

**HIGH SPEED, DEAD RECKONING, AND TOWED  
IMPLEMENT CONTROL FOR AUTOMATICALLY  
STEERED FARM TRACTORS USING GPS**

**A DISSERTATION  
SUBMITTED TO THE DEPARTMENT OF MECHANICAL ENGINEERING  
AND THE COMMITTEE ON GRADUATE STUDIES  
OF STANFORD UNIVERSITY  
IN PARTIAL FULFILLMENT OF THE REQUIREMENTS  
FOR THE DEGREE OF  
DOCTOR OF PHILOSOPHY**

**David Mark Bevly**

**August 2001**

UMI Number: 3028071

Copyright 2001 by  
Bevly, David Mark

All rights reserved.

UMI<sup>®</sup>

---

UMI Microform 3028071

Copyright 2002 by Bell & Howell Information and Learning Company.  
All rights reserved. This microform edition is protected against  
unauthorized copying under Title 17, United States Code.

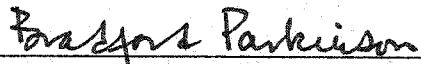
---

Bell & Howell Information and Learning Company  
300 North Zeeb Road  
P.O. Box 1346  
Ann Arbor, MI 48106-1346

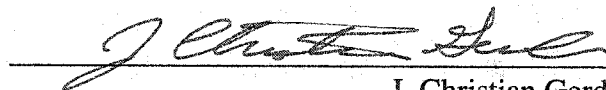
**© Copyright 2001 David Mark Bevly**

**All Rights Reserved**


I certify that I have read this thesis and that in my opinion it is fully adequate, in scope and in quality, as a dissertation for the degree of Doctor of Philosophy.

  
\_\_\_\_\_  
Bradford Parkinson (Principal Advisor)

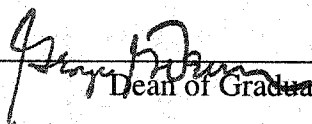
I certify that I have read this thesis and that in my opinion it is fully adequate, in scope and in quality, as a dissertation for the degree of Doctor of Philosophy.

  
\_\_\_\_\_  
J. Christian Gerdes

I certify that I have read this thesis and that in my opinion it is fully adequate, in scope and in quality, as a dissertation for the degree of Doctor of Philosophy.

  
\_\_\_\_\_  
Daniel DeBra

Approved for the University Committee on Graduate Studies:

  
\_\_\_\_\_  
Dean of Graduate Studies





# Abstract

The ability of GPS to provide accurate position and attitude information has led to many advances in land, marine, and air navigation systems. Recently, research has been done in the area of automated farm tractors using GPS. Driver assisted agricultural vehicles have many benefits such as relieving the driver from the tedious task of steering, increased accuracy, allowing for operation during poor visibility periods such as night, fog, and heavy dust environments, as well as providing the opportunity for new agricultural techniques. However, the capabilities of these systems must be increased for high-speed spraying operation and continuous control through short GPS outages. Additionally, the ability to accurately control farm *implements* (rather than the tractor) will be necessary, in order for automatically steered farm tractors to become more widespread.

Various mathematical models that have been used for the control of off-road vehicles are discussed. It has often been noted that the performance of these controllers decreases at speeds above 5 m/s (10 mph). A system identification approach is taken to determine an accurate yaw model in order to improve automatic control at higher speeds and understand controller limitations due to neglecting the yaw dynamics. Yaw dynamic models are developed for multiple speeds to show the effect of velocity on the model. The identified yaw model exhibits dominant second order dynamics. Although the model does not resemble any previously used analytical models, a model which includes a front tire relaxation length is shown to capture the identified model characteristics. Results show an improvement of the lateral tracking error (with a decrease in control effort) using the new system identification model.

Integration of GPS with a low cost Inertial Navigation System (INS) is shown to be capable of providing continuous control of a tractor on a farm, despite intermittent loss of GPS measurements. Two Extended Kalman Filters (EKF) are cascaded in order to accurately estimate all of the biases and states needed for dead reckoning navigation and control of the tractor through short GPS outages. The cascaded estimation scheme is shown to have several advantages over a traditional estimation architecture, including better state and bias estimation. Additionally, models of the error growth due to integration of sensor noises are developed and shown to adequately predict the dead reckoning heading and position errors.

Finally, the use of GPS position measurements on a tractor towed implement for position control of the implement through automatic steering of a farm tractor is presented. Many farm operations could benefit from the ability to control the actual position of the implement as opposed to the position of the tractor. A simple kinematic model is therefore developed for the implement. A controller is designed and verified on the experimental system by maintaining the position of the implement on a given path across the field.

Experimental results are given which verify the ability to extend the cm-level control accuracy of farm tractors to towed implements, high speeds, and through short GPS outages. Accurate lateral control of 4 cm ( $1\sigma$ ) of the tractor is performed up to 16 mph, as opposed to limitations of less than 10 mph for similar accuracies in previous work. This potentially represents a 60% improvement in the efficiency of the tractor allowing it to perform accurate automatic spraying in less time. Lateral control of 4 cm without any GPS attitude measurements and lateral errors of less than a foot for 20-40 second complete GPS outages is also presented. Finally, experiments show 10 cm lateral tracking of a towed implement using direct GPS measurements and the techniques developed in this thesis.

# Acknowledgments

First off, I thank God for giving me both the opportunity and ability to do this work. “I can do all things through him who strengthens me” (Philippians 4:13).

I would like to thank my advisor, Professor Brad Parkinson, for his guidance and technical assistance during the past three years (see, I did not say “freedom”). I would also like to thank my co-advisor, Professor Chris Gerdes, for his equally important assistance and mentorship, as well as helping me prepare for academia. I’ve had an incredible opportunity to work under three great and distinctly different advisors during my graduate years. Hopefully I can draw from each of them as I move into their role. I’d also like to thank my third reader, Professor Dan DeBra, for his helpful comments and encouragement on being a controls experimentalist in academia. There were also many other professors, like Ed Carryer, who were always willing to help when the need arose.

I would like to thank John Deere for providing the financial support, donation of the 8400 farm tractor, and most importantly interesting and technically challenging problems. Special thanks to Bob Mayfield who was always excited about our work and willing to help in any way we needed. I would also like to thank the folks at the John Deere test sites, including Butch Hansen, Robert Lorentzen, and Terry Sturtz. There is no better place to program and debug control software than in a John Deere tractor, on a farm in Arizona or Central California, while listening to country music on the radio station. Except for the computer part, that is how I grew up spending my summers, so it felt like home (Texas), at times, even at Stanford.

I would like to thank IntegriNautics and Mike O’Conner for providing the GPS positioning hardware and software and an unwarranted amount of technical assistance and support behind all of their equipment.

I'd also like to thank the past tractor members, Mike O'Conner, Tom Bell, and Andy Rekow, for their technical contributions over the past four years. They paved the way for this research and created an experimental platform that was very flexible. This made it relatively effortless (in terms of experimental systems) to gather the results provided in this thesis (until "the accident"). I would also like to thank my cube-mate, Gabe Elkaim, for his technical assistance and for not liking sports so that I could finish in four years.

I would like to thank the members of the GPS (WAAS and LAAS – and yes I know the difference now) labs for always helping to answer all of my GPS (and other) questions. A special thanks goes to Guttorm Opshaug, Dennis Akos, Konstantine Gromov, and Demoz Gebre-Egziabher. I would also like to thank Demoz for his help in the areas of estimation, Kalman filtering, and dead reckoning, as well as all the interesting talks about starting a career in academia. Thanks to the Dynamic Design Lab (DDL), including Eric Rossetter, for giving me an ME lab home (away from the Aeros).

I also want to thank my family, including my two brothers, Rick and John, for all of their support. Special thanks to my dad, whom I strive to be like some day, for teaching me how to work hard on the farm and that life is not always fair. The experience of growing up on a farm has always been invaluable to my success, but for this thesis it added a unique relevance. I also have to thank my mom, who is always right, for her encouragement as well as teaching me the power of prayer and positive thinking.

Special thanks to my intramural basketball team (The Bevely Hillbillies) and other great friends I played ball with at Stanford, like Adam Skaates, Bruce Khailany, Chris Stolte, Mike Clarke, and Dan Gilchrist, who gave me a haven away from research.

I would like to thank the 2A girls, Brook Mykytka and Kristin Hedgepath, as well as John Pyhtila for being great friends during my tenure at Stanford. These life-long friends truly made living in California a great experience, even if we didn't agree politically. I also would like to thank Stephanie Stoll for her companionship over the past several years. I don't think I could have done it without her.

I would like to recognize Noe Lozano, Dean Plummer, and the Dean's Office for the Stanford 3D Fellowship which provided two years of my support. I am also forever grateful to Professor Roth for bringing me to Stanford.

Gig'em Aggies, A<sub>T</sub>M '94 - whoop!

# Table of Contents

Abstract .....	v
Acknowledgments .....	vii
1 Introduction .....	1
1.1 Tractor Modeling .....	2
1.2 GPS/INS Integration .....	4
1.3 Implement Control .....	6
1.4 Objectives .....	8
1.5 Organization .....	8
1.6 Contributions .....	10
2 Tractor Yaw Dynamic Modeling .....	11
2.1 Commonly Used Physical Yaw Dynamic Models .....	12
2.2 System Identification of the Yaw Dynamic Model .....	15
2.2.1 Identification with Single Rear Wheels .....	17
2.2.2 Identification with Dual Rear Wheels .....	21
2.3 New Yaw Dynamic (NYD) Model .....	23
2.4 Bicycle Model with Tire Relaxation Lengths .....	27
2.5 Physical Model Parameter Identification/Selection .....	30
2.6 Comparison of Models .....	33
2.7 Experimental Control Results .....	38

2.8	Conclusions.....	42
3	Control Algorithm.....	45
3.1	Lateral Dynamic Controller Model .....	45
3.1.1	Hydraulic Steering Valve Model.....	45
3.1.2	Lateral Position Model .....	47
3.2	Control Law .....	49
3.3	Simulated and Experimental Line Tracking .....	52
3.4	Effect of Neglecting Sideslip.....	54
3.5	Conclusions.....	58
4	Cascaded State Estimation .....	59
4.1	Tractor Dynamics and Estimated States .....	60
4.2	Regular Estimation .....	62
4.2.1	Shortcomings of the Regular Estimation Algorithm.....	67
4.3	Cascaded Estimation Algorithm .....	69
4.4	Experimental Results .....	74
4.4.1	Rough Verification of Bias Estimates .....	75
4.5	Conclusions.....	77
5	Dead Reckoning Analysis .....	79
5.1	Error Analysis.....	80
5.1.1	Heading Error Analysis.....	80
5.1.2	Lateral Error Analysis for the Stationary Case .....	82
5.1.3	Lateral Error Analysis for the Non-Stationary Case .....	84
5.1.4	Error Growth Prediction Through Covariance Propagation .....	87
5.2	Experimental Dead Reckoning Results .....	88
5.3	Conclusions.....	95
6	Partial INS Based Attitude for Control of a Tractor .....	97
6.1	Effect of Roll .....	98

6.2	Estimation Algorithm Using PINS Attitude.....	99
6.2.1	Reconstructing an Estimate of Heading .....	101
6.2.2	Estimation of the Remaining Tractor States .....	104
6.2.3	Reconstructing an Estimate of Roll.....	106
6.3	Simulation Results .....	110
6.4	Experimental Results .....	112
6.5	Conclusions.....	118
7	Towed Implement Control .....	119
7.1	Tractor-Implement Model .....	120
7.2	Implement Control Algorithm .....	124
7.3	Implement Estimation Algorithm.....	129
7.4	Experimental Implement Control Results .....	133
7.5	Conclusions.....	140
8	Conclusions and Further Work .....	141
8.1	Conclusions.....	141
8.2	Future Work.....	143
8.3	Closing.....	148
	Appendices .....	149
A	Experimental System .....	149
B	Identification of HC12 Delay and Its Effect on the Yaw Dynamic Modeling ..	153
C	Implement Dynamics and Kinematics.....	159
C.1	Angular Dynamics.....	159
C.2	Lateral Position Dynamics .....	161
C.3	Position Kinematics and Dynamics.....	162
C.4	Inverse Kinematics.....	163
D	Steering Valve Identification.....	165
	Bibliography.....	171



# List of Tables

Table 2.1	Model Parameters for the NYD Model .....	25
Table 2.2	Parameters Used for the Physical Models.....	32
Table 2.3	Summary of Physically Derived Models .....	33
Table 2.4	Summary of System Identified Models.....	33
Table 3.1	Parameters of the Steering System.....	46
Table 3.2	Control Gains for Selected Velocities .....	51
Table 4.1	Assumed Process Noise Covariance for Each State.....	64
Table 4.2	Assumed Sensor Noise Covariances .....	64
Table 6.1	Simulation Study Results: Heading Estimation and Lateral Errors ( $1\sigma$ ) for Various Sensor Sets .....	111
Table 6.2	Static Sensor Noises ( $1\sigma$ ).....	113
Table 6.3	Comparison of Attitude Systems for Control of the Tractor .....	117
Table 7.1	Implement Model Parameters .....	121
Table 7.2	Estimated States for Towed Implement Control.....	130
Table 7.3	Additional Covariance Values for Process Noise of the Implement States .....	131
Table D.1	Parameters Describing the Stead State Characteristics of the Steering Valve .....	167

## List of Figures

Figure 2.1	Schematic of the Bicycle Model .....	13
Figure 2.2	Schematic of Data Acquisition for System Identification.....	15
Figure 2.3	Schematic of a Farm Tractor .....	16
Figure 2.4	Spectral Analysis and Box Jenkins Second Order Fit of the Input ( $\delta$ ) to Output ( $r$ ) Data .....	18
Figure 2.5	Model Errors vs. System Identified Model Order for No Zeros and N-1 Zeros for Single Rear Wheels .....	18
Figure 2.6	Modeled Yaw Rate Output for Zero Order, First Order and Second Order Model Fits Versus Actual Yaw Rate (Actual – Solid Line) .....	20
Figure 2.7	ID2 Model Frequency Responses vs. Velocity for $V_x=2,4,6$ and 8 m/s for Single Rear Wheels.....	21
Figure 2.8	Model Errors vs. System Identified Model Order for No Zeros and N-1 Zeros for Dual Rear Wheels.....	22
Figure 2.9	ID2 Model Frequency Responses vs. Velocity for $V_x=2,4,6$ and 8 m/s for Dual Rear Wheels .....	22
Figure 2.10	ID2 Data and Best Fit (NYD) Model Parameters vs. Velocity for Single Rear Wheels .....	24
Figure 2.11	ID2 Data and Best Fit (NYD) Model Parameters vs. Velocity for Dual Rear Wheels.....	25
Figure 2.12a	Model Errors and Normalized Model Errors for the ID2 Model with Single Rear Wheels .....	26
Figure 2.12b	Model Errors and Normalized Model Errors for the NYD Model with Single Rear Wheels .....	26
Figure 2.13a	Model Errors and Normalized Model Errors for the ID2 Model with Dual Rear Wheels .....	26

Figure 2.13b	Model Errors and Normalized Model Errors for the NYD Model with Dual Rear Wheels .....	26
Figure 2.14	TR Model Frequency Response vs. Velocity for $V_x=2,4,6$ and 8 m/s .....	28
Figure 2.15	FTR Model Frequency Response vs. Velocity for $V_x=2,4,6$ and 8 m/s .....	29
Figure 2.16	Front and Rear Tire Cornering Stiffness vs. Tractor CG Location .....	31
Figure 2.17	Pole-Zero Plot of Various Models at 4 m/s (regular) and 8 m/s (bold) .....	34
Figure 2.18a	ID2 Data and FTR Model Approximation vs. Velocity for Single Rear Wheels .....	35
Figure 2.18b	ID2 Data and FTR Model Approximation vs. Velocity for Dual Rear Wheels .....	35
Figure 2.19a	Frequency Response Comparison of the FTR and NYD Models for $V_x=2, 5$ and 8 m/s for Single Rear Wheels .....	36
Figure 2.19b	Frequency Response Comparison of the FTR and NYD Models for $V_x=2, 5$ and 8 m/s for Dual Rear Wheels .....	36
Figure 2.20	Yaw Rate Modeling Errors for Various Model Types at $V_x=2, 5$ and 8 m/s for Single Rear Wheels .....	37
Figure 2.21	Yaw Rate Modeling Errors for Various Model Types Averaged Over all Data Runs for Single and Dual Rear Wheels .....	38
Figure 2.22	Resulting Closed-Loop Bandwidth vs. Velocity Using LQR .....	39
Figure 2.23	Experimental Run Using an SK Model at 5 m/s .....	40
Figure 2.24	Experimental Run Using an ID1 Model at 5 m/s .....	41
Figure 2.25	Experimental Run Using the NYD Model at 5 m/s .....	41
Figure 2.26	Experimental Run Using the NYD Model at 16 mph (8 m/s) .....	42
Figure 3.1	Schematic of the Lateral Dynamics for the Tractor .....	47
Figure 3.2a	Continuous Open Loop Roots for the Lateral Tractor Model .....	49
Figure 3.2b	Discrete Open Loop Roots Sampled at 0.1 Seconds (10 Hz) .....	49
Figure 3.3a	Continuous Closed-Loop Roots for the Lateral Tractor Model .....	51
Figure 3.3b	Discrete Closed-Loop Roots Sampled at 0.1 Seconds (10 Hz) .....	51
Figure 3.4	Schematic of a Desired Trajectory .....	52
Figure 3.5a	Simulated 1m Step Response .....	53
Figure 3.5b	Simulated 2m Step Response .....	53

Figure 3.6	Experimental vs. Simulated Step Response .....	54
Figure 3.7	Comparison of Control Algorithms on the FTR Model for a Simulated 1 m Step Response at 5 m/s .....	56
Figure 3.8	Comparison of the Significance of the Two Different Lateral Velocity Components for a Simulated 1 m Step Response at 5 m/s .....	57
Figure 3.9	Comparison of Step Responses at 5 m/s Using the NYD Controller with Mis-Modeled CG Locations.....	58
Figure 4.1	Schematic of a Farm Tractor .....	61
Figure 4.2	Gyroscope Bias Estimation from the Regular Estimation Scheme.....	67
Figure 4.3	Actual vs. Estimated Heading with the Regular EKF Estimation Scheme .....	68
Figure 4.4	Estimation of the Gyroscope Bias with no Estimate of the Steer Angle Bias During a Straight Line Tracking Experiment.....	69
Figure 4.5	Block Diagram of the Cascaded Estimation Architecture .....	70
Figure 4.6	Estimation of All Four Biases During a Simulated Straight Line Tracking Run with an Initial Lateral Step Input of 1m .....	73
Figure 4.7	Experimental Validation of Separate Bias Estimation of Steer Angle and Gyroscope Biases During Straight Line Tracking.....	74
Figure 4.8	Heading and Radar Bias Estimation During Experimental Straight Line Tracking .....	76
Figure 4.9	Heading Error Through Explicit Integration of the Yaw Gyroscope From the Cascaded Estimation Technique.....	77
Figure 5.1	Integration of Gyroscope Noise .....	81
Figure 5.2	Validation of the Heading Error Growth Using a Monte Carlo Simulation .....	82
Figure 5.3	Validation of the Lateral Error Growth for the Stationary Case Using a Monte Carlo Simulation.....	84
Figure 5.4	Validation of the Lateral Error Growth for the Non-Stationary Case Using a Monte Carlo Simulation.....	86
Figure 5.5	Heading Error Following a Simulated GPS Outage.....	89
Figure 5.6	Lateral Error Following a Simulated GPS Outage.....	90
Figure 5.7	Dead Reckoning Position Errors After a Simulated GPS Outage for a Single Dead Reckoning Experiment .....	91
Figure 5.8	Lateral Estimation Errors due to Integrating Various Headings (Demonstrating the Effect of Crab Angle on the Errors) .....	92
Figure 5.9	Dead Reckoning Performance Around a Track .....	93

Figure 5.10	Dead Reckoning Errors Around the Track.....	94
Figure 6.1	Effect of Positive Roll on GPS Measurements .....	99
Figure 6.2	Schematic of a Tractor .....	100
Figure 6.3	Separate Yaw Gyroscope Bias Estimation.....	104
Figure 6.4	Spectral Analysis of Tractor Cab Roll (at 2 m/s) .....	108
Figure 6.5a	Heading Error vs. Roll Noise for Various Sensor Sets .....	111
Figure 6.5b	Lateral Tracking Error vs. Roll Noise for Various Sensor Sets .....	111
Figure 6.6	Accelerometer Roll and Roll from GPS.....	113
Figure 6.7	Filtered Accelerometer Roll, GPS Roll, and Their Difference .....	114
Figure 6.8	Experimental Step Response Without GPS Attitude Measurements .....	115
Figure 6.9	Heading Estimation for the Experimental Step Response .....	115
Figure 6.10	Control of the Tractor in a Field.....	116
Figure 6.11	Heading Estimation for the Field Run.....	116
Figure 6.12	Heading Errors and Heading Estimate Errors for the Field Run.....	117
Figure 7.1	Schematic of a Farm Tractor and Towed Implement Combination.....	120
Figure 7.2	Implement Model Parameters vs. Velocity for the Implement Down (solid) and Implement Up (Dashed) .....	122
Figure 7.3	Implement Model Validation .....	123
Figure 7.4a	Continuous Open Loop Poles of the Tractor-Implement Combination .....	124
Figure 7.4b	Discrete Open Loop Poles of the Tractor-Implement Combination .....	124
Figure 7.5	Schematic of a Desired Implement Trajectory.....	125
Figure 7.6a	Continuous Closed-Loop Poles of the Tractor-Implement Combination .....	127
Figure 7.6b	Discrete Closed-Loop Poles of the Tractor-Implement Combination .....	127
Figure 7.7	Identification of the Second Order Yaw Dynamic Model of the Tractor with a Towed Implement.....	128
Figure 7.8	GPS Guided Farm Tractor and Implement .....	133
Figure 7.9	Simulation of Tractor-Implement Step Responses.....	134
Figure 7.10	Experimental Implement Step Response.....	135
Figure 7.11	Comparison of Simulated and Experimental Implement Control Step Response for Two Different Initial Conditions.....	135

Figure 7.12	Implement Lateral Tracking Errors.....	136
Figure 7.13	Simulated Control of the Implement Along an Arc .....	137
Figure 7.14	Lateral Errors of Implement and Tractor Position for the Simulated Arc Trajectory .....	137
Figure 7.15	Implement Angle During Simulated Control Along an Arc .....	138
Figure 7.16	Experimental Control of the Implement Along an Arc.....	139
Figure 7.17	Lateral Errors of Implement and Tractor Position for the Experimental Arc Trajectory.....	139
Figure A.1	GPS Guided Farm Tractor.....	150
Figure A.2	Components of the GPS Farm Tractor .....	151
Figure A.3	Overall Block Diagram of the Guidance System .....	152
Figure B.1	Pole Location of a First Order Model of $H(z)$ for Various Sample Rates .....	154
Figure B.2	Spectral Analysis (ETFE), First Order Box-Jenkins Model, and a Pure Time Delay Model of $H(z)$ .....	155
Figure B.3	Comparison of Identified Zero Location with A/D Measurements (Delayed by 0.075 Seconds) and HC12 Measurements .....	156
Figure B.4	Model Errors vs. Model Order for No Zeros and N-1 Zeros for Identification Using A/D Measurements.....	157
Figure B.5a	Model Errors vs. Model Order for No Zeros and N-1 Zeros for Identification Using HC12 Measurements.....	157
Figure B.5b	Model Errors vs. Model Order for Identification Using HC12 Measurements Shifted Forward by 0.075 Seconds .....	157
Figure B.6a	Comparison of ID2 Data with A/D Measurements and HC12 Measurements.....	158
Figure B.6b	Comparison of ID2 Data with A/D Measurements and HC12 Measurements Shifted Forward by 0.075 Seconds .....	158
Figure C.1	Schematic of a Farm Tractor and Implement for Calculating the Implement Angular and Lateral Dynamic Models.....	160
Figure C.2	Schematic of the Tractor and Implement for Calculating Forward and Inverse Kinematics .....	162
Figure D.1	Typical Valve Characteristics Including Dead-Band Region and Saturation (Steady State Slew Rate vs. Voltage Input).....	165
Figure D.2	Experimental and Valve Model of the Steady State Slew Rate vs. Input Voltage.....	166
Figure D.3	Valve Inversion and Valve Dynamics Block Diagram .....	167

Figure D.4	Empirical Transfer Function and Box-Jenkins Model Fit of the Steering Actuator Dynamics .....	168
Figure D.5	Valve Input and Actual vs. Model Valve Outputs of Steer Angle ( $\delta$ ) and Slew Rate ( $\dot{\delta}$ ).....	169

# Chapter 1

## Introduction

The global positioning system (GPS) has provided the ability to determine a body's position anywhere on the surface of the globe. Atmospheric conditions, injected noise, called Selective Availability<sup>1</sup> (SA), and other random noise corrupt the positioning accuracy. However, differential corrections, known as differential GPS (DGPS) can eliminate most of these errors. In fact, carrier-phase differential GPS has been shown to provide a positioning accuracy of about 2 cm ( $1\sigma$ ) [Cohen, 1995]. Additionally, a four antenna Carrier-Phase GPS unit can be used to provide 0.1 degree (zero drift) attitude measurements in roll, pitch, and yaw without a correction reference station [Cohen, 1994]. The ability to measure position and attitude on vehicles has led to many advances in land, marine, and air navigation systems.

The farming industry has also seen a rise in the use of GPS for precision agriculture. GPS, coupled with agricultural systems, gives farmers the ability to monitor yields in their fields and apply site specific farming techniques to increase the efficiency and productivity of every acre of land [Lachapelle, 1994]. More recently, research has been performed in the area of automated farm tractors [O'Connor, 1996, Bell, 1998 & Nieminen, 1994] and combines [Cordesses, 1999] using GPS. Automatically steered

---

<sup>1</sup> The Department of Defense removed Selective Availability on May 2, 2000. However this did not affect the work in this thesis because the Carrier-Phase DGPS effectively removed this error source.



farm equipment has many advantages, including: relieving the driver of the tedious task of accurately steering the vehicle, operation in low visibility circumstances such as night, fog or heavy dust, and increasing precision agriculture accuracies. Farms generally provide an excellent opportunity for the use of GPS because of the openness of the farming environment, which provides good satellite visibility. A differential reference antenna can easily be placed at the corner of a farm to provide cm-level positioning accuracy on a given field. Additionally, automatically steered tractors have much greater accuracy than human drivers, opening the door for new farming techniques. A farmer in South Texas could not use one of his farm hands to do crop cultivating tasks because the operator could not cultivate for one chain<sup>2</sup> without plowing up some of the crops [Bevly, 1998]. Currently, some farms are experimenting with reducing crop rows from 30 to 18 inches, where accurate control will be a necessity. To steal a phrase from Tenny Sharpe at NavCom, "This system turns a farm's worst driver into their best driver."

## 1.1 Tractor Modeling

In order to provide accurate control of a farm vehicle, the handling characteristics (known as the yaw dynamics) must be well known or modeled. Most previous control of farm vehicles has been done at tillage speeds (2-3 m/s). However, some farm applications, such as spraying, require accurate control at speeds greater than 5 m/s. Comprehensive knowledge of these dynamics will allow a control architecture to perform accurate control while spraying. Many spraying operations are performed when the crop is anywhere from 4 inches to 3 feet high. The tractor must be accurately controlled between the rows (30 inch rows are most common) while spraying to reduce any crop damage. This thesis assesses the impact of the dynamic steering characteristics of a farm tractor on automatic lateral control. Particular interest is given to the change in dynamics at speeds in the range of 12-18 mph where automatic control of farm operations, such as spraying, would be useful.

---

<sup>2</sup> Chain is a dimension of length equal to 66 feet. Chains are often used in marking field lengths because of the property that one chain squared equals one tenth of an acre. The name was derived from farmers cutting a chain 66 feet in length to measure field acreage.

Previous research has developed automatically steered farm tractors that operate at low speeds by modeling the yaw rate to steer input as a constant gain [O'Connor, 1996]. It has been shown that the accuracy of the compensator using this model decreases with increasing speeds [Elkaim, 1997] and this thesis demonstrates instability at speeds above 5 m/s (10mph), for certain control gains. Alternatively, a first order lag between steer angle and yaw rate (neutral steer characteristics) has been used to model the yaw dynamics of the tractor [Rekow, 1999].

Several researchers have modeled the dynamic behavior of heavy farm vehicles [G.M. Owen, 1982; Crolla, 1983] and construction equipment [R.H. Owen, 1982]. The goal of these previous models was to characterize the vehicle dynamics for design and safety evaluations. This thesis further investigates the yaw dynamics of a farm tractor for the purpose of increasing automatic control performance at higher speeds. Previous work for automatic high speed control of a farm tractor neglected the yaw dynamics [Stombaugh, 1998]. A model from steer input to lateral error may have made it difficult to observe the yaw dynamics due to the  $-40$  dB slope from the two integrators (one from yaw rate to heading and one from heading to lateral position). Another paper used a simple kinematic model and produced a velocity independent control algorithm [Cordesses, 1999]. It is important to understand the yaw dynamics and the effect they have on control performance and/or limitations.

The first part of this thesis presents the system identification of a new model for the farm tractor's yaw dynamics in order to improve automatic control at higher speeds and understand controller limitations due to neglecting these dynamics. As speed increases, higher order models are required to maintain accurate lateral control of the vehicle. Neglecting these dynamics can cause the controller to become unstable at the bandwidths required for accurate control at higher speeds. The yaw dynamic model, which is found to be dominated by a second order response, is identified for multiple speeds to determine the effect of velocity on the model. The second order yaw dynamics cannot be represented by the traditional bicycle model. An analytical derivation shows that the specific characteristics can, however, be captured by a model consisting of a significant (non-negligible) relaxation length in the front tire. Experiments confirm the effectiveness of this new model for accurate lateral control of the farm tractor at high speeds.

## 1.2 GPS/INS Integration

Farms provide an excellent opportunity for the use of GPS because of the openness of the farming environment, which provides good satellite visibility. Although, farms generally have a very open view of the sky and GPS satellites, many farms are bordered by barns or foliage, which may cause temporary loss of GPS satellites, or multi-path errors. Additionally, intermittent communication loss can occur between the reference antenna and the tractor. In order for automatically steered tractors to gain major acceptance, the system must not be halted for such outages. Integration of GPS with a low cost Inertial Navigation System (INS) can help to insure continuous control of a tractor on a farm.

The integration of inertial sensors with GPS has been given much attention. The stability of GPS over long periods of time provides a perfect compliment to the short-term accuracy of inertial units, that can have large errors over longer periods of time due to bias drifts. Some research has studied the use of updating position estimates with inertial equipment between low rate (1-5 Hz) GPS measurement updates [Da, 1996; Gebre-Egziabher, 1998]. Other work has concentrated on utilizing the inertial units during short GPS outages [Berman, 1998; Masson, 1996]. Additionally, augmentation of GPS with inertial sensors for land navigation location systems has been studied [Abbot, 1999]. Evaluation of a Fiber Optic Gyro (FOG), similar to the gyro used in this research, was used for dead reckoning navigation of an indoor robot [Borenstein, 1998]. Land vehicle navigation using the FOG has also been studied [Allen, 1994]. Fusion of GPS and dead reckoning systems for autonomous land vehicles was studied in [Schonberg, 1996; Aono, 1998]. A method for estimating vehicle states such as sideslip and wheel slip using GPS has been developed [Bevly, 2000(a)]. The methodology has been extended to incorporate INS measurements to estimate vehicle parameters such as tire cornering stiffness [Bevly, 2001].

Recently a two-antenna system (used for heading) has been integrated with inertial sensors for a full attitude solution [Hayward, 1999]. GPS velocity measurements were used to determine vehicle accelerations in order to correct the accelerometer's roll and pitch measurements. Because most farm applications occur at constant speed, it is not

necessary to account for low frequency longitudinal vehicle accelerations. However, off road vehicles do experience large amounts of higher frequency vibrational accelerations that can corrupt the accelerometer measurements.

In this thesis, low-cost INS integrated with carrier-phase DGPS is studied for the control of a farm tractor. An inexpensive dead reckoning system, initialized using carrier phase differential GPS, provides adequate position and attitude estimation for the continuous control of a farm tractor during short GPS outages. Analysis based on the short-term integration of sensor noise is used to determine the growth of the dead reckoning heading and position errors over time. The cm-level accuracy of carrier-phase DGPS allows for precise calibrations of the plant and sensor models in order to improve the estimation accuracy using the INS system. Additionally an INS based attitude system is investigated and shown to be a feasible alternative to the multiple antenna GPS attitude solution for the control of a farm tractor. Results are given which verify the ability of INS to provide dead reckoning and attitude estimation for control of a farm tractor.

The control algorithm used for the tractor in this thesis is actually independent of whether or not GPS measurements or inertial measurements are available. This is due to the fact that the control algorithm only uses the estimates of specific states, and not the measurements themselves (assuming that the estimator can produce the required state estimates given its measurements). This flexibility allows for optimization of the GPS/INS integration and dead reckoning estimator, without affecting the control algorithm of the tractor.

Much of the GPS/INS related work is concerned solely with the navigation and dead reckoning estimation of vehicles [Rogers, 1999; Brodie, 1999; Weisenburger, 1999], and not control of the vehicle. In this thesis, however, both dead reckoning and control are needed. This requires estimating states, including sensor biases, necessary for accurate full state feedback control, in addition to the states required for accurate dead reckoning and navigation. Estimation of all of these states in one traditional estimator has several draw backs, including an inability to always estimate certain biases accurately and degraded dead reckoning estimation.

Therefore, an estimation scheme using two cascaded Kalman filters is developed in this thesis. A dead reckoning filter estimates the navigation states, including inertial

(gyroscope and radar) sensor biases using GPS, and provides position and attitude estimates when GPS measurements are not available. A control filter estimates the additional states required for control of the tractor, using the corrected sensor measurements from the dead reckoning filter. The cascaded estimation scheme is shown to have several advantages over a traditional estimation architecture, including better state and bias estimation. Similarly, a two stage least square estimation has been shown to provide better state estimation than an Extended Kalman Filter [Haupt, 1996]. Additionally, separate filters for individual measurements with biases were shown to be more effective than a single, coupled filter for underwater ranging applications [Johnson, 1989].

The cascaded architecture separates the bias estimation of several of the states. Separate bias estimation has been studied for decreasing computational requirements, by using two lower-order estimators [Friedland, 1969]. Properties, alternate derivations, and the optimality of Friedland's estimator are discussed in [Friedland, 1978], [Ignagni, 1981], and [Alouani, 1993], respectively. Additionally, the separate bias estimation of Friedland has been extended to non-linear systems [Caglayan, 1984], time varying bias models [Tacker, 1972], and to systems with a randomly varying bias [Tanaka, 1975; Ignagni, 1990]. Additionally, it has been shown that separate bias estimation schemes can produce a reduced order filter for estimating biases in a system with no sensor noise [Haessig, 1998].

## 1.3 Implement Control

As precision agriculture techniques become more demanding, and automated guided systems become more widespread, the need for accurately controlling a farm implement becomes inevitable. It is, after all, the implement that is performing the farm task. Many agricultural operations pull towed implements, in which their position can vary from that of the tractor (especially on contours and side hills). In order to fully utilize precision row cropping techniques and automated steering systems, it will become necessary to accurately control towed implements. For example, some farms will plant crops on

contoured trajectories using towed planters in which the planter implement and tractor positions can differ. In order to accurately control the spacing between two passes, it will be necessary to control the actual planter position. Later in the crop season, crops cultivated and harvested with other, often hitch mounted, implements will require accurate row positioning (especially if cultivated or harvested with an automated system) in order to prevent crop losses. Other farm areas use underground irrigation lines buried along the crop rows, called drip tape irrigation, to reduce the amount of water loss due to evaporation. Control architectures would be beneficial that could guide an implement through a field without cutting an irrigation line. Currently, markers are used to indicate where irrigation lines are located and drivers must very slowly and carefully guide the tractor between the irrigation lines. It is frequently necessary to control work implements around permanent obstacles in the field. The ability to directly control an implement could additionally lead to advances in other farming techniques. Often times precision implements are mounted on the hitch of a tractor, which limits implement size due to the load on the tractor. By controlling towed implements it may become possible to provide more effective farm tools.

Research has studied the control of robotic vehicles pulling trailers [Laumond, 1998 & Chen, 2000] and heavy trailer truck combinations [Chen, 1995]. However, the majority of these systems are not trying to specifically control the location of the trailer. There has also been work done on the control of tractor implements, using GPS measurements, through actuation of the implement itself [Zuydam, 1998]. However, large actuation forces are required to move sizable towed implements plowing soil, and in some cases the actuation moves the tractor instead of the implement. Some initial simulation work has been done on controlling tractor-implement combinations around a constant geometry radius [Larsen, 1995]. More recent work has even used GPS to control a tractor plus an implement [Smith, 1985], although there are no details on the model and control algorithms. This thesis explores the use of a simple kinematic implement model, using differential carrier-phase GPS measurements ( $1\sigma=2$  cm) on both the tractor and towed implement for specifically controlling the position of the implement. This control is accomplished through the steering actuation of the tractor.

## 1.4 Objectives

In order for automatically steered farm tractors to become more widespread, they must be able to perform accurate control over the range of farm applications. Therefore, the objective of this thesis was to extend the capabilities of current automatically steered farm tractors using GPS. These extensions include accurately controlling towed implements, accurate control at high speeds for spraying, and continuous control through short GPS outages. Additionally, it was desired to develop new fundamental models and estimation techniques to provide these capabilities and determine the limitation of previous models and techniques.

## 1.5 Organization

This thesis is divided into eight chapters. Chapter 2 describes a system identification approach of determining the dynamics of the tractor. Identification is performed at varying speeds for the tractor with single and dual rear wheels. Experimental results are given showing the improvement in control performance at high speeds for farm operations such as spraying. This chapter also compares these dynamics with other popular analytical models used in the control and design of vehicles. An analysis of the experimentally identified model is performed in order to develop a matching analytical model.

Chapter 3 discusses the control architecture used for guiding the tractor in this thesis. The newly developed yaw dynamics described in Chapter 2 along with the steering dynamics and lateral tractor dynamics are linearized and placed into a state space form. An LQR algorithm is used to design the control gains for the full state feedback of the system. Open and closed-loop roots are shown along with simulated and experimental step responses of the control architecture.

Chapter 4 develops a cascaded Kalman Filter state estimation architecture for estimating all of the states required for full state feedback. The cascaded architecture also estimates all of the system biases in order to improve the control and dead reckoning accuracy of the system. Results are given showing the estimator's ability to estimate the

system biases and explicitly integrate the corrected gyroscope reading to produce heading estimates when GPS measurements are removed.

Chapter 5 evaluates the dead reckoning capabilities of the estimator given in Chapter 4. Error analysis equations are developed based on the integration of sensor noise and are shown to adequately describe the errors associated with the dead reckoning system. Simulated GPS outages are created by removing GPS position and attitude from the system during experimental runs, thus validating the dead reckoning system.

Chapter 6 develops an inertial sensor based alternative to using multiple GPS antennas for attitude. A yaw rate gyroscope is used in a heading estimator to filter the noisy heading measurements from the velocity vector of a single GPS antenna. The heading estimator in conjunction with a low pass filtered accelerometer provide all of the attitude information necessary to accurately control the farm tractor. Simulation results are given showing the importance of the gyroscope for filtering heading measurements as well as the importance of a measure of roll. Experimental results validate the simulation study showing accurate control of the tractor without any GPS attitude measurements.

Chapter 7 presents a method for using the GPS guided tractor to control a towed implement. A GPS receiver is placed on the *implement* (in addition to the GPS receiver on the tractor used in previous work) to provide cm-level position measurements of the implement. A kinematic model for the implement is developed and linearized and added to the tractor dynamics. The parameters of the implement model are obtained using system identification techniques and the model is validated. An estimator and control architecture is developed for the tractor-implement combination. Simulated and experimental step responses and lateral tracking are performed to validate the models and control methodology. Experimental results show that the implement can be controlled to within 10 cm of the desired path on flat terrain. Finally, Chapter 8 outlines the conclusions of this thesis and presents suggestions future work.



## 1.6 Contributions

- Developed a more accurate yaw dynamic model for the control of farm vehicles. The new model allows an increase in control bandwidth thereby increasing the performance at higher speeds. Identified how the model and parameters change with speed and dual vs. single rear wheels. Developed an analytical model used to describe the yaw dynamics. This new physical understanding of the model and more accurate modeling can be used in determining new higher limits on control performance.
- Developed a cascaded state estimation architecture for estimation of all system biases and states. The cascaded architecture also provides the ability to dead reckon through short GPS outages by explicitly integrating the inertial sensors. Analyzed the ability of the dead reckoning system to provide adequate position and attitude estimates for control of the tractor during short GPS outages. Experimentally verified the estimation scheme and dead reckoning error analysis, showing accurate control of the farm vehicle for short periods without any GPS measurements.
- Analyzed the use of an INS based attitude system as a replacement for the multiple antenna attitude system. Demonstrated accurate control using only a single GPS antenna on the tractor and the INS attitude system. Quantified the importance of a gyroscope for smoothing noisy heading measurements.
- Developed and experimentally validated a method for controlling the position of a towed implement using carrier-phase DGPS position measurements on the towed implement. Verified the use of a simple kinematic model for a towed implement and identified the model parameters for a given implement. Developed the control and estimation equations to perform accurate tracking of the towed implement.

## Chapter 2

# Tractor Yaw Dynamic Modeling

This chapter assesses the impact of the dynamic steering characteristics of a farm tractor for automatic lateral control. It has been shown that the control performance of the tractor decreased with increased speeds using previous models [Elkaim, 1997]. A system identification approach [Ljung, 1987] is used to identify the yaw dynamics of the farm tractor in order to improve automatic control at higher speeds and understand controller limitations due to neglecting the yaw dynamics. Input and output data is analyzed in order to obtain the dominating dynamics from the input to output. In this chapter the yaw model is shown to be dominated by second order dynamics. An analytical model which includes a front tire relaxation length is seen to capture the characteristics of the tractor's yaw dynamics. The system identification tools are then used to identify the parameters of this analytical model with a front tire relaxation length.

The yaw dynamic models are identified for multiple speeds to show the effect of velocity on the model. Particular attention is given to the change in dynamics at speeds in the range of 12-18 mph where automatic control of farm operations such as spraying would be useful. In order to increase the controller performance at these speeds, the yaw dynamics must be well modeled. The identified modeled yaw dynamics do not resemble any traditional analytical models. Additionally, the effect of velocity on the closed loop bandwidth of the controller for a given set of Linear Quadratic Regulator (LQR)

controller weights is presented. It is shown that the closed-loop bandwidth approaches the unmodelled yaw dynamics as the vehicle speed increases. Results are given which show that as the closed loop bandwidth of LQR control weights approaches the regime of the unmodelled yaw dynamics, the controller can become unstable. This demonstrates that these dynamics must be accounted for when developing a controller. After obtaining an accurate model describing the yaw dynamics of the tractor, this model was used to produce a controller which improved performance and robustness at all speeds. Finally, results show an improvement of the lateral tracking error (with a decrease in control effort) using the system identified model.

## 2.1 Commonly Used Physical Yaw Dynamic Models

Figure 2.1 shows a schematic of the traditional bicycle (TB) model. The model does not include roll, as with a real bicycle, but simply get its name from the half (or two wheel) vehicle schematic in Figure 2.1. All vectors and angles in the figure are drawn to illustrate positive sign conventions. It is important to note that this sign convention associates positive forces with negative slip angles ( $\alpha$ ) as shown in the linear tire model:

$$\begin{aligned} F_{yf} &= -C_{\alpha f} \alpha_f \\ F_{yr} &= -C_{\alpha r} \alpha_r \end{aligned} \quad (2.1)$$

The front and rear cornering stiffnesses ( $C_{\alpha f}$  and  $C_{\alpha r}$ , respectively) are taken as positive in this convention. Simple Newtonian principles can be used to derive the lateral dynamics of the bicycle model shown in Figure 2.1.

$$\begin{aligned} \sum F_y &= ma_y = m(\dot{V}_y + V_x r) = F_{yf} + F_{yr} = -C_{\alpha f} \alpha_f - C_{\alpha r} \alpha_r \\ \sum M_z &= I_z \dot{r} = aF_{yf} - bF_{yr} = -aC_{\alpha f} \alpha_f + bC_{\alpha r} \alpha_r \end{aligned} \quad (2.2)$$

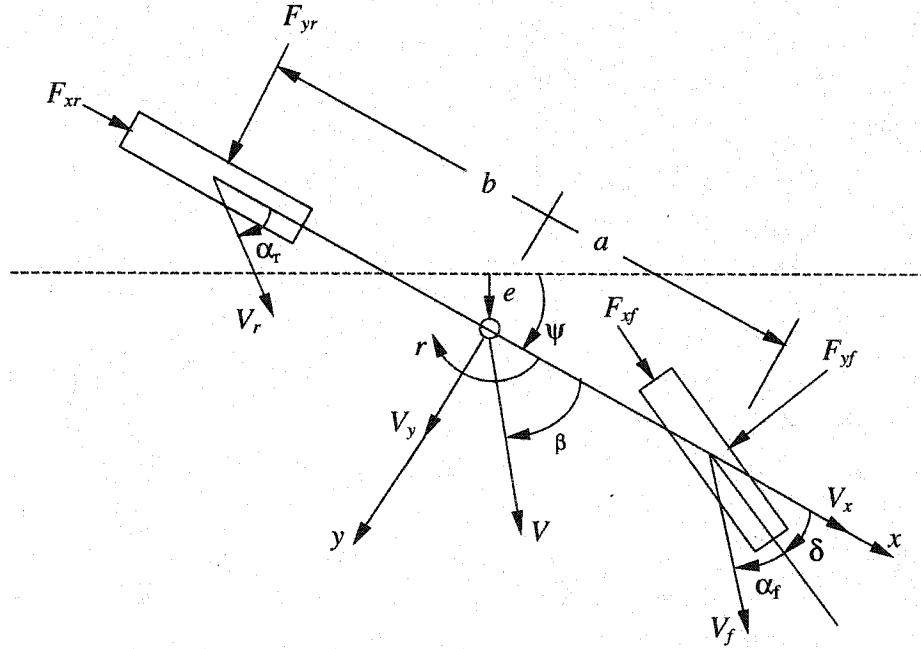


Figure 2.1 Schematic of the Bicycle Model.

The front and rear tire slip angles, for small angles, can be approximated as:

$$\begin{aligned}\alpha_f &\approx -\delta + \left( \frac{V_y + ar}{V_x} \right) \\ \alpha_r &\approx \frac{V_y - br}{V_x}\end{aligned}\quad (2.3)$$

Collecting terms results in the state space representation of the vehicle's lateral dynamics.

$$\begin{bmatrix} \dot{V}_y \\ \dot{r} \end{bmatrix} = \begin{bmatrix} \frac{-C_{af} - C_{ar}}{mV_x} & -V_x + \left( \frac{C_{ar}b - C_{af}a}{mV_x} \right) \\ \frac{C_{ar}b - C_{af}a}{I_z V_x} & \frac{-C_{af}a^2 - C_{ar}b^2}{I_z V_x} \end{bmatrix} \begin{bmatrix} V_y \\ r \end{bmatrix} + \begin{bmatrix} \frac{C_{af}}{m} \\ \frac{C_{af}a}{I_z} \end{bmatrix} \delta \quad (2.4)$$

This linear model is often used in the control and estimation of highway vehicles and is only valid for small slip angles, small steer angle inputs, and within the linear range of the tire model described by Equation (2.1). The above state space model can be rearranged to produce the second order traditional bicycle (TB) yaw rate model shown in Equation (2.5) [Dixon, 1996].

$$\frac{r(s)}{\delta(s)} = \frac{aC_{\alpha f}s + \frac{LC_{\alpha f}C_{\alpha r}}{mV_x}}{I_zs^2 + \frac{c_0I_z + mc_2}{mV_x}s + \left( \frac{c_0c_2 - c_1mV_x^2 - c_1^2}{mV_x^2} \right)} \quad (2.5)$$

where:

$a$  = distance from the front axle to the CG  
 $L$  = wheel base length  
 $C_{\alpha f}, C_{\alpha r}$  = front and rear tire cornering stiffnesses  
 $m$  = vehicle mass  
 $I_z$  = yaw moment of inertia of the vehicle  
 $V_x$  = forward velocity  
 $c_0 = C_{\alpha f} + C_{\alpha r}$   
 $c_1 = aC_{\alpha f} - bC_{\alpha r}$   
 $c_2 = a^2C_{\alpha f} + b^2C_{\alpha r}$

A special case of the bicycle model is created when the understeer gradient is equal to zero (known as neutral steer). For neutrally steering vehicles, the above bicycle model simplifies to the neutral steer (NS) model given below:

$$\frac{r(s)}{\delta(s)} = \frac{aC_{\alpha f}}{I_zs + \frac{c_2}{V}} \quad (2.6)$$

This model represents a first order lag from steer angle to yaw rate as was used in [Rekow, 1999].

A simple kinematic (SK) model which assumes the yaw rate is directly proportional to the yaw rate has been used to model some off road vehicles including a combine [Cordesses, 1999]. This model is derived by assuming no side slip (or lateral velocity) at the tires and can adequately model the vehicle at low speed, low frequency maneuvers. The SK model is given in Equation (2.7) below:

$$\frac{r(s)}{\delta(s)} = \frac{V_x}{L} \quad (2.7)$$

## 2.2 System Identification of the Yaw Dynamic Model

A system identification approach was used to improve control (especially at higher speeds) of the John Deere 8400 tractor discussed in Appendix A. Figure 2.2 shows a schematic of the equipment used to collect the data for the system identification. The tractor uses a linear potentiometer to measure the steering wheel angle while an electrically actuated steering valve is used to provide a steering slew rate when the tractor is operating under closed loop control. A Motorola 68HC12 microprocessor interacts with the steering valve and potentiometer and communicates with the master computer via a serial bus. A delay in the steer angle measurement was discovered and quantification of this delay was performed (as discussed in Appendix B) in order to account for this effect. A sampling of measurements was taken directly into the computer analog to digital converter to verify the results obtained from the HC12. The master computer runs the control and estimation algorithms at a 10 Hz update rate using a Lynx real time operating system; measurements for the system identification were taken at 20 Hz. A KVH fiber optic gyroscope (FOG) was used for sensing yaw rates. Although off-road vehicles are subject to large amounts of mechanical vibrations, the non-mechanical FOG can provide excellent yaw sensing under these conditions. The  $1\sigma$  sensor noise of the FOG is 0.44 deg/s. A more detailed analysis of the FOG noise can be found in [Gebre-Egziabher, 2001(a)].

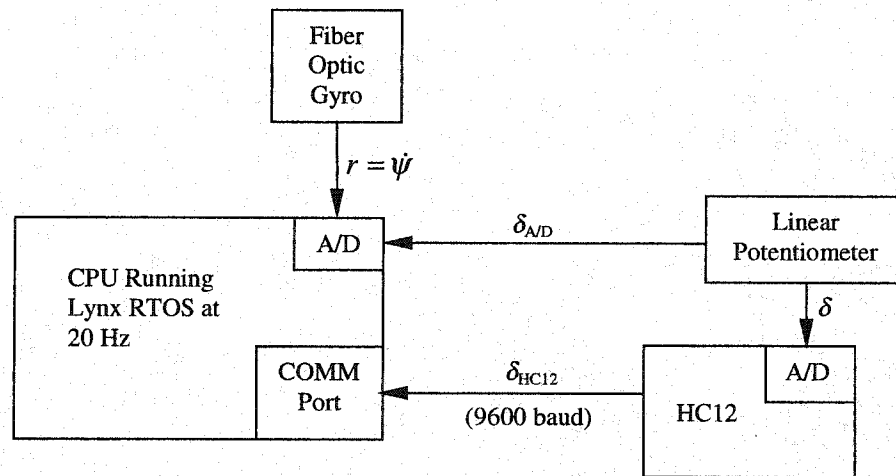


Figure 2.2 Schematic of Data Acquisition for System Identification.

Figure 2.3 shows a schematic of an off-road vehicle including the center of gravity (CG) of the vehicle. The wheel base length ( $L$ ) as well as the distance from the front and rear axles to the vehicle CG ( $a$  and  $b$ , respectively) is shown in the figure. A system identification approach was decided upon to identify the characteristics of the yaw dynamics from steer angle ( $\delta$ ) to yaw rate ( $r=\dot{\psi}$ ) for the tractor at different velocities.

Steer angles were commanded by the Deere 8400 driver while running at various constant speeds on a dirt road, paved highway and tilled field. Because it is important to get a good range of input frequencies, special care was taken in providing the input signal to the steer angle to excite the yaw dynamics. The input to output data was the steer angle to yaw rate (measured from the FOG). The mean was subtracted from the data in order to remove any biases present. Once the input/output data was obtained, several model types were utilized to determine the best model type to be used to fit the data.

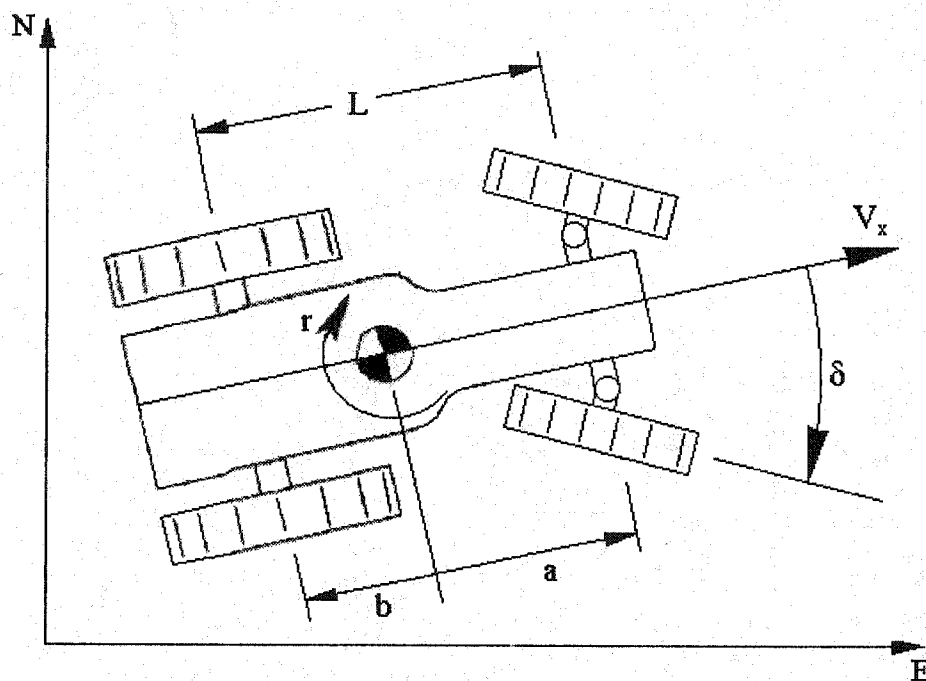


Figure 2.3 Schematic of a Farm Tractor.

A Box-Jenkins model shown in Equation (2.8) [Ljung, 1987], provided the best model fit of the experimental data.

$$r(k) = \frac{B(q)}{A(q)} \delta(k) + \frac{C(q)}{D(q)} e(k) \quad (2.8)$$

where:  $r$  = yaw rate

$\delta$  = steer angle input

$e$  = noise

$B(q)$ ,  $C(q)$ ,  $D(q)$ ,  $A(q)$  are polynomials (of the shift operator,  $q$ ) describing the transfer function between the inputs and output

For a few data runs, the Box-Jenkins model could not adequately fit the data. For these data sets, an ARMAX model fit was used. The ARMAX model fit is similar to the Box-Jenkins fit shown in Equation (2.8) with the constraint that  $A(q)=D(q)$  [Ljung, 1987].

### 2.2.1 Identification with Single Rear Wheels

Figure 2.4, shows a typical spectral analysis in magnitude and phase (empirical transfer function using MATLAB's ETFE command) of the experimental input to output data. The figure also shows the second order identified (ID2) fit of the input-output data. The noise in the empirical transfer function above 10 rad/s is due to the lack of input signal at those frequencies. In the 8400 tractor, it is quite difficult to input steer angle rates above 10 rad/s. However, this input range was sufficient to capture the second order peak at 6 rad/s shown in the figure.

Figure 2.5 shows the modeling errors from various order fits. Also shown are the errors from model fits with one zero in the numerator. The increase in model errors from model fits above second order ( $N>2$ ) is due to the model attempting to fit the high frequency noise, which sacrifices the fit of the actual second order dynamics seen in Figure 2.4.



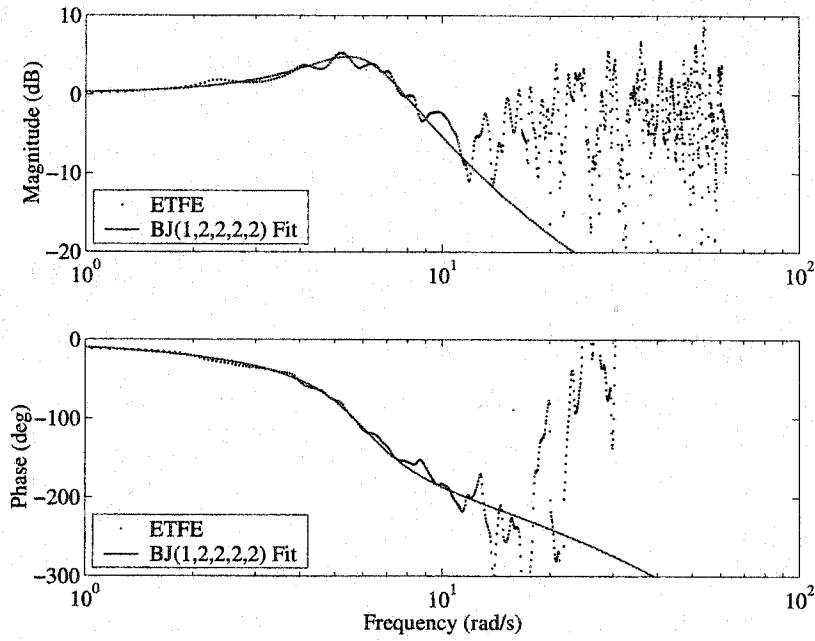


Figure 2.4 Spectral Analysis and Box Jenkins Second Order Fit of the Input ( $\delta$ ) to Output ( $r$ ) Data.

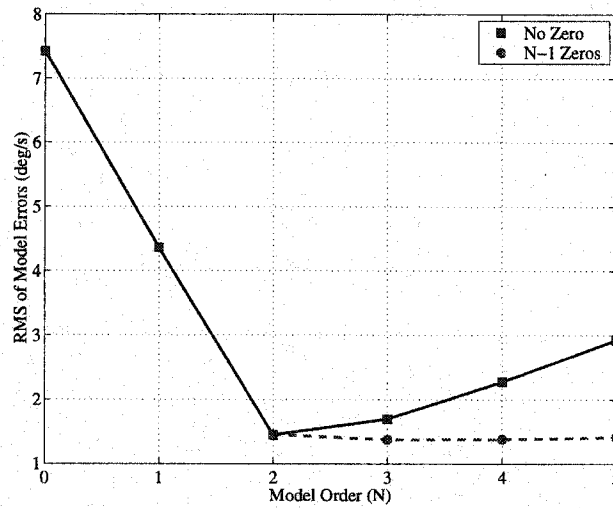


Figure 2.5 Model Errors vs. System Identified Model Order for No Zeros and N-1 Zeros for Single Rear Wheels.

Because the zero did not increase the accuracy of the model fit, a second order fit, with two time delays, was used to model the tractor yaw dynamic data. The second order fit was of the form:

$$R(k) = \frac{K}{q^2 + \gamma q + \lambda} \delta(k) \quad (2.9)$$

The variables  $K$ ,  $\gamma$ , and  $\lambda$  are simply constants that describe a transfer function with two poles and no zeros.

Figure 2.6 shows an example run (at 4 m/s) along with a simple gain (ID0), first order (ID1), and second order (ID2) identified model fits. The first and second order models were determined using the Box-Jenkins model fit. The ID1 fit assumes the model is of the form of the neutral steer vehicle model given in Equation (2.6). The gain for the zero order model was calculated using least squares to fit the ID0 model shown in Equation (2.10).

$$\psi = K_{R_0} \delta \quad (2.10)$$

As seen in Figure 2.6, the phase lag is quite apparent at the higher frequency inputs. Additionally, the resonance peak of the system at 6 rad/s can be seen in the data at about  $t=30$  seconds.

Figure 2.7 shows how the frequency response of the ID2 model changes for different velocities for data runs at 2, 4, 6, and 8 m/s. It is important to notice the increasing phase lag with increasing speed below 5 rad/s. This shows that compensators with a closed loop bandwidth below 5 rad/s will become more oscillatory at higher speeds if these dynamics are not taken into account.

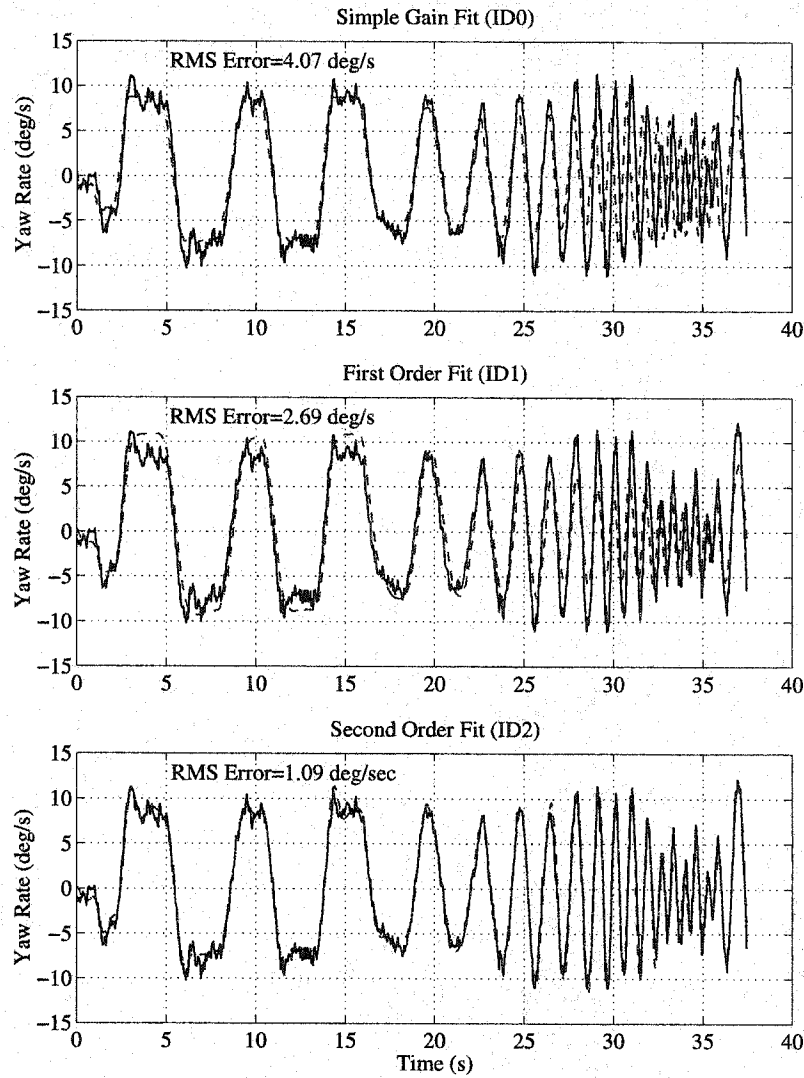


Figure 2.6 Modeled Yaw Rate Output for a Zero Order, First Order and Second Order Model Fits Versus Actual Yaw Rate (Actual – Solid Line).

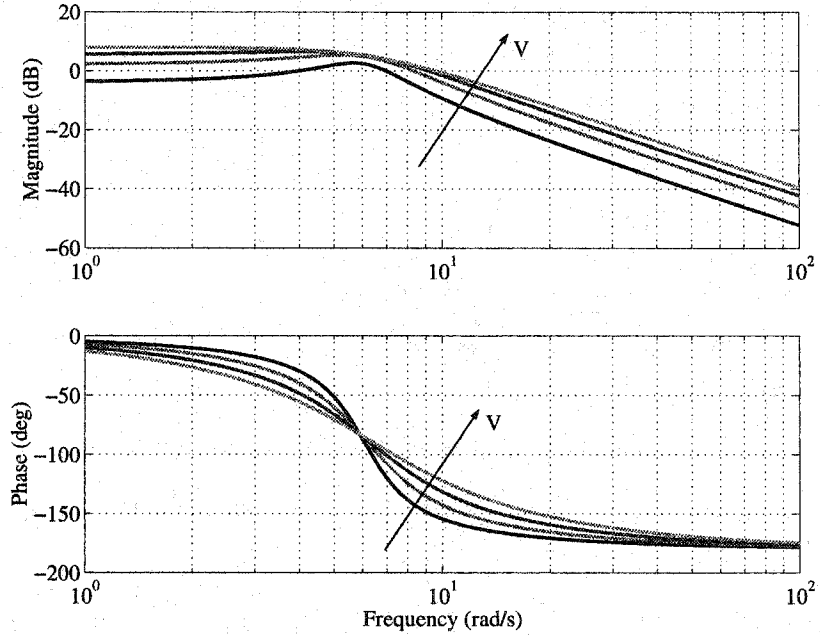


Figure 2.7 ID2 Model Frequency Responses vs. Velocity for  $V_x=2,4,6$ , and 8 m/s for Single Rear Wheels.

### 2.2.2 Identification with Dual Rear Wheels

As an additional verification, the yaw dynamics of the tractor with dual rear wheels (which are often used to increase traction) were also identified. Analytically, the addition of dual rear wheels has the effect of doubling the rear cornering stiffness. Therefore, the identified model with duals should be predicted by doubling the analytical model's rear cornering stiffness and determining if the same trends exist between the analytical and identified model with single and duals.

Figure 2.8 shows the modeling errors from various order fits. As with single rear wheels, a second order model with no zeros is a good choice of the model fit. Figure 2.9 shows how the frequency response of the ID2 model changes for data runs at 2, 4, 6, and 8 m/s with dual rear wheels.

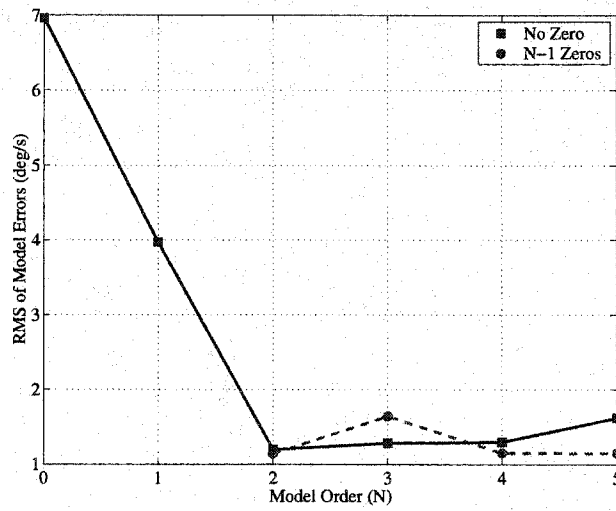


Figure 2.8 Model Errors vs. System Identified Model Order for No Zeros and N-1 Zeros for Dual Rear Wheels.

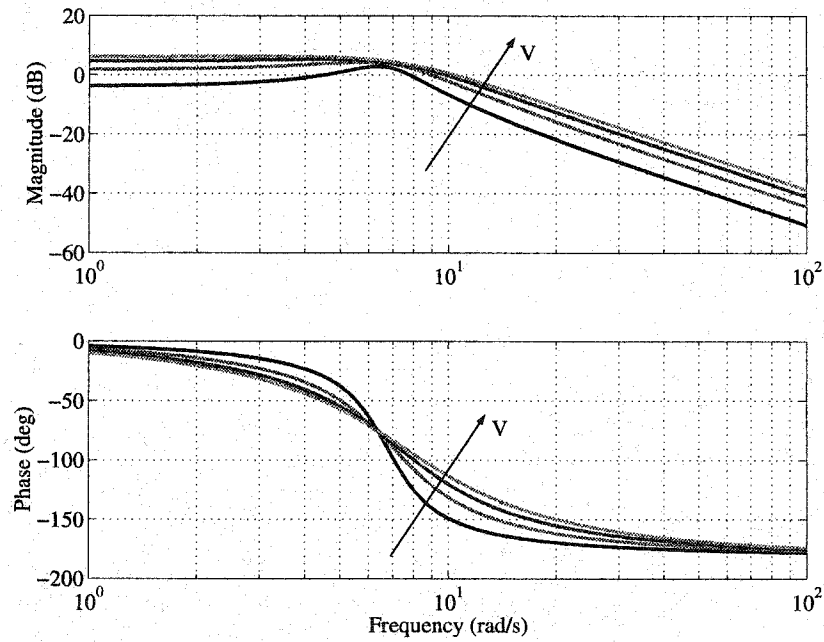


Figure 2.9 ID2 Model Frequency Responses vs. Velocity for  $V_x=2,4,6$ , and 8 m/s for Dual Rear Wheels.

## 2.3 New Yaw Dynamic (NYD) Model

Once the model form was determined, several experimental runs were performed over the range of vehicle speeds in order to determine how the parameters of the ID2 change with velocity. The natural frequency ( $\omega_n$ ), damping ratio ( $\zeta$ ), and DC gain ( $R_{ss}$ ) were calculated for each of the yaw dynamic transfer functions. Figure 2.10 shows the changes in the parameters from the ID2 model versus velocity for these various experimental runs together with a least squares fit of the data. This figure is an attempt to fit the system identified model to the form described by the traditional bicycle model in Equation (2.5).

An important parameter in describing the turning response of a vehicle is the understeer gradient. Methods for experimental measurement of the understeer gradient ( $K_{us}$ ) are based on the following definition [Gillespie, 1992]:

$$\delta = 57.3 \frac{L}{R} + K_{us} a_y \quad (2.11)$$

where  $R$  is the radius of turn and  $a_y$  is the lateral acceleration. Alternatively the understeer gradient for the tractor can be estimated from the steady state yaw rate ( $r_{ss}$ ) versus forward velocity ( $V_x$ ) by rewriting Equation (2.11) to form:

$$r_{ss} = K_R \delta = \frac{V_x}{L + K_{us} V_x^2} \delta \quad (2.12)$$

Fitting the steady state response versus velocity resulted in an understeer gradient of 1.4 deg/g, which, as shown in Figure 2.10, gives approximately the same steady-state yaw rate response as a neutrally steering vehicle over this speed range. A least square fit was used to solve for the understeer gradient as well as the wheel base length ( $L$ ) in Equation (2.12). Although the wheel base length can be measured directly, solving for  $L$  provides some validity to the fit. The resulting wheel base length was 3.06 m which is within 5% of the actual wheel base length (2.95 m). Note that Equation (2.12) does not account for effects such as roll steer or camber effects. However, the fact that the solution of the wheel base length is close to the actual wheel base, demonstrates the validity of the form given in Equation (2.12)

The overall model fit of the tractor yaw dynamics is described by Equation (2.13).

$$r(s) = \frac{K_R \omega_n^2}{s^2 + 2\zeta \omega_n s + \omega_n^2} \delta(s) \quad (2.13)$$

where:

$$K_R = \frac{V_x}{L + K_{US} V_x^2} \quad (2.14)$$

The values for  $K_{US}$ ,  $\omega_n$ , and  $\zeta$  are a function of velocity and are determined from a least squares fit of the ID2 models. The natural frequency ( $\omega_n$ ) was fit using a first order polynomial and the damping ratio ( $\zeta$ ) was fit using a second order polynomial. These polynomial fits are a function of velocity as seen in Figure 2.10 for single rear wheels. These ensemble best fits of the ID2 data are used to form the new yaw dynamic (NYD) model for the 8400.

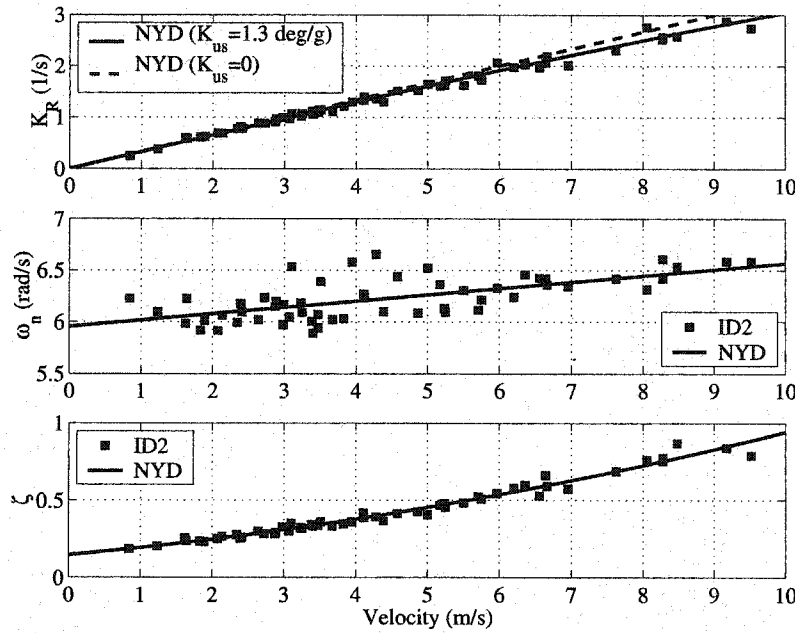


Figure 2.10 ID2 Data and Best Fit (NYD) Model Parameters vs. Velocity for Single Rear Wheels.

Figure 2.11 shows the changes in the parameters from the ID2 model versus velocity for multiple experimental runs with dual rear wheels. As with the single rear wheels shown in Figure 2.10, this figure is an attempt to fit the system identified model to the

form described by the bicycle model in Equation (2.5). Fitting the steady state response versus velocity now results in an understeer gradient ( $K_{us}$ ) of 7.5 deg/g. Although the pole location characteristics can not be described by the bicycle model, the change in the understeer gradient can be predicted by the bicycle model. Table 2.1 lists the data used to produce the NYD model fits seen in Figure 2.10 and 2.11 for single and dual rear wheels, respectively.

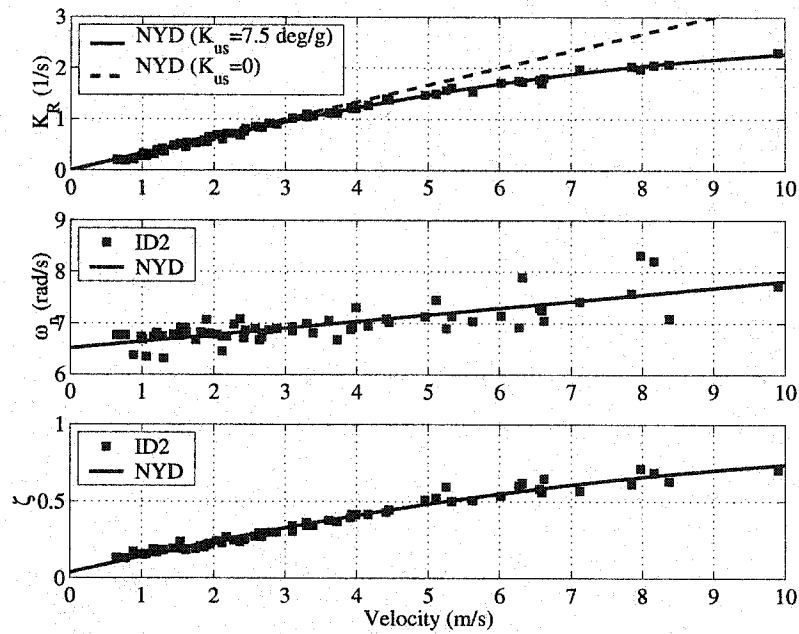


Figure 2.11 ID2 Data and Best Fit (NYD) Model Parameters vs. Velocity for Dual Rear Wheels.

Table 2.1 Model Parameters for the NYD Model.

Parameter	Single Rear Wheels	Dual Rear Wheels
$L$ (m)	3.0567	3.0647
$K_{us} \left( \frac{rad \cdot s^2}{m} \right)$	0.0023	0.0134
$\omega_n$ (rad/s)	$0.0613V_x + 5.9548$	$0.1301V_x + 6.5095$
$\zeta$	$0.0036V_x^2 + 0.0436V_x + 0.1458$	$-0.0038V_x^2 + 0.1079V_x + 0.0374$



Model errors are taken to be the RMS errors between the actual and model yaw rates. Because all biases (averages) have been removed from the data, all errors and yaw rate outputs can be assumed to be zero mean. Because data runs performed at lower speeds have less yaw rate output, it was desired to normalize the errors according to the amount of output for a given run. The model errors were therefore normalized by dividing the RMS errors by the RMS of the yaw rate output as shown below.

$$\text{Normalized Errors} = \frac{\text{RMS}\{R_{\text{actual}} - R_{\text{model}}\}}{\text{RMS}\{R_{\text{actual}}\}} \times 100\% \quad (2.15)$$

Figures 2.12 and 2.13 show the modeling errors from the ID2 and NYD models for single and dual rear wheels.

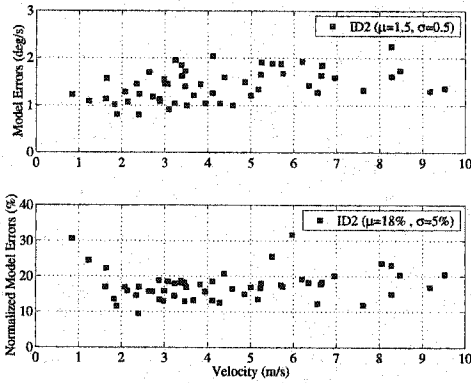


Figure 2.12a Model Errors and Normalized Model Errors for the ID2 Model with Single Rear Wheels.

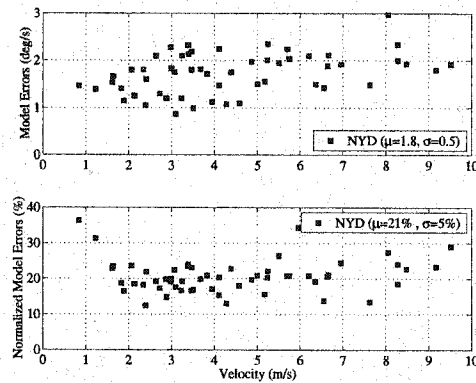


Figure 2.12b Model Errors and Normalized Model Errors for the NYD Model with Single Rear Wheels.

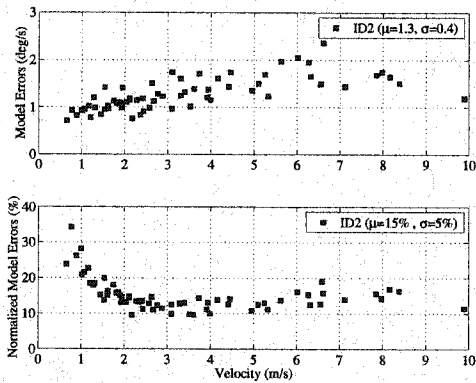


Figure 2.13a Model Errors and Normalized Model Errors for the ID2 Model with Dual Rear Wheels.

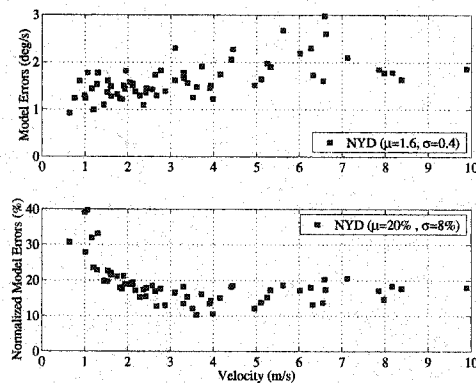


Figure 2.13b Model Errors and Normalized Model Errors for the NYD Model with Dual Rear Wheels.

## 2.4 Bicycle Model with Tire Relaxation Lengths

No choice of physical parameters for the TB model given in Equation (2.5) can capture the dynamics seen in the system identification of the tractor. Reproducing the understeering behavior of the tractor with the traditional bicycle model results in damping that decreases as speed increases. Clearly, the identified system exhibits the opposite behavior. Previous research in agricultural wheeled vehicles has suggested that a relaxation length of the tire contributes to an increase in yaw damping at higher speeds [Crolla, 1982 & Owen, 1982]. The relaxation length ( $\sigma$ ) is the amount a tire must roll in order to generate the steady state slip angle at the tire ( $\alpha_0$ ). A first order model due to the tire relaxation length can be used to described the slip angle ( $\alpha$ ) dynamics as shown below in Equation (2.16).

$$\dot{\alpha} = \frac{V_x}{\sigma}(\alpha_0 - \alpha) \quad (2.16)$$

A side slip angle at the tire is required to generate a side force at the tire. Under a simple linear tire model, the lateral force at the tire is proportional to the slip angle (as shown previously in Equation (2.1)). This proportionality constant is known as the tire cornering stiffness. The authors in [Owen, 1982] use the relaxation length to develop the following tire relaxation (TR) model for a tractor:

$$\begin{bmatrix} \dot{V}_y \\ \dot{r} \\ \dot{\alpha}_f \\ \dot{\alpha}_r \end{bmatrix} = \begin{bmatrix} 0 & -V_x & \frac{-c_{\alpha f}}{m} & \frac{-c_{\alpha r}}{m} \\ 0 & 0 & \frac{-c_{\alpha f}a}{I_z} & \frac{-c_{\alpha r}b}{I_z} \\ 1/\sigma_f & a/\sigma_f & -V_x/\sigma_f & 0 \\ 1/\sigma_r & -b/\sigma_r & 0 & -V_x/\sigma_r \end{bmatrix} \begin{bmatrix} V_y \\ r \\ \alpha_f \\ \alpha_r \end{bmatrix} + \begin{bmatrix} 0 \\ 0 \\ -V_x \\ \sigma_r \end{bmatrix} \delta \quad (2.17)$$

where

$b$  = distance from the rear axle to the CG

$V_y$  = lateral velocity of the vehicle at the CG

$\alpha_f, \alpha_r$  = front and rear tire side slip angles

$\sigma_f, \sigma_r$  = front and rear tire relaxation lengths

$C_{\alpha f}, C_{\alpha r}$  = front and rear tire cornering stiffnesses

Figure 2.14 shows how the frequency response of a vehicle modeled by Equation (2.17) changes with velocity from 2 m/s to 8 m/s. The specific parameters used in the models in this thesis are given in the preceding section in Table 2.2. Alternatively, estimates of model parameters for a similar vehicle (loader backhoe) can be found in [Owen, 1982]. In order to obtain similar changes in damping versus velocity, a tire relaxation length of 1.4-1.7 times the tire radius was used. This is approximately two to three times what has been observed by other researchers for passenger cars [Loeb, 1990]. Additional research has found that a second order slip angle model (as opposed to the first order model shown in Equation (2.16)) was needed to accurately describe the tire dynamics [Heydinger, 1991]. It is important to note that at higher speeds, the amount of time necessary for the tire to travel the required distance to create a slip angle decreases. This decreases the effect of the tire relaxation parameter at higher speeds and for smaller diameter tires, explaining why relaxation length is neglected in most passenger car models where speeds of concern are typically over 15 m/s. As seen in Figure 2.14, this model correctly shows the increase in damping at higher speeds as seen in the NYD model in Figure 2.10 for single rear wheels and Figure 2.11 for dual rear wheels.

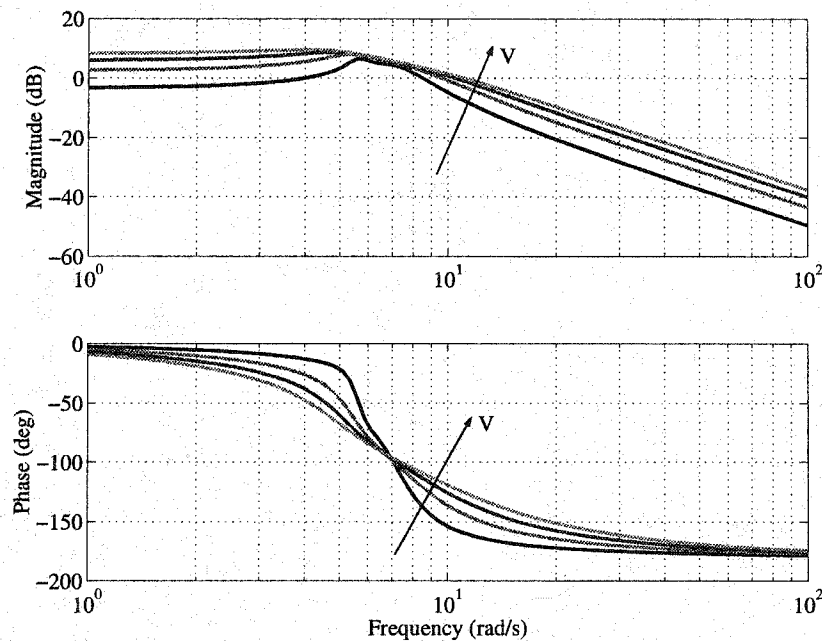


Figure 2.14 TR Model Frequency Response vs. Velocity for  $V_x=2,4,6$ , and 8 m/s.

A simplification of the tire relaxation model can be made by assuming only a tire relaxation length at the front tire. This results in the front tire relaxation (FTR) model given below in Equation (2.18).

$$\begin{bmatrix} \dot{V}_y \\ \dot{r} \\ \dot{\alpha}_f \end{bmatrix} = \begin{bmatrix} \frac{c_{\alpha r}}{mV_x} & -V_x + \frac{c_{\alpha r}b}{mV_x} & \frac{-c_{\alpha f}}{m} \\ \frac{c_{\alpha r}b}{I_z V_x} & \frac{-c_{\alpha r}b^2}{I_z V_x} & \frac{-c_{\alpha f}a}{I_z} \\ \frac{1/\sigma_f}{a/\sigma_f} & \frac{a/\sigma_f}{-V_x/\sigma_f} & -V_x/\sigma_f \end{bmatrix} \begin{bmatrix} V_y \\ r \\ \alpha_f \end{bmatrix} + \begin{bmatrix} 0 \\ 0 \\ -\frac{V_x}{\sigma_f} \end{bmatrix} \delta \quad (2.18)$$

As seen in Figure 2.15, the FTR model also exhibits the similar increase in damping at higher speeds.

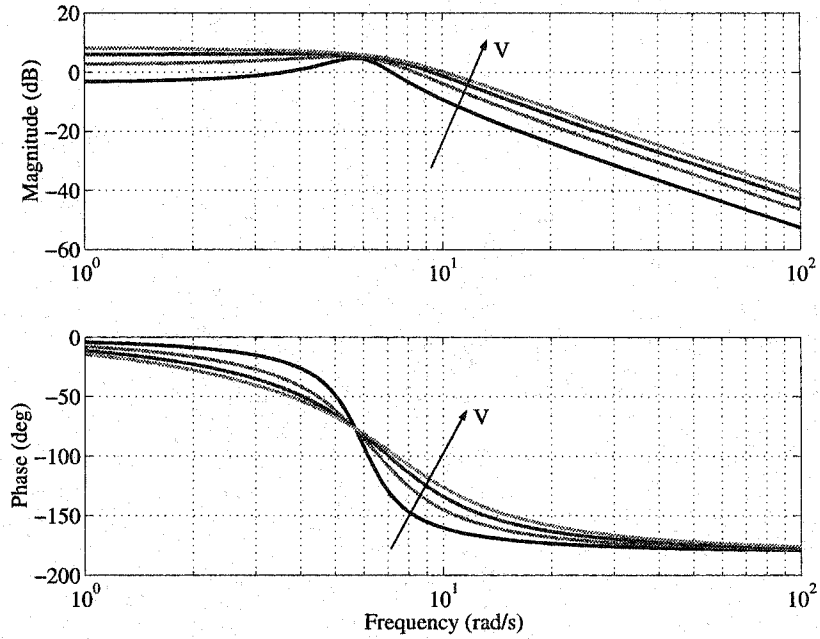


Figure 2.15 FTR Model Frequency Response vs. Velocity for  $V_x=2, 4, 6$ , and  $8$  m/s.

## 2.5 Physical Model Parameter Identification/Selection

Because the understeer gradient was obtained for single and dual rear wheels, it is possible to solve for the cornering stiffnesses as a function of CG location. The understeer gradient for single rear wheels can be described using the front and rear axle weights ( $W_f$  and  $W_r$ ) and the front and rear cornering stiffnesses as shown below [Gillespie, 1992].

$$K_{us}^{singles} = \frac{W_f}{c_{of}} - \frac{W_r}{c_{or}} = \frac{\left(\frac{b}{L}\right)m}{c_{of}} - \frac{\left(\frac{a}{L}\right)m}{c_{or}} = \frac{\left(\frac{b}{L}\right)m}{c_{of}} - \frac{\left(\frac{L-b}{L}\right)m}{c_{or}} \quad (2.19)$$

Similarly, under the assumption that adding dual rear wheels doubles the rear cornering stiffness, the understeer gradient for dual rear wheels is given as:

$$K_{us}^{duals} = \frac{\left(\frac{b}{L}\right)m}{c_{of}} - \frac{\left(\frac{L-b}{L}\right)m}{2 \times c_{or}} \quad (2.20)$$

Equation (2.20) assumes that each of the dual rear wheels have the same effective cornering stiffness. This may not be true if the tires are different or if the lateral forces are not taken up evenly on each tire. The front and rear cornering stiffnesses can then be solved (by solving Equation (2.19) and (2.20) simultaneously) as a function of CG location ( $b$ ). Figure 2.16 shows the solution of the front and rear cornering stiffnesses as a function of the CG location. It is important that these cornering stiffnesses are the total cornering stiffness *at the axle*, and not the value of the cornering stiffness per tire. The location of the CG of the tractor was estimated to be approximately one meter in front of the rear axle ( $b = 1$  m). Therefore tire cornering stiffnesses associated with this CG location were chosen. This corresponds to nearly the same rear tire cornering stiffness that was observed for a similar size rear tire in the loader backhoe example given in [Owen, 1982]. The FTR model was compared using tire cornering stiffnesses associated with various CG locations. However, there was little difference observed in the FTR model's pole locations as a result of varying the CG location.

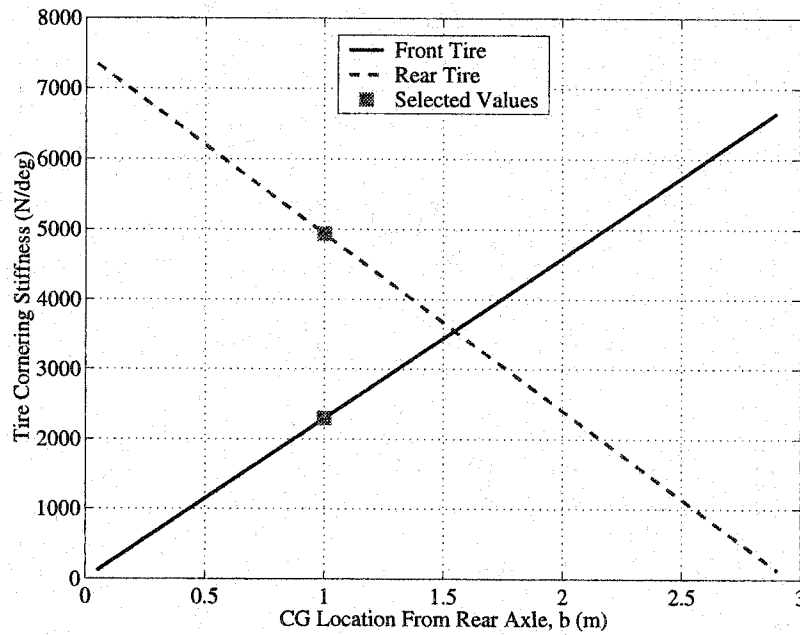


Figure 2.16 Front and Rear Tire Cornering Stiffness vs. Tractor CG Location.

An estimate of the vehicle's yaw inertia can be made knowing the vehicle mass and CG location using the following approximation given in [Garrott, 1988].

$$I_z \approx m \times a \times b \quad (2.21)$$

The selected tire cornering stiffness along with the other model values are given in Table 2.2. The values for the front and rear tire relaxation lengths were approximated such that the models matched the observed (ID2) data. It is interesting that the best fit for the FTR model required the front tire relaxation length to decrease for the case with dual rear wheels. It is uncertain if this effect is due to adding the dual rear wheels, or a change in test conditions for data taken with dual rear wheels. As mentioned previously, data runs with single rear wheels were taken on paved highway, dirt road and tilled field. However, data with dual rear wheels was only taken on a paved highway after the vehicle had been shipped. Tire pressures may have been altered during shipping, which could also change the tire relaxation length.

Table 2.2 Parameters Used for the Physical Models.

Parameter	Units	Single Rear Wheels	Dual Rear Wheels
$\sigma_f$ (FTR Model)	m	1.1874 (1.7 × front tire radius)	0.9779 (1.4 × front tire radius)
$\sigma_f$ (TR Model)	m	0.8382 (1.4 × front tire radius)	0.8382 (1.4 × front tire radius)
$\sigma_r$ (TR Model)	m	1.3513 (1.4 × rear tire radius)	1.3513 (1.4 × rear tire radius)
$C_{\alpha r}$	N/deg	49,370	2 × 49,370
$C_{\alpha f}$	N/deg	22,941	
$a$	m	1.95	
$b$	m	1	
$L$	m	2.95	
$m$	kg	9,500	
$I_z$	kg-m <sup>2</sup>	18,525	

## 2.6 Comparison of Models

Summaries of the physical models and system identified models are given in Table 2.3 and Table 2.4, respectively. The parameters given in Table 2.2 were used for all of the physical models.

Table 2.3 Summary of Physically Derived Models.

Model Name	Model Abbreviation	Equation Number	Model Order
Simple Kinematic	SK	(2.7)	0
Neutral Steer	NS	(2.6)	1
Traditional Bicycle	TB	(2.5)	2
Bicycle Model with Front Tire Relaxation Length Only	FTR	(2.18)	3
Bicycle Model with Front and Rear Tire Relaxation Lengths	TR	(2.17)	4

Table 2.4 Summary of System Identified Models.

Model	Model Form $\left( \frac{R(s)}{\delta(s)} \right)$	Model Order
ID0	$K_{R_0}$	0
ID1	$\frac{K_{R_1}}{\tau_s + 1}$	1
ID2	Equation (2.13)	2
NYD	Equation (2.13) & Table 2.1	2



Figure 2.17 shows how the poles and zeros of the various models change with changing velocity. The model with front and rear relaxation lengths has approximately a complex pole-zero pair cancellation. As a result, a bicycle model which only considers a front tire relaxation length can closely capture the dynamics of the tractor. This can be seen by the fact that the remaining complex poles of the model with only a front relaxation length have similar characteristics to the complex poles of the identified model. This makes physical sense, as the forces at the front tire generate the yaw moment on the tractor. Note that the poles and zeros of the bicycle model fail to even qualitatively describe the identified behavior.

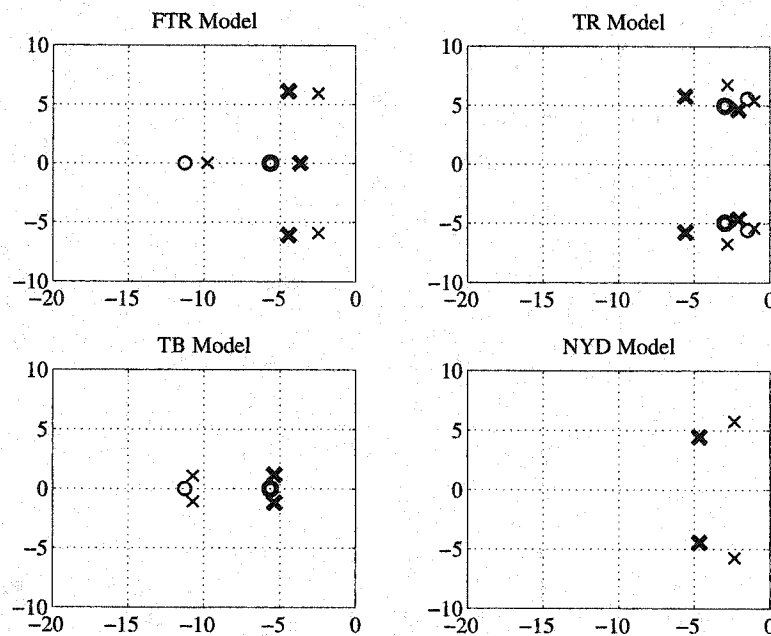


Figure 2.17 Pole-Zero Plot of Various Models at 4 m/s (regular) and 8m/s (bold).

Figure 2.18 shows how the FTR model's dominant second order characteristics change versus velocity (solid lines). The model was simulated with a white noise input and then a best fit second order system was used to model the input/output data of the third order FTR model (in order to get the approximate second order fit of the natural frequency and damping ratio). The figure also contains the actual parameters of each of

the ID2 models for a given velocity as shown previously for single and dual rear wheels in Figures 2.10 and 2.11, respectively. The FTR model for single rear wheels (Figure 2.18a) and dual rear wheels (Figure 2.18b) can also be compared with the NYD system identified model fits in Figures 2.10 and 2.11, respectively. There is incredible agreement between the NYD and FTR models. It is interesting to note that the experimental damping ratio goes from 0.2 to 1.1 for singles and 0.2 to 0.9 for duals as predicted by the FTR model. The FTR model also predicts the steady state yaw rate versus velocity quite well. However, this is not surprising since the physical model parameters were chosen to produce a vehicle with the same understeer characteristics seen in the NYD model.

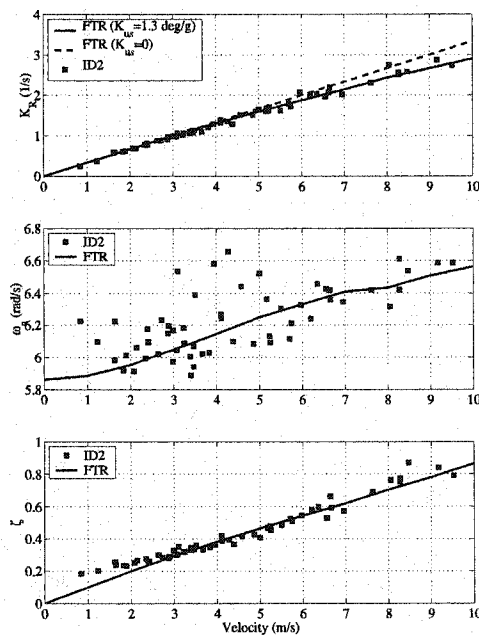


Figure 2.18a ID2 Data and FTR Model Approximation vs. Velocity for Single Rear Wheels.

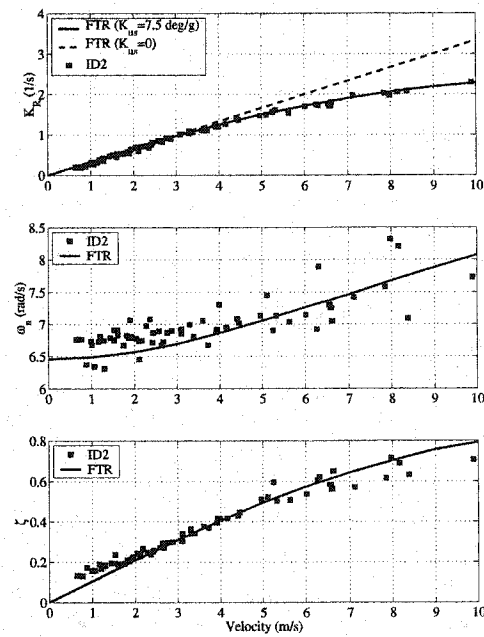


Figure 2.18b ID2 Data and FTR Model Approximation vs. Velocity for Dual Rear Wheels.

The FTR model does not completely match the system identification model shown previously. The largest discrepancy occurs in the natural frequency of the yaw dynamics. However, this discrepancy can be considered quite small with respect to uncertainties in the analytical model parameters as well as errors from unmodelled dynamics using the

simple second order yaw model. An exact analytical model that describes the system identified model may be very difficult to obtain. This is in part because the actual vehicle is comprised of complex dynamics which cannot be captured exactly by the simple linear analytical models given above. Because the analytical models are comprised of many parameters which are generally not well understood (such as the tire relaxation length or cornering stiffness), a system identification approach is necessary.

Additionally, the frequency responses of the analytical model (using only a front tire relaxation length) and the system identified model are compared at 2, 5, and 8 m/s for the case of singles (Figure 2.19a) and duals (Figure 2.19b). As seen in Figure 2.19b, the system identified model and analytical model for the tractor setup with duals agree very well. Again there is a slight discrepancy in the natural frequency as mentioned previously with Figure 2.18. However, since the models are intended for use in closed-loop control, the impact of this difference is minor.

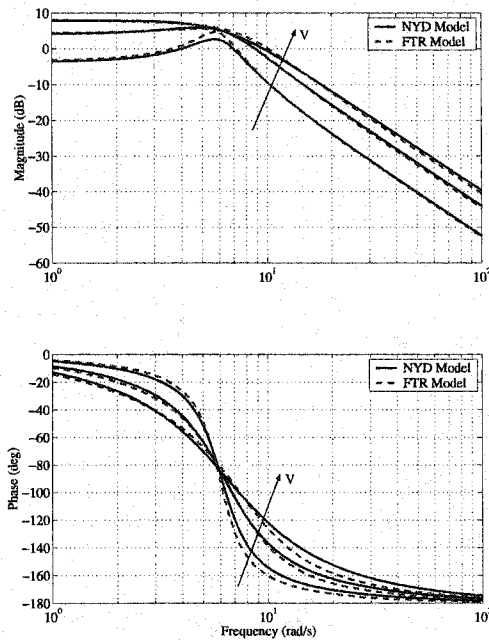


Figure 2.19a Frequency Response Comparison of the FTR and NYD Models at  $V_x=2, 5$  and  $8$  m/s for Single Rear Wheels.

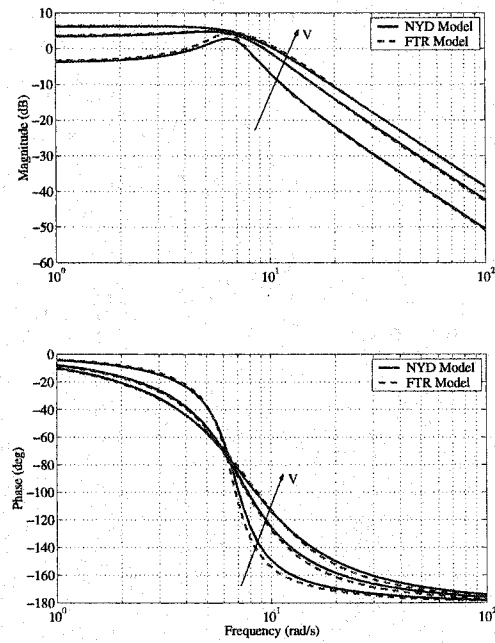


Figure 2.19b Frequency Response Comparison of the FTR and NYD Models at  $V_x=2, 5$ , &  $8$  m/s for Dual Rear Wheels.

Figure 2.20 shows the modeling errors from several models for varying forward velocities of 2, 5, and 8 m/s. It is important to note that the amount of error will greatly depend on the frequency content of each data set. For example, the errors associated with a constant gain fit (ID0) will be significantly less for a run that has more low frequency content than for a run with a larger range of frequency content. The SK model exhibits a noticeable decrease in modeling performance as speed increases. This is because the SK model neglects understeer effects of the vehicle which become more pronounced at higher speeds. Finally, Figure 2.21 shows the modeling errors for the various models for single and dual rear wheels. These errors are the average errors over all data runs from each model type. It is easy to see that the best fit second order model for each data set (ID2) has the lowest modeling errors. However, the NYD and physical FTR models are quite good. In fact, the difference between the ID2, NYD and FTR models is within the noise of a reduced order model of this fidelity. Additionally, the NYD and FTR models have almost 300% and 400% better modeling performance than the TB and SK models, respectively.

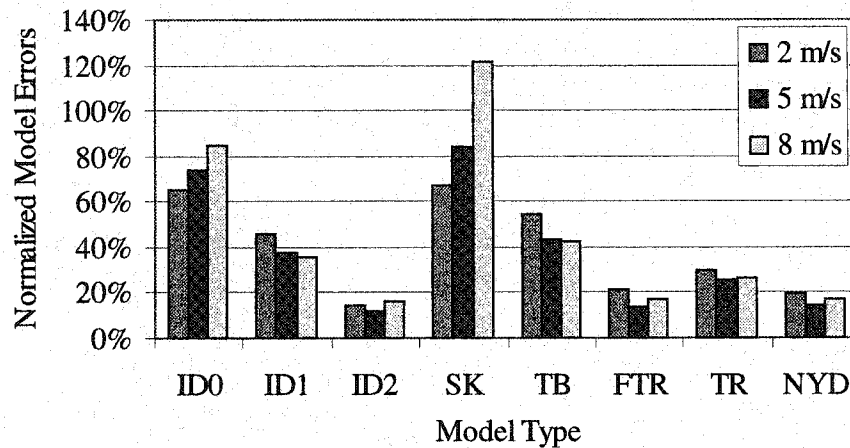


Figure 2.20 Yaw Rate Modeling Errors for Various Model Types at  $V_x=2, 5$  and 8 m/s for Single Rear Wheels.

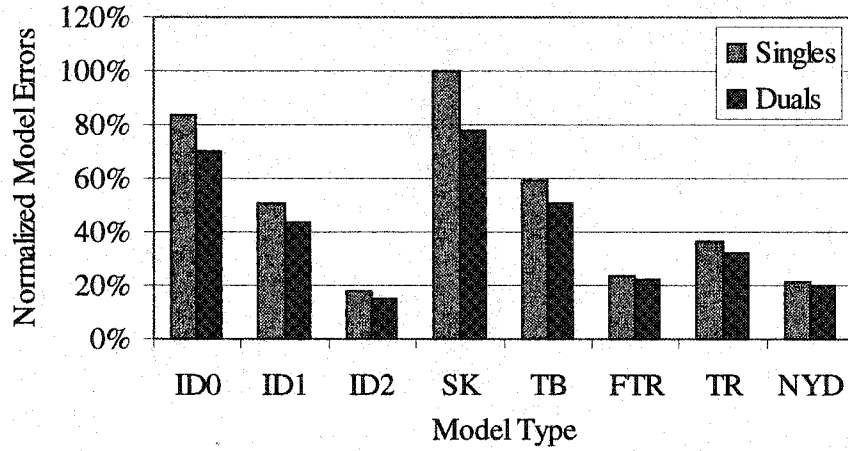


Figure 2.21 Yaw Rate Modeling Errors for Various Model Types Averaged Over all Data Runs for Single and Dual Rear Wheels.

## 2.7 Experimental Control Results

The control input is a pulse width modulated (PWM) signal to a hydraulic valve that controls the steering slew rate of the front tires. The NYD model described by Equation (2.12) must be augmented with additional states and biases resulting in a twelfth order estimator. The estimator is comprised of two cascaded filters in order to estimate all of the states and biases correctly and is presented in Chapter 4. A linear quadratic regulator (LQR) described in Chapter 3 was used to control the lateral error ( $y$ ) of the tractor with the control point at the vehicle CG ( $l_{cp} = 0$ ). The following weighting matrices were used in designing the LQR feedback gains in order to compare the control accuracy of various models at high speeds.

$$\begin{aligned}
 Q_x &= \text{diag}[Q_y \quad Q_\psi \quad Q_{\dot{\psi}} \quad Q_{\ddot{\psi}} \quad Q_\delta \quad Q_{\dot{\delta}}] \\
 &= \text{diag}[1 \quad 0 \quad 0 \quad 0 \quad 0 \quad 0] \\
 R_u &= 0.1
 \end{aligned} \tag{2.22}$$

Specifics about the LQR weights and control algorithm are given in Chapter 3.

Figure 2.22 shows how the closed loop bandwidth (given from the dominant eigenvalue pair of  $A - B \times K_{comp}$ ) of the system changes with speed and changing  $R_u$  ( $Q_x$  remains constant at the values shown in Equation (2.22)). This figure shows that the LQR weights of the controller must be decreased as speed increases in order to maintain the same closed loop bandwidth. Therefore, if the lateral dynamics identified earlier in this chapter (occurring at 6 rad/s) are not modeled, a restriction must be placed on the bandwidth of the controller in order to ensure stability.

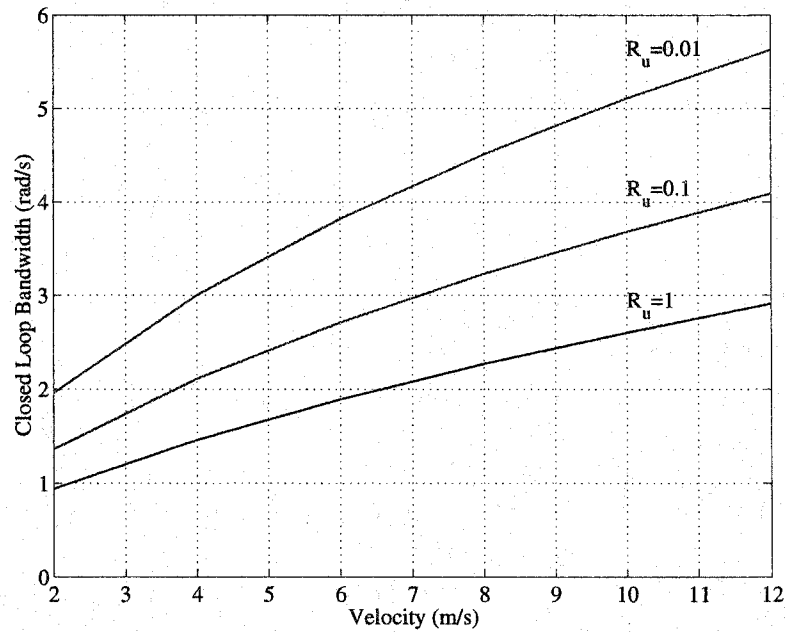


Figure 2.22 Resulting Closed-Loop Bandwidth vs. Velocity Using LQR.

Controllers for the tractor based on the simple kinematic (SK), first order (ID1), and new yaw dynamic (NYD) models were implemented on the experimental system. The tractor was given a line trajectory to follow and time was given to allow the bias estimations to settle. Figures 2.23-2.25 show the lateral error and control effort for experimental runs at 5 m/s using an SK model (used in [O'Conner, 1996]), first order (ID1) model (used in [Rekow, 1999]), and the higher order model developed from system identification (NYD). The LQR weights shown in Equation (2.22) were used in these

runs. As seen in Figure 2.23, the SK model controller is unstable at 5 m/s. Stability of the SK model was recovered when the LQR weights were decreased (lowering the closed loop bandwidth). However, lowering the bandwidth of the controller will lead to a decrease in control performance. The ID1 model is stable (Figure 2.24). However, the effect of the unmodelled dynamics can easily be seen by the large limit cycle in the control effort. The performance of the controller using the NYD model is shown in Figure 2.25. The controller improvement from using the NYD model is quite apparent even at 5 m/s. Note that a small improvement in the  $1\sigma$  control accuracy results in significant benefit in precision agricultural applications [Rekow, 2001]. Finally, the controller using the NYD model for a run at 16 mph (8 m/s) is shown in Figure 2.26.

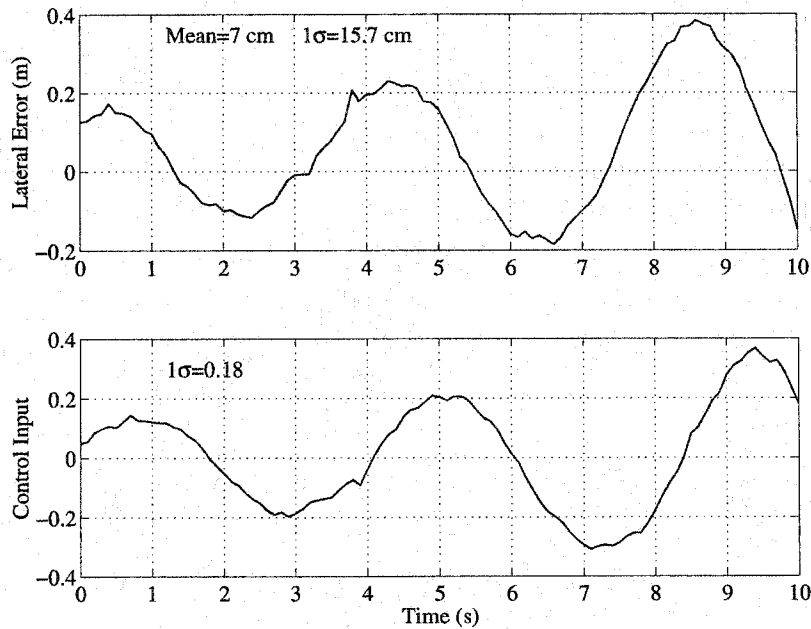


Figure 2.23 Experimental Run Using an SK Model at 5 m/s.

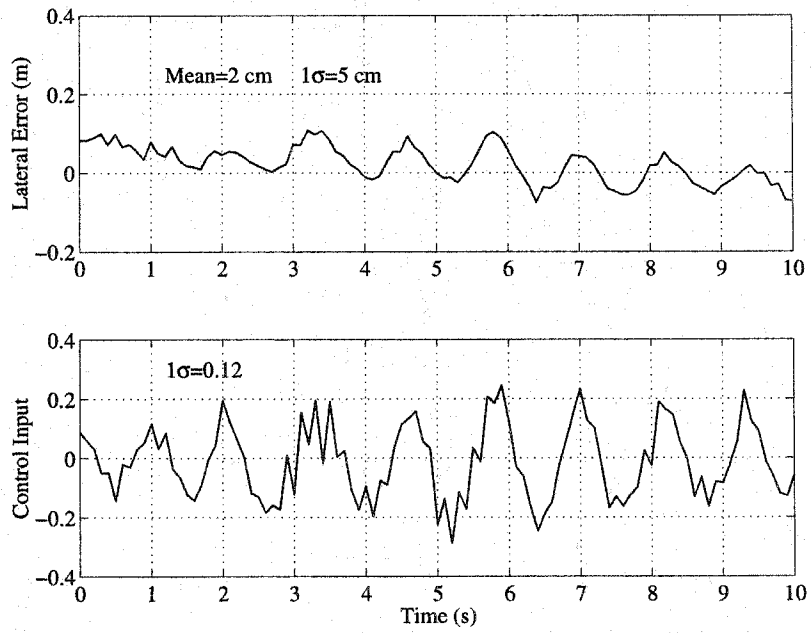


Figure 2.24 Experimental Run Using an ID1 Model at 5 m/s.

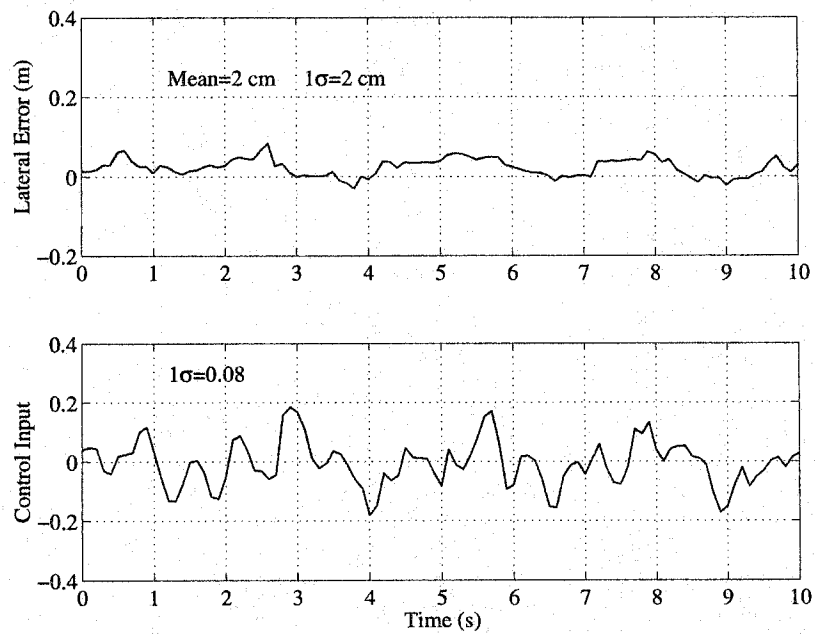


Figure 2.25 Experimental Run Using the NYD Model at 5 m/s.



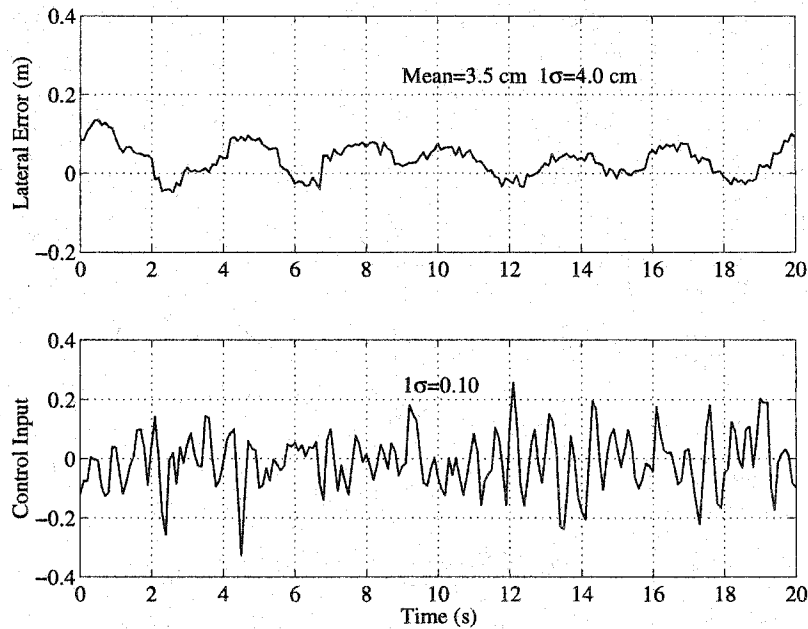


Figure 2.26 Experimental Run Using the NYD Model at 16 mph (8 m/s).

## 2.8 Conclusions

This chapter has presented a system identification of a large farm tractor for the purpose of increasing lateral control performance at higher speeds. Second order yaw dynamics (occurring at approximately 6 rad/s), as well as the dependence of these dynamics on velocity, were found using the system identification approach. The system identified (NYD) model did not resemble the characteristics of the traditional bicycle model or any other physical models proposed previously for the control of farm tractors. A physical model which considered a front tire relaxation length was shown to capture the characteristics of the NYD model. For high speed operations such as spraying, knowledge of these dynamics was shown to be important in improving the lateral control performance of the tractor.

Additionally it was shown that blindly applying LQR weights to the tractor without accounting for the yaw dynamics can produce an unstable controller. However, simpler models, such as the kinematic model, can be used for control at the expense of requiring controllers with a lower bandwidth. Therefore, simpler models, requiring a lower controller bandwidth, will have a reduced disturbance rejection capability, thereby decreasing the control accuracy of the system. A more thorough tradeoff analysis of the control accuracy versus model type for various closed-loop bandwidths should be completed. This would allow a control designer to decide whether the higher order yaw dynamic model is necessary or if a simpler model, with a lower bandwidth controller, would be sufficient for specific farm applications.

Because the physical models depend on many parameters, such as tire cornering stiffness and tire relaxation length, which are difficult to obtain, an experimental system identification approach may be the best way to obtain accurate parameters for such vehicles. A possible avenue for future work is to determine if the model parameters (including the tire relaxation length) change with field conditions, tire ballast, and weight distribution. If it is determined that any of the parameters in the FTR model do indeed vary, some type of real time system identification could be used to capture the changing dynamics. Alternatively, some type of robust control analysis may be used to provide a controller that is impervious to the changes in the yaw dynamics. However, bounds on changes in yaw dynamics must first be known, through the system identification used in this chapter. Knowledge of the yaw dynamic model discussed in this chapter will ultimately lead to an increase in performance, productivity, and robustness, in automatically steered farm vehicles.



## Chapter 3

# Control Algorithm

This chapter discusses the control architecture used for guiding the tractor along a line. The equations required for full state feedback of the tractor are first given, followed by the weighting matrix used in the LQR algorithm for designing the feedback gain. The method for utilizing the algorithm to track a straight line is presented. Simulation and experimental step response results are presented for the full state feedback of the tractor. It is shown that the linear control architecture can be used to control the tractor about a line, within 3 cm ( $1\sigma$ ), for small lateral and heading errors.

### 3.1 Lateral Dynamic Controller Model

#### 3.1.1 Hydraulic Steering Valve Model

The farm tractor is controlled through the actuation of an electro-hydraulic steering valve. The input to the steering valve is a Pulse Width Modulated (PWM) voltage signal that controls the amount of hydraulic flow to the steering valve. The valve characteristics are very nonlinear and include a dead-band region as characterized in [O'Connor, 1997] and identified on line in [Rekow, 1998]. Identification of the steady state slew rate versus input voltage was used to invert the nonlinear characteristics of the steering valve.

The remaining steering valve dynamics from the control input ( $u$ ) to steer angle are then described by the linear transfer function:

$$\delta(s) = \frac{K_v d_v}{I_v s^2 + d_v s} u(s) = \frac{K_v}{s(\tau_v s + 1)} u(s) \quad (3.1)$$

where:  $K_v$ =Valve Gain  
 $I_v$ =Valve Inertia  
 $d_v$ =Valve Damping  
 $\tau_v$ =Valve Time Constant

The above transfer function represents a first order lag between input and steering slew rate ( $\dot{\delta}$ ), plus a pure integrator from slew rate to steer angle ( $\delta$ ). The values for the steering valve model in Equation (3.1) were found using a system identification approach similar to the approach taken to model the tractor yaw dynamics in Chapter 2. Identification of the dynamics and nonlinear steady state characteristics of the valve are presented in Appendix D. The resulting parameters for the valve model, as well as physical constraints due to steer angle limits and actuator saturation, are given in Table 3.1

Table 3.1 Parameters of the Steering System.

Parameter	Value
$K_v$	1.0
$\tau_v$	0.1053 s
$\delta_{\max}$	0.8 rad
$\dot{\delta}_{\max}$	0.85 rad/s

### 3.1.2 Lateral Position Model

A state space full state feedback algorithm was used to control the lateral error ( $y_{err}$ ) of the tractor shown in Figure 3.1. The control point (CP) and Center of Gravity (CG) of the vehicle are shown in the figure.

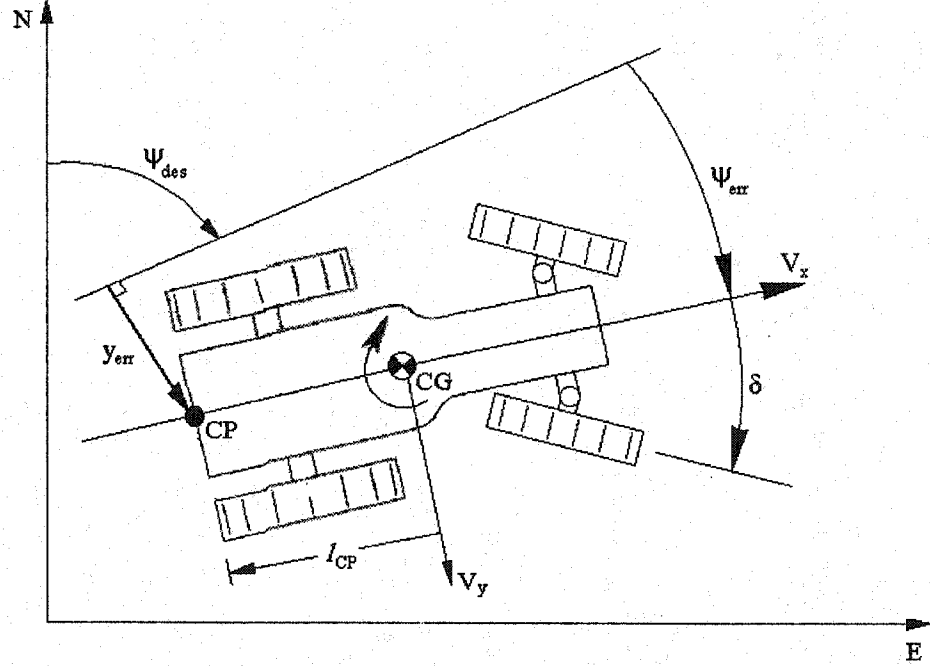


Figure 3.1 Schematic of the Lateral Dynamics for the Tractor.

The dynamics of the lateral error ( $y_{err}$ ) as shown in Figure 3.1 are described by:

$$\dot{y}_{err} = V_x \sin(\psi_{err}) + (V_y - l_{CP}\dot{\psi})\cos(\psi_{err}) \quad (3.2)$$

where:  $l_{CP}$  is the distance from the control point to the CG of the vehicle

Because  $V_x \gg V_y$ , lateral velocities at the CG ( $V_y$ ) due to vehicle sideslip are neglected. The effect of neglecting  $V_y$  will be discussed in Section 3.4. Constant or slowly varying lateral velocities will be estimated in the form of a crab angle using a Kalman filter in Chapter 4. Therefore, only the lateral velocities due to transients are neglected.

Other researchers, including [Cordesses, 1999], have used a kinematic model which assumes no lateral velocities due to sideslip. For a kinematic model of the vehicle, the point at the center of the rear axle will have no lateral velocity. Because the kinematic

model assumes no tire side-slip, the velocity vector must be along the direction of the tire. Therefore there is assumed to be no lateral velocity at the tires and thereby no lateral velocity of the vehicle between the rear tires.

It is important to note that the dynamics of the system change by moving the control point (thereby changing  $l_{cp}$ ) [Bell, 2000]. The system becomes non-minimum phase (contains a zero in the right half plane) for a control point located behind the CG (assuming the lateral velocity at the CG is zero). All of the work done in this thesis placed the control point for the tractor at the CG of the vehicle ( $l_{cp} = 0$ ). As mentioned previously, the CG for a farm tractor is highly variable, but in this thesis was assumed to be constant. Chapter 7 will discuss the direct control of a towed implement, where the control point shifts to the implement. Setting the control point at the CG, neglecting the lateral velocity at the CG, and assuming small heading errors, the lateral dynamics are described by:

$$\dot{y}_{err} = V_x \psi_{err} \quad (3.3)$$

The remaining dynamics necessary for full state feedback control are the yaw dynamics (from the new yaw dynamic (NYD) model developed in Chapter 2) and steering dynamics given in Equation (3.1). The yaw dynamics (from Equation (2.13)) defined about a reference trajectory and the steering dynamics (Equation (3.1)) are then rewritten into the following form.

$$\ddot{\psi}_{err} = -2\zeta\omega_n\dot{\psi}_{err} - \omega_n^2\psi_{err} + K_R\omega_n^2\delta \quad (3.4)$$

$$\ddot{\delta} = \frac{-1}{\tau_v}\dot{\delta} + \frac{K_v}{\tau_v}u \quad (3.5)$$

The parameters of the yaw dynamic model were given in Table 2.1 Equations (3.3-3.5) can now be placed into the state space form shown below in Equation (3.6) for the lateral control states ( $X_c$ ):

$$\dot{X}_c = A_c X_c + B_c u \quad (3.6)$$

where:

$$A_c = \begin{bmatrix} 0 & V_x & 0 & 0 & 0 & 0 \\ 0 & 0 & 1 & 0 & 0 & 0 \\ 0 & 0 & 0 & 1 & 0 & 0 \\ 0 & 0 & -\omega_n^2 & -2\zeta\omega_n & K_R\omega_n^2 & 0 \\ 0 & 0 & 0 & 0 & 0 & 1 \\ 0 & 0 & 0 & 0 & 0 & -1/\tau_v \end{bmatrix}, B_c = \begin{bmatrix} 0 \\ 0 \\ 0 \\ 0 \\ 0 \\ K_v/\tau_v \end{bmatrix}, X_c = \begin{bmatrix} y_{err} \\ \psi_{err} \\ \dot{\psi}_{err} \\ \ddot{\psi}_{err} \\ \delta \\ \dot{\delta} \end{bmatrix}$$

The poles of the sixth order system described by Equations (3.3-3.5) are shown in Figure 3.2a and the poles of the discretized system sampled at 0.1 seconds are shown in Figure 3.2b. The poles consist of three integrators (one from the steering dynamics and two from yaw rate to lateral error), two complex poles from the yaw dynamics, and one real pole from the steering dynamics.

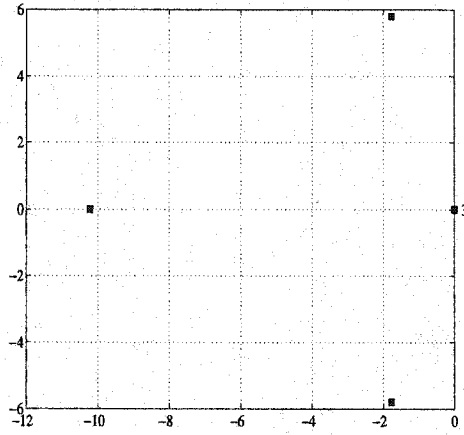


Figure 3.2a Continuous Open Loop Roots for the Lateral Tractor Model.

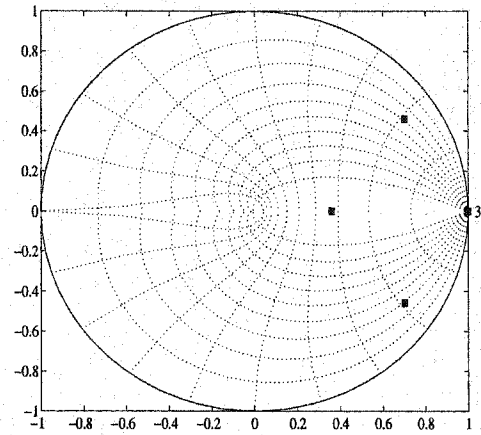


Figure 3.2b Discrete Open Loop Roots Sampled at 0.1 Seconds (10 Hz).

## 3.2 Control Law

The linear lateral dynamics can then be used to calculate the LQR control gains for the control law:

$$u = -K_c \hat{X}_c \quad (3.7)$$



where:  $\hat{X}_c = \begin{bmatrix} \hat{y}_{err} & \hat{\psi}_{err} & \hat{\psi} & \hat{\psi} & \hat{\delta} & \hat{\delta} \end{bmatrix}^T$

(Note: The ^ denotes estimates). Methods for calculating  $\hat{y}_{err}$  and  $\hat{\psi}_{err}$  from a reference are given in Section 3.3. All other estimates come from the Kalman Filter estimation method described in Chapter 4. The LQR compensator gain matrix ( $K_c$ ) was solved at each time step (by solving the Riccati equation in real time) using the following control state weighting matrix ( $Q_x$ ) and control input weighting value ( $R_u$ ) [Stengel, 1994]:

$$\begin{aligned} Q_x &= \text{diag}[Q_y \quad Q_\psi \quad Q_\psi \quad Q_\psi \quad Q_\delta \quad Q_\delta] \\ &= \text{diag}[1 \quad 0 \quad 0 \quad 0 \quad 1 \quad 0] \\ R_u &= 0.1 \end{aligned} \quad (3.8)$$

The LQR control algorithm is an “optimal” control algorithm that optimizes the cost function:

$$J_c = \sum X_c^T Q_x X_c^T + u^T R_u u \quad (3.9)$$

subject to the control feedback constraint given in Equation (3.7). It is important to note that only the relative values of the LQR weighting matrices are important. The weighting matrices can be normalized with respect to any variable or state. If they are normalized to give a cost function that is unitless, then the units of each weighting value are the reciprocal of the square of the units of the weighted state.

The selected control weighting values given in Equation (3.8) were found experimentally by “hand tuning” until satisfactory performance was obtained. The above compensator results in a closed loop bandwidth (given from the dominant eigenvalue pair of  $A_c - B_c \times K_c$ ) of about 1 Hz at 2 m/s (the bandwidth changes as a function of velocity as discussed in Chapter 2). Since we are concerned about controlling the lateral errors ( $y$ ),  $Q_y$  was set to one. Additionally,  $Q_\delta$  was set to one to penalize steer angle. Reducing the amount of steer angle adds some damping to the system. Table 3.2 lists the control gain vector for  $Q_\delta=1$  and  $Q_\delta=0$  at forward velocities of 2, 4 and 8 m/s.

Table 3.2 Control Gains for Selected Velocities.

$Q_\delta$	$V_x$ (m/s)	$K_c$
0	2	[2.75 9.03 0.97 0.23 3.95 0.23]
	5	[2.44 12.70 2.21 0.36 6.51 7.74]
	8	[2.25 16.04 3.69 0.49 7.74 0.81]
1.0	2	[2.65 9.85 1.04 0.25 4.96 0.45]
	5	[2.40 12.93 2.24 0.37 7.00 0.67]
	8	[2.22 16.13 3.72 0.50 8.06 0.83]

Figure 3.3 shows the closed loop roots of the characteristic equation (continuous and discrete) of the system for the cases of  $Q_\delta=1$  and  $Q_\delta=0$ . It is interesting to notice that only the integrator poles are altered from the open loop system to the compensated closed-loop system. The added damping using  $Q_\delta=1$  can also be seen in Figure 3.3.

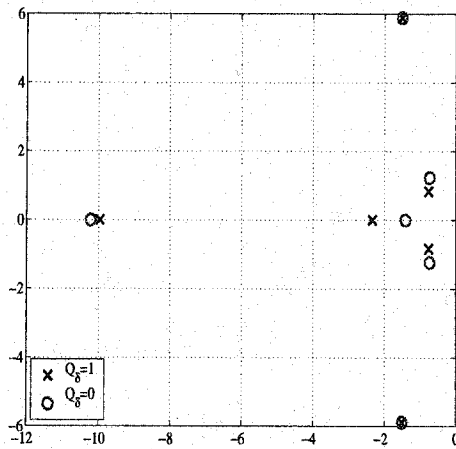


Figure 3.3a Continuous Closed-Loop Roots for the Lateral Tractor Model.

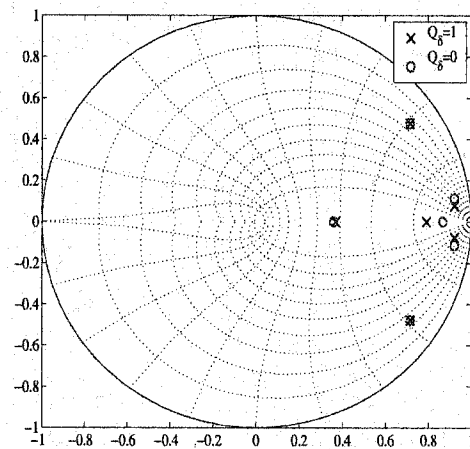


Figure 3.3b Discrete Closed-Loop Roots Sampled at 0.1 Seconds (10 Hz).

### 3.3 Simulated and Experimental Line Tracking

The majority of experiments performed in this thesis were line tracking experiments. A desired line trajectory is defined by a desired position and heading as shown in Figure 3.4.

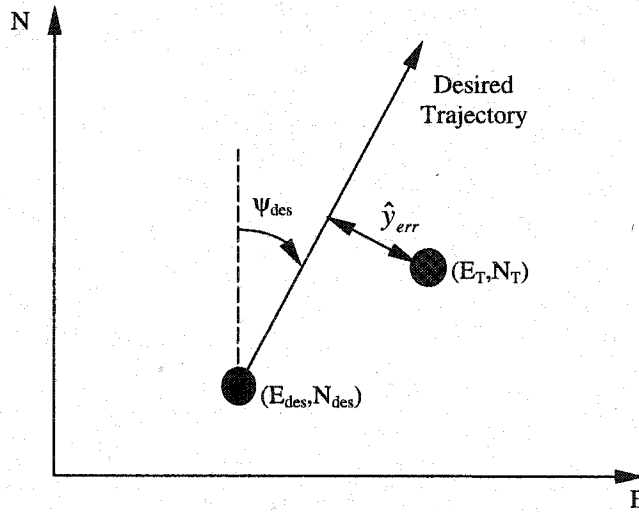


Figure 3.4 Schematic of a Desired Trajectory.

The heading error is simply the difference in the desired heading ( $\psi_{des}$ ) and the estimated heading ( $\hat{\psi}$ ).

$$\hat{\psi}_{err} = \hat{\psi} - \psi_{des} \quad (3.10)$$

The lateral error of the tractor is the distance from the control point of the tractor to the desired line and can be found by:

$$\hat{y}_{err} = (\hat{E}_T - E_{des}) \cos(\psi_{des}) - (\hat{N}_T - N_{des}) \sin(\psi_{des}) \quad (3.11)$$

The estimates for the vehicle heading and position ( $\hat{E}_T, \hat{N}_T, \hat{\psi}$ ) are from the Kalman Filter estimation algorithm discussed in Chapter 4.

Figure 3.5 shows simulated step responses at 2 m/s for one and two meter initial offsets for the cases of  $Q_{\delta}=1$  and  $Q_{\delta}=0$ . The tractor model (including the NYD model from Chapter 2, actuator saturation, steer angle limits) was simulated assuming full state feedback. The position of the tractor was simulated using the nonlinear equations:

$$\begin{aligned}\dot{E} &= V_x \sin(\psi) \\ \dot{N} &= V_x \cos(\psi)\end{aligned}\tag{3.12}$$

The increase in damping caused by setting  $Q_\delta=1$  can be seen in the step responses. Additionally, by penalizing the steer angle ( $\delta$ ), the system avoids the nonlinear saturation function of the steering actuator as well as the nonlinear position kinematics for large heading errors. However when the tractor remains in the linear region, the step response of the system using  $Q_\delta=1$  is better in terms of step response time. A more classical *nonlinear* feedback architecture (such as feedback linearization) could compensate for the nonlinear errors due to linearization and saturation when the errors from the desired trajectory are large. However, for small heading errors and steer angles (such as those encountered when tracking typical farm trajectories), the linearized LQR algorithm works quite well.

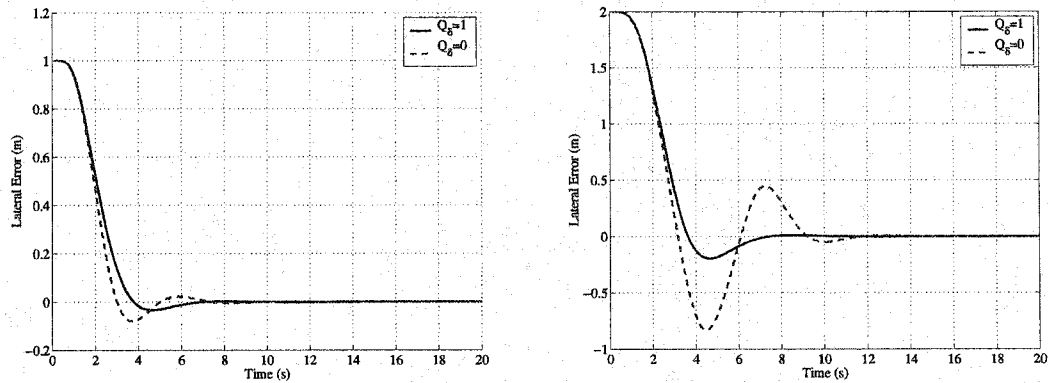


Figure 3.5a Simulated 1 m Step Response. Figure 3.5b Simulated 2 m Step Response.

Finally, Figure 3.6 shows a typical experimental step response and the tracking capabilities of the real system at 2 m/s using the LQR weighting matrices given in Equation (3.8). The cascaded Kalman filter given in Chapter 4 was used in conjunction with the LQR full state feedback because measurements of all the states are not available in the experimental system. The simulated step response of the tractor, assuming full state feedback, is also shown in the figure. It has been shown that the tractor can be controlled along various other trajectories such as arcs, curves, and spirals. Methods for control along these other trajectories can be found in [Bell, 1999].

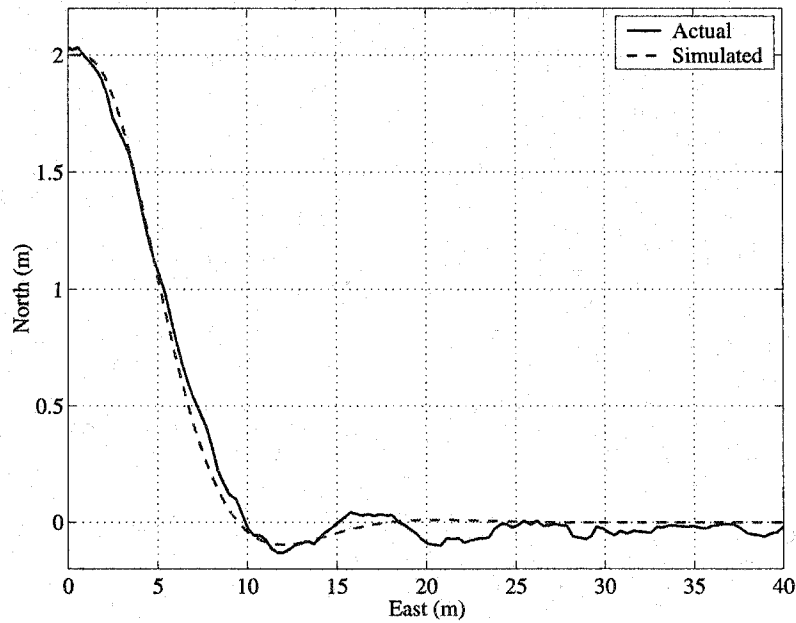


Figure 3.6 Experimental vs. Simulated Step Response.

### 3.4 Effect of Neglecting Sideslip

As discussed in Section 3.2, lateral velocities at the CG due to vehicle yaw dynamic transients are neglected (partly due to historical reasons [O'Conner, 1997; Bell, 1999; Rekow, 2000]). This section is an attempt to look at the effect of assuming that these velocities are negligible. An analytical (the FTR) model that includes the lateral velocity at the CG was developed in Chapter 2. This model could be used for control. However, in practice this would require the estimation of an additional unmeasured state. Future work should conduct a more thorough investigation of neglecting the lateral velocity and weigh the tradeoffs of a more complicated estimator (increasing the order of the estimator by one).

The FTR model developed in Chapter 2 is given again below.

$$\begin{bmatrix} \dot{V}_y \\ \dot{\psi} \\ \dot{\alpha}_f \end{bmatrix} = \begin{bmatrix} \frac{c_{\alpha}}{mV_x} & -V_x + \frac{c_{\alpha}b}{mV_x} & \frac{-c_{\alpha}}{m} \\ \frac{c_{\alpha}b}{I_zV_x} & \frac{-c_{\alpha}b^2}{I_zV_x} & \frac{-c_{\alpha}a}{I_z} \\ 1/\sigma_f & a/\sigma_f & -V_x/\sigma_f \end{bmatrix} \begin{bmatrix} V_y \\ \psi \\ \alpha_f \end{bmatrix} + \begin{bmatrix} 0 \\ 0 \\ -V_x/\sigma_f \end{bmatrix} \delta \quad (3.13)$$

The parameters of the FTR model are given in Table 2.2. The lateral dynamics (including the lateral velocity at the CG) for small heading errors are now defined as:

$$\dot{y}_{err} = V_x \psi_{err} + V_y \quad (3.14)$$

Equations (3.13-3.14) and (3.5) can be placed into the state space form shown in Equation (3.6) where the state vector is now defined as.

$$x_c = \begin{bmatrix} \hat{y} & \hat{\psi} & \hat{\psi} & V_y & \alpha_f & \hat{\delta} & \hat{\delta} \end{bmatrix}^T$$

The linear lateral dynamics using the FTR model can then be used to calculate the LQR control gains for the control law given in Equation (3.7). Again the compensator gain matrix ( $K_c$ ) is solved using the LQR algorithm. The same control input weighting value ( $R_u$ ) and the control state weighting matrix ( $Q_x$ ) given in Equation (3.8) are used. However, the FTR model requires the following two additional state weighting parameters to solve for the LQR control gain:

$$Q_{\alpha_f} = Q_{V_y} = 0 \quad (3.15)$$

The FTR tractor model with the steering actuator model in Equation (3.1) (including actuator saturation, steer angle limits) was simulated assuming full state feedback. The position of the tractor was simulated using the following nonlinear equations, which include the lateral velocity at the CG:

$$\begin{aligned} \dot{E} &= V_x \sin(\psi) + V_y \cos(\psi) \\ \dot{N} &= V_x \cos(\psi) - V_y \sin(\psi) \end{aligned} \quad (3.16)$$

Figure 3.7 shows simulated one meter step responses at 5 m/s for the controllers using the FTR and NYD models. The control algorithm using the NYD model (presented in Section 3.3) neglects the lateral velocity at the CG while the control algorithm using the FTR model (presented in this section) includes the lateral velocity. Note that both control algorithms were simulated on the system using the FTR model and included the lateral

velocity. In the simulated response, neglecting  $V_y$  causes the simulated response of the NYD controller to be more damped and does not produce the “optimal” (optimal in terms of an LQR controller design) step response as does the FTR controller. However experimental step responses (which neglected the lateral velocities) were not seen to be over damped, but rather did produce typical LQR design step responses.

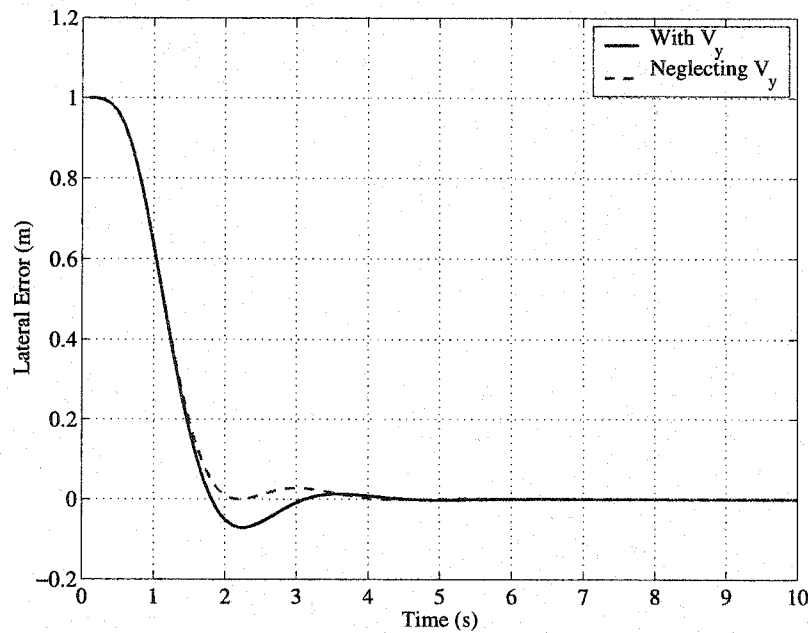


Figure 3.7 Comparison of Control Algorithms on the FTR Model for a Simulated 1 m Step Response at 5 m/s.

Figure 3.8 shows the lateral velocities ( $V_x\psi$  and  $V_y$ ) as well as the integrated lateral position ( $y$ ) from each of these lateral velocities for the above simulated step response. As seen in the figure, the  $V_x\psi$  term dominates as was assumed in simplifying Equation (3.2) to form Equation (3.3).

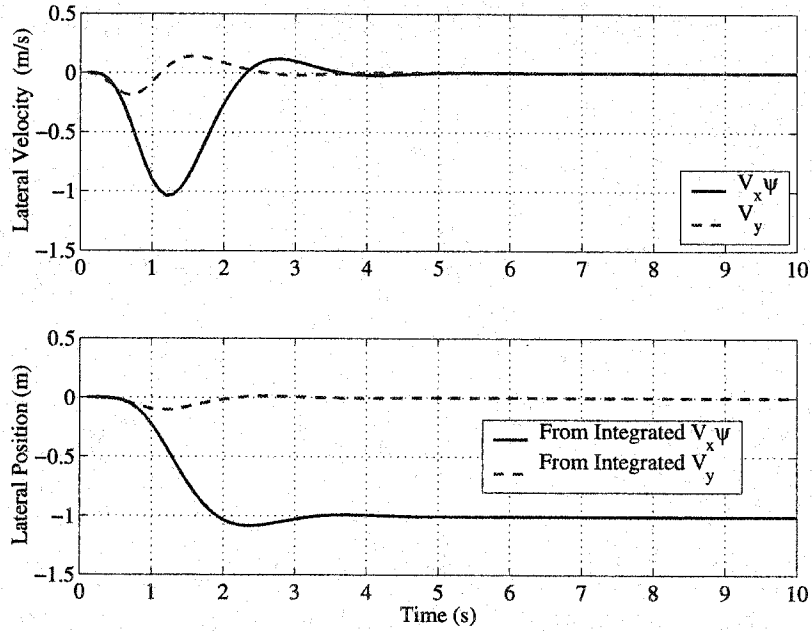


Figure 3.8 Comparison of the Significance of the Two Different Lateral Velocity Components for a Simulated 1 m Step Response at 5 m/s.

The fact that experimental step responses using the NYD controller were not over damped as seen in the simulations may be due to mis-modeling of the CG location. The CG location of the tractor can vary depending on things such as tire and nose ballast. Nose ballast is changed depending on the farm application to compensate for towing heavy loads. For the work in this thesis the front of the tractor was ballasted with twenty 100 pound lead weights. This may have caused the actual CG location to shift forward from the modeled CG location. Mis-modeling the CG location of the vehicle can have the same effect on the control of the tractor as neglecting the lateral velocity (or adding a fictitious lateral velocity). This is because positive tractor yaw rates will add lateral velocity in front of the CG and deduct lateral velocity behind the CG. This effect can be seen in the  $l_{CP}\dot{\psi}$  term in Equation (3.2). Therefore the vehicle will experience a greater or lesser lateral velocity at the modeled CG location than at the actual CG location. Figure 3.9 shows the step response of the NYD controller (which neglects the lateral velocity at the CG) for various mis-modeled CG locations. Notice that the NYD



controller with a CG location modeled 0.5 m behind the actual CG location produces the same step response as the FTR controller which includes the lateral velocities at the CG.

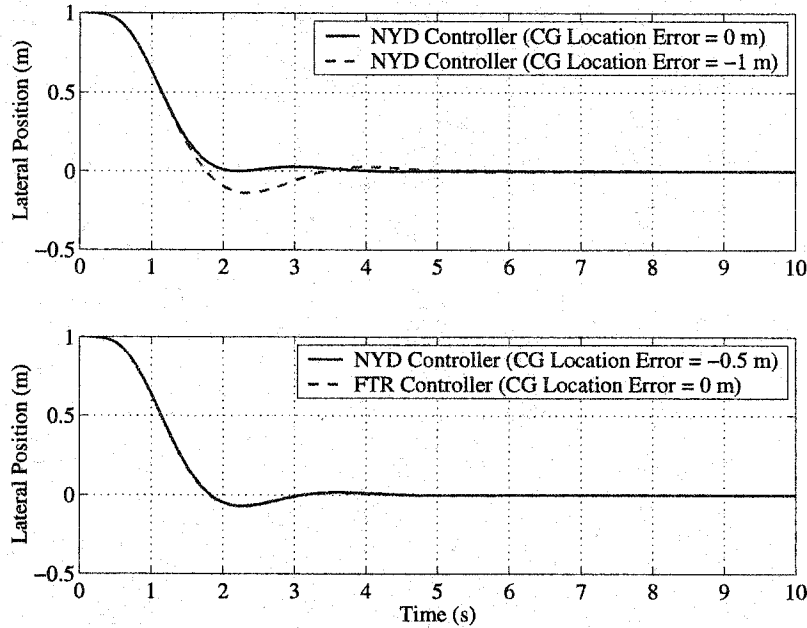


Figure 3.9 Comparison of Step Responses at 5 m/s Using the NYD Controller with Mis-Modeled CG Locations. A Negative CG Location Error Corresponds to Modeling the CG Behind the Actual CG Location.

### 3.5 Conclusions

This chapter has described the use of a full state feedback algorithm for regulating the tractor about a line trajectory. The lateral dynamics of the tractor, which include the second order yaw dynamics from Chapter 2, and the dynamics of the steering valve, were used for the full state model. An LQR algorithm was used to select the feedback gains of the system. The open and closed-loop roots for the tractor were shown as well as simulated and experimental step responses for the control algorithm. The model and algorithm were shown to be effective in tracking straight line trajectories. The effect of neglecting lateral velocities as well as mis-modeling the tractor's CG location were also discussed.

## Chapter 4

# Cascaded State Estimation

The full state feedback algorithm utilized in Chapter 3 requires the estimation of several states because direct measurements of these states are not available. Additionally, states must continue to be estimated if GPS measurements become unavailable (due to some type of temporary GPS outage or communication loss with the references station). Integration of GPS with a low cost Inertial Navigation System (INS) can help to provide continuous control of a tractor on a farm through these short outages. The cm-level accuracy of carrier-phase Differential GPS allows for precise calibration of the sensor models in order to improve the accuracy of the dead reckoning system. This includes accurately estimating the gyroscope and radar biases which requires the addition of two more states to the tractor estimator. Two additional measurements are added to the estimator for these sensors (the radar velocity and the gyroscope yaw rate). Once the estimator is modified to incorporate these velocity and yaw rate measurements, and their corresponding biases, the state estimates can be used to control the position of the tractor. The control algorithm presented in Chapter 3 is independent of the estimation algorithm, which allows for optimization of the GPS/INS integration and dead reckoning estimator, without affecting the control algorithm for the tractor.

This chapter develops a cascaded estimation algorithm for estimating all of the biases and model states for full state feedback and dead reckoning of the farm tractor through

short GPS outages. First a conventional (one stage) estimation scheme is presented. This type of estimation scheme has several drawbacks including sensitivity to model errors for bias estimation and dead-reckoning as well as increased computational requirements due to the size of the matrices involved. Additionally, the states for position and velocity are not highly coupled to the tractor dynamic states, allowing for separation of the estimators. For these reasons, the state estimation is divided into two cascaded estimators. The first is a dead reckoning (or navigation) estimator which calibrates all of the inertial sensor biases while GPS is available. The dead reckoning estimator continues to provide position and heading estimates during periods without GPS measurement by specifically integrating inertial measurements when GPS measurements are not available. This provides the ability to maintain continuous control of the vehicle through these GPS outages. The second estimator is used to estimate the additional states needed for the full state feedback algorithm discussed in Chapter 3. Bias estimates from the dead reckoning estimator are used to correct the sensor measurement used in the second estimator. An Extended Kalman Filter (EKF) is then used to update each of the estimators (either simultaneously or at independent update rates). Results are given showing that the cascaded estimation technique provides better estimation of the vehicle states, especially during a GPS outage, over a conventional estimation scheme. Results are also given which verify the ability of the estimation algorithm to estimate all of the system biases and provide heading estimation through a 30 second GPS outage.

## 4.1 Tractor Dynamics and Estimated States

The schematic of the farm tractor in general East-North coordinates is shown in Figure 4.1. The position of the tractor, at any point along the centerline of the tractor can be described by:

$$\begin{aligned}\dot{E}_T &= V_x \sin(\psi) + (V_y - \dot{\psi}l_{CP})\cos(\psi) \\ \dot{N}_T &= V_x \cos(\psi) - (V_y - \dot{\psi}l_{CP})\sin(\psi)\end{aligned}\tag{4.1}$$

where  $l_{CP}$  is the distance from the point along the centerline of the vehicle to the CG.

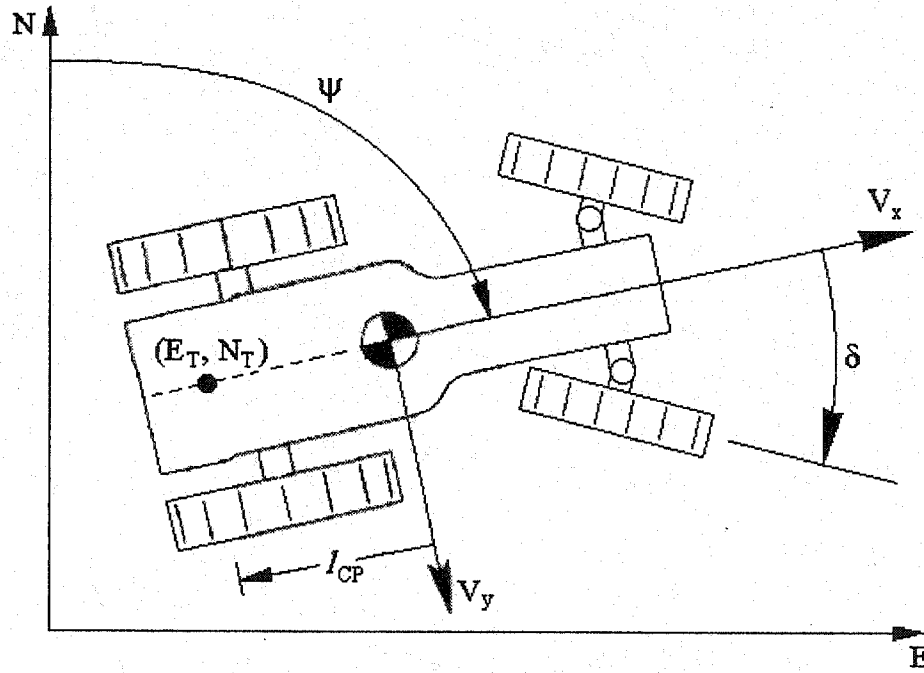


Figure 4.1 Schematic of a Farm Tractor.

Again, as discussed in Chapter 3, the lateral velocities at the CG due to transients are neglected ( $V_y = 0$ ) and  $l_{cp}$  is set to zero in the work in this thesis. However, slowly varying lateral velocities due to vehicle “crabbing” will be estimated in the form of a heading bias. In this thesis, crab angle refers to the constant (or slowly varying) difference between the vehicle’s heading and direction of travel (known as vehicle sideslip). Vehicles experience lateral velocities or sideslip due to yaw transients. However, crab angles can occur from traveling on sloped terrain, tires getting caught in a furrow, or pulling a heavy implement. Additionally, an apparent crab angle can occur from misalignment of the heading sensor. Therefore, these slowly varying lateral velocities are treated as a bias. Note that GPS measurements obtained on the roof of the tractor must be translated through a “lever arm” to the CP [Bell, 1999]. This requires full attitude (roll, pitch, and yaw) of the tractor (as shown in Equation (6.20-6.21)).

The tractor yaw dynamics (given previously in Equation (3.4)) are described by:

$$\ddot{\psi} = -2\zeta\omega_n\dot{\psi} - \omega_n^2\psi + K_R\omega_n^2\delta \quad (4.2)$$

The values for  $K_R$ ,  $\omega_n$ , and  $\zeta$  are functions of velocity and determined from a least squares best fit of the system identification data in Chapter 2. The steering valve dynamics from the control input ( $u$ ) to steer angle are described by:

$$\ddot{\delta} = \frac{-1}{\tau_v} \dot{\delta} + \frac{K_v}{\tau_v} u \quad (4.3)$$

where the control input ( $u$ ) is a pulse width modulated (PWM) voltage to an electro-hydraulic valve used to steer the front wheels. The values for  $K_v$ ,  $d_v$ , and  $I_v$  that describe the steering dynamics were determined using system identification techniques similar to the techniques used to obtain the yaw dynamic model in Chapter 2.

The model dynamics in Equations (4.1-4.3) are of the form:

$$\dot{X} = f(X) + Bu \quad (4.4)$$

In order to utilize linear state space control and estimation techniques [Franklin, 1998], Equations (4.1-4.3) must be placed in the form:

$$\begin{aligned} \dot{X} &= AX + Bu \\ Y &= CX \end{aligned} \quad (4.5)$$

## 4.2 Regular Estimation

The control input is a PWM signal to a hydraulic valve that controls the slew rate of the steer tires. The seventh order model shown above in Equations (4.1-4.3) must be augmented with five additional states (four biases, and velocity) resulting in a twelfth order estimator. Six of the states, given in Equation (3.6), are needed for the full state feedback algorithm discussed in Chapter 3. The remaining states are needed to estimate biases, positions, and velocity in order to improve the accuracy of the control architecture. The estimated states are (denoted by a  $\hat{\cdot}$ ):

$$\hat{X} = \left[ \hat{E}_T \quad \hat{N}_T \quad \hat{r}_b \quad \hat{\psi} \quad \hat{g}_b \quad \hat{\psi}_b \quad \hat{\psi} \quad \hat{\psi} \quad \hat{V}_x \quad \hat{\delta} \quad \hat{\delta} \quad \hat{\delta}_b \right]^T$$

where:

$E_T$  = tractor east position  
 $N_T$  = tractor north position  
 $V_x$  = forward velocity  
 $\psi$  = heading  
 $\dot{\psi}$  = yaw rate  
 $\ddot{\psi}$  = yaw acceleration  
 $\psi_b$  = heading bias or "crab angle"  
 $\delta$  = steer angle  
 $\dot{\delta}$  = steering slew rate  
 $\delta_b$  = steer angle bias  
 $g_b$  = gyro bias  
 $r_b$  = radar bias

Because the dynamics described in Equations (4.1-4.3) are nonlinear, they must be linearized about an operating point at each time step in order to place the dynamics in the form shown in Equation (4.5). This is done by solving for the Jacobian (J) at each time step such that:

$$\dot{X} = JX + Bu + w \quad (4.6)$$

where:

$$J = \begin{bmatrix} \frac{\partial f_1}{\partial x_1} & \dots & \frac{\partial f_1}{\partial x_n} \\ \vdots & & \vdots \\ \frac{\partial f_n}{\partial x_1} & \dots & \frac{\partial f_n}{\partial x_n} \end{bmatrix}_{X=X_0}$$

$w$  = zero mean random process noise vector with covariance,  $Q_w$

The biases and velocity of the tractor are assumed to be constant. However, they are modeled as a first order Markov process such that:

$$\begin{bmatrix} \dot{V}_x & \dot{\psi}_b & \dot{g}_b & \dot{r}_b & \dot{\delta}_b \end{bmatrix}^T = w_{bias}$$

where  $w_{bias}$  is a zero mean random process (white) noise vector.

Modeling the biases in this way prevents the estimation of these states from “falling asleep” by providing persistent excitation to the Kalman filter as seen in Equations (4.10-4.11). The estimated process noise values used in this thesis are shown in Table 4.1. Many of these estimates were selected by previous researchers to provide adequate filtering performance [O’Connor, 1997; Bell, 1999; Rekow, 2001]. The process noise

used for the bias states were “tuned” to provide the estimator with an observed adequate tracking to filtering characteristics.

Table 4.1 Assumed Process Noise Covariance for Each State.

State	Covariance	State	Covariance ( $\sigma^2$ )
$E$	$0.1 \text{ m}^2$	$\delta$	$0.0 (\text{rad/s})^2$
$N$	$0.1 \text{ m}^2$	$V_x$	$0.01 (\text{m/s})^2$
$\psi$	$0.01 \text{ rad}^2$	$\delta_b$	$1.0 \times 10^{-6} \text{ rad}^2$
$\dot{\psi}$	$0.1 (\text{rad/s})^2$	$g_b$	$1.0 \times 10^{-5} (\text{rad/s})^2$
$\ddot{\psi}$	$0.1 (\text{rad/s}^2)^2$	$r_b$	$1.0 \times 10^{-6} (\text{m/s})^2$
$\delta$	$0.01 \text{ rad}^2$	$\psi_b$	$1.0 \times 10^{-4} \text{ rad}^2$

The observation matrix ( $C$ ) is described by:

$$Y_{meas} = CX + v \quad (4.7)$$

where:  $Y_{meas} = [E_T^{GPS} \quad N_T^{GPS} \quad \psi^{GPS} \quad \dot{\psi}^{gyro} \quad V_x^{radar} \quad \delta^{pot}]^T$   
 $v$  = unknown sensor noise vector (6x1) with covariance,  $R_v$

The sensor noise values were obtained by taking the covariance of static sensor data. The sensor noise values used in this thesis are give in Table 4.2.

Table 4.2 Assumed Sensor Noise Covariances.

Measured State	Sensor	Covariance ( $\sigma^2$ )
$E$	GPS	$9.0 \times 10^{-4} \text{ m}$
$N$	GPS	$9.0 \times 10^{-4} \text{ m}$
$\psi$	GPS	$1.745 \times 10^{-3} \text{ rad}$
$\dot{\psi}$	FOG	$6.0 \times 10^{-5} \text{ rad/s}$
$\delta$	Linear Potentiometer	$1.5 \times 10^{-3} \text{ rad}$
$V_x$	Radar	$1.4 \times 10^{-2} \text{ m/s}$

Note that there are four sensor biases (used to define the observation matrix) such that:

$$\begin{aligned}
 \psi^{GPS} &= \psi + \psi_b \\
 \delta^{pot} &= \delta + \delta_b \\
 V_x^{radar} &= V_x + r_b \\
 \dot{\psi}^{gyro} &= \dot{\psi} + g_b
 \end{aligned} \tag{4.8}$$

The resulting linearized state matrices (linearized about a desired heading,  $\psi_{des}$ ) are shown below along with the state divisions that will be made in the cascaded estimation scheme in the preceding section.

$$\dot{X} = \begin{bmatrix} 0 & 0 & 0 & V_x \cos(\psi_{des}) & 0 & 0 & 0 & 0 & \sin(\psi_{des}) & 0 & 0 & 0 \\ 0 & 0 & 0 & -V_x \sin(\psi_{des}) & 0 & 0 & 0 & 0 & \cos(\psi_{des}) & 0 & 0 & 0 \\ 0 & 0 & 0 & 0 & 0 & 0 & 0 & 0 & 0 & 0 & 0 & 0 \\ 0 & 0 & 0 & 0 & 0 & 0 & 1 & 0 & 0 & 0 & 0 & 0 \\ 0 & 0 & 0 & 0 & 0 & 0 & 0 & 0 & 0 & 0 & 0 & 0 \\ 0 & 0 & 0 & 0 & 0 & 0 & 0 & 0 & 0 & 0 & 0 & 0 \\ \hline 0 & 0 & 0 & 0 & 0 & 0 & 0 & 1 & 0 & 0 & 0 & 0 \\ 0 & 0 & 0 & 0 & 0 & 0 & -\omega_n^2 & -2\zeta\omega_n & 0 & K_R\omega_n & 0 & 0 \\ 0 & 0 & 0 & 0 & 0 & 0 & 0 & 0 & 0 & 0 & 0 & 0 \\ 0 & 0 & 0 & 0 & 0 & 0 & 0 & 0 & 0 & 0 & 1 & 0 \\ 0 & 0 & 0 & 0 & 0 & 0 & 0 & 0 & 0 & 0 & -1/\tau_v & 0 \\ 0 & 0 & 0 & 0 & 0 & 0 & 0 & 0 & 0 & 0 & 0 & 0 \end{bmatrix} \begin{bmatrix} E_T \\ N_T \\ r_b \\ \psi \\ g_b \\ \psi_b \\ \dot{\psi} \\ \ddot{\psi} \\ V_x \\ \delta \\ \dot{\delta} \\ \delta_b \end{bmatrix} + \begin{bmatrix} 0 \\ 0 \\ 0 \\ 0 \\ 0 \\ 0 \\ 0 \\ 0 \\ 0 \\ 0 \\ -K_v/\tau_v \\ 0 \end{bmatrix} u + w \tag{4.9}$$

$$Y_{meas} = \begin{bmatrix} 1 & 0 & 0 & 0 & 0 & 0 & 0 & 0 & 0 & 0 & 0 & 0 \\ 0 & 1 & 0 & 0 & 0 & 0 & 0 & 0 & 0 & 0 & 0 & 0 \\ 0 & 0 & 0 & 1 & 0 & 1 & 0 & 0 & 0 & 0 & 0 & 0 \\ \hline 0 & 0 & 0 & 0 & 0 & 1 & 0 & 1 & 0 & 0 & 0 & 0 \\ 0 & 0 & 1 & 0 & 0 & 0 & 0 & 0 & 0 & 1 & 0 & 0 \\ 0 & 0 & 0 & 0 & 0 & 0 & 0 & 0 & 0 & 0 & 1 & 1 \end{bmatrix} X + v$$

The Extended Kalman Filter (EKF) is comprised of a measurement update and time update [Stengel, 1994], which is performed at each time step ( $k$ ). The measurement update is described by:

$$\begin{aligned}
 L_k &= P_k C^T (C P_k C^T + R_v)^{-1} \\
 X_k &= X_k + L_k (y_{meas} - C X_k) \\
 P_k &= (I - L_k C) P_k
 \end{aligned} \tag{4.10}$$

where:  $L$  = Kalman Gain Vector



$P$  = State Estimation Covariance Matrix  
 $C$  = Observation Matrix  
 $R_v$  = Sensor Noise Matrix  
 $I$  = Identity Matrix  
 $X$  = State Estimate Vector

A simple Euler Integration time update is described by:

$$\begin{aligned}
 X_{k+1} &= X_k + \Delta t \dot{X}_{k+1} \\
 P_{k+1} &= \Phi P_k \Phi^T + Q_w
 \end{aligned}
 \tag{4.11}$$

where:  $\Phi$  = discretized Jacobian (J) at each time step  
 $Q_w$  = discretized process noise matrix  
 $\dot{X}$  is calculated from nonlinear Equations (4.1-4.3)

The process noise matrix ( $Q_w$ ) was taken to be a diagonal matrix, which assumes no correlation for the process noise of any of the states. Although the process noise of some states are correlated in reality, this approximation provides good filtering characteristics by the Kalman filter. The values of each diagonal were the process noise covariance of the corresponding state as listed in Table 4.1. Similarly the sensor noise matrix ( $R_v$ ) was taken to be diagonal using the sensor noise values in Table 4.2.

The addition of the radar and gyroscope biases is used to improve the accuracy of the dead-reckoning system. Integration of unknown biases results in a parabolic growth of positioning errors. The radar bias comes from the fact that the radar sensor has a bias offset which is dependent on ground conditions. The heading bias is used to solve for any bias in the heading sensor or vehicle heading (known as a “crab angle” or sideslip) that can occur from pulling heavy equipment or tillage on sloped terrain. On sloped terrain, the crab angle reverses sign as the roll angle due to slope changes sign (which occurs when the tractor reverses direction in the field) [Bell, 1999]. Estimation of the crab angle is necessary to provide information about the difference between the vehicle heading and direction of travel. Estimation of the steer angle bias is used to improve the control performance. State estimation of the forward velocity is required for use in the model as seen in Equation (4.1) and because parameters in Equation (4.2) are a function of velocity. All of the biases and velocity are assumed to be slowly varying.

### 4.2.1 Shortcomings of the Regular Estimation Algorithm

This section presents a few of the problems associated with the regular estimation algorithm presented in Section 4.2.1. These shortcomings will lead to the motivation behind the development of the cascaded estimation architecture described in the next section.

The tractor is equipped with differential braking which gives the ability to add a heading disturbance to the system by braking one side of the tractor. In the following experiment, the bias estimator is allowed to remain on even after GPS measurements are no longer available. Figure 4.2 shows that the bias estimator will still try to estimate the bias without GPS as mentioned in the previous section. This is because in theory the gyroscope bias is still observable without GPS measurements through the steering angle. However, uncertainties in the model as well as unknown disturbances on the tractor will create large errors in the bias estimation when GPS attitude measurements are not available (as seen in Figure 4.2). Because the steering wheels remain straight (which, according to the model, should result in no yawing of the tractor) the estimator believes that the yaw rate, resulting from the brake disturbance acting on the tractor, is a change in the gyroscope bias and not an actual yaw rate.

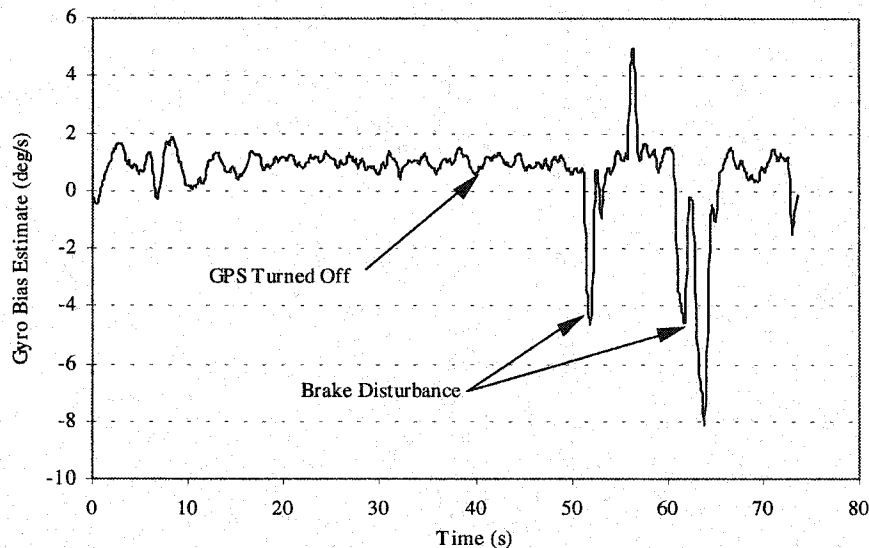


Figure 4.2 Gyroscope Bias Estimation from the Regular Estimation Scheme. Brake Disturbances are Added After a Simulated GPS Outage.

Figure 4.3 shows another run where a brake disturbance is being added to affect the tractor heading once GPS has been removed. Even though the tractor heading has changed, the estimated heading remains constant. This is due to the fact that the EKF integrates the heading from the model through the wheel angle as described by Equation (4.2) (which remains constant) instead of from the yaw gyroscope because the sensor noise is less on the steer angle sensor.

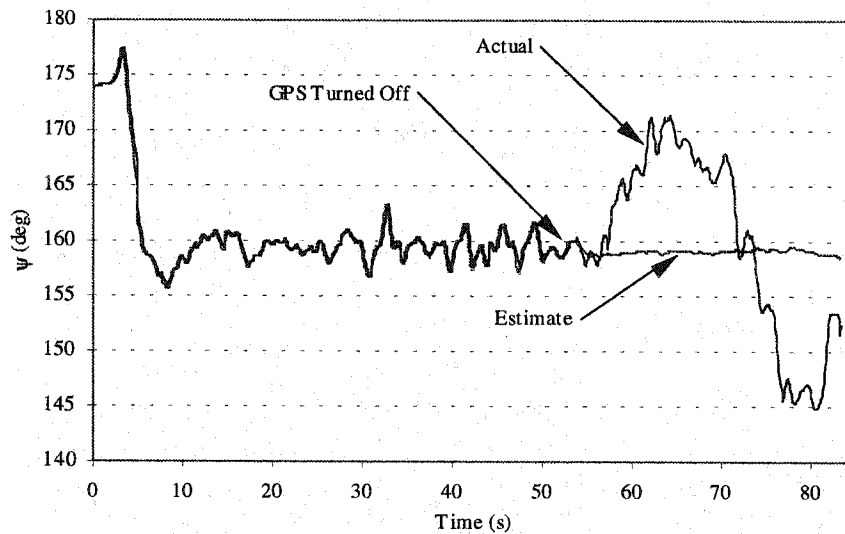


Figure 4.3 Actual vs. Estimated Heading with the Regular EKF Estimation Scheme. Brake Disturbances are Added After a Simulated GPS Outage.

Finally, Figure 4.4 shows the gyroscope bias estimate without estimating the steer angle bias. Because a steer angle bias results in a constant yaw rate, as seen from Equation (4.2), a bias in the steering angle is also seen as a constant yaw rate offset by the model. Similarly, any other model errors in the system can lead to incorrect estimates of the sensor biases. The regular Kalman filter can be used to try and estimate both the steer angle and gyroscope biases. However, the Kalman filter can struggle to correctly estimate both biases together and can even become unstable trying to estimate both biases if correct disturbance covariances ( $Q_w$ ) are not used. Any unknown bias in the steer angle sensor or effective steer angle will result in an error in the yaw rate estimate, which will in turn lead to an error in the gyroscope bias estimate. It is more desirable to estimate the

sensor biases with respect to the reference measurements (GPS in the case of this work) as opposed to a reference provided by the model to ensure the most accurate estimates of the biases. For these reasons, it is necessary to utilize two separate cascaded estimators in order to accurately estimate all of the states.

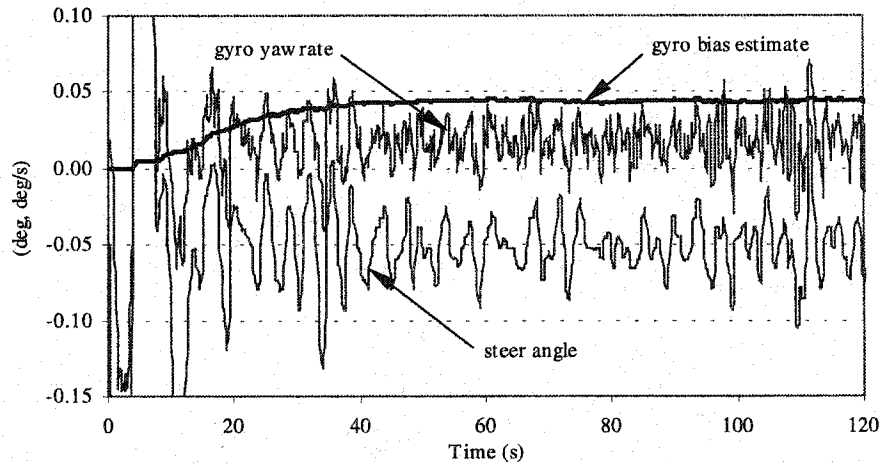


Figure 4.4 Estimation of the Gyroscope Bias with No Estimate of the Steer Angle Bias During a Straight Line Tracking Experiment. Average Yaw Rate and Steer Angle Should Equal Zero. Therefore the Sensor's Bias is Equal to the Sensor's Average Value for the Straight Line Tracking Experiment.

### 4.3 Cascaded Estimation Algorithm

Separating the estimation into two filters allows for estimation of all of the states in order to improve both the dead reckoning system as well as the control system. Figure 4.5 shows a block diagram demonstrating the almost “natural” separation of the filters. This natural separation could also be observed by the number of zero elements in the state matrices, and almost complete independence of the two sets of states in Equation (4.12). The first filter provides accurate positioning with dead reckoning estimation when no GPS measurements are available, by estimating biases in the IMU while GPS is available. The second filter uses the corrected IMU plus the steer angle measurements to provide the additional states for control of the tractor. Furthermore, the use of a separate

estimation technique allows for estimation of both the steer angle and gyroscope biases. As mentioned previously, these two biases cannot be estimated together in the Kalman filter. Separating the estimators also allows for the two filters to be run at different speeds. As will be seen in the following chapter, the accuracy of the time update depends largely on the sample rate. Because the yaw rate and velocity measurements (from the gyroscope and on-board radar, respectively) are continuously available, they can be sampled and integrated forward at higher sample rates in order to increase the dead reckoning accuracy.

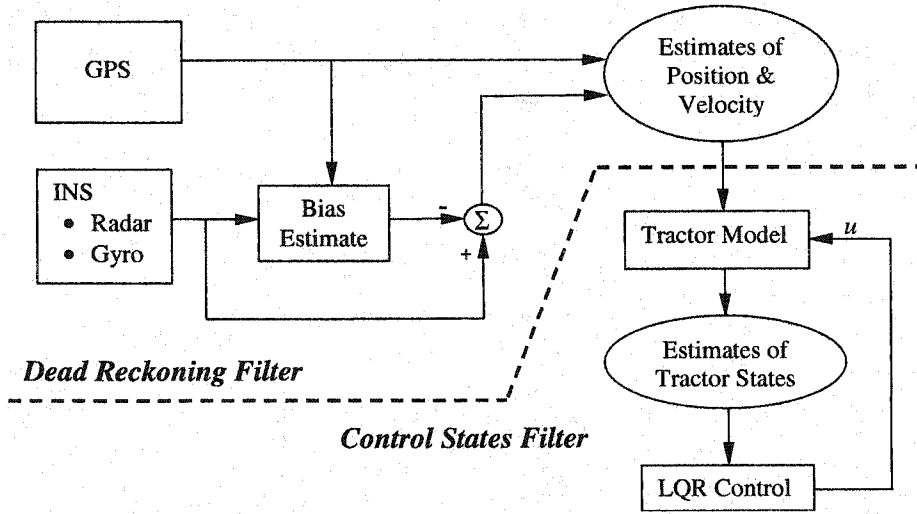


Figure 4.5 Block Diagram of the Cascaded Estimation Architecture.

Substituting the available rate measurements (used as inputs) into Equations (4.1) and (4.2) (with  $l_{CP}=0$ ) results in the dead reckoning (or kinematic) equations:

$$\begin{aligned}\dot{E}_T &= (V_x^{radar} - r_b) \sin(\psi) \\ \dot{N}_T &= (V_x^{radar} - r_b) \cos(\psi) \\ \dot{\psi} &= \dot{\psi}^{gyro} - g_b\end{aligned}\tag{4.12}$$

where  $V_x^{radar}$  and  $\dot{\psi}^{gyro}$  are the radar and yaw gyroscope measurements. The dead reckoning estimated states are:

$$x_1 = [E_T \quad N_T \quad r_b \quad \psi \quad g_b \quad \dot{\psi}_b]^T$$

The remaining dynamics used to estimate the states necessary for control are the tractor yaw dynamics (4.3), the steering dynamics (4.4), and velocity. The control estimated states are:

$$X_2 = [\psi \quad \dot{\psi} \quad v_X \quad \delta \quad \dot{\delta} \quad \delta_b]^T$$

The dynamics in Equation (4.12) can be linearized about the operating point at each time step by solving for the Jacobian ( $J$ ) such that:

$$\dot{X}_1 = J_1 X + B_1 u + w_1 \quad (4.13)$$

where:

$$J_1 = \begin{bmatrix} \frac{\partial f_1}{\partial x_1} & \dots & \frac{\partial f_1}{\partial x_n} \\ \vdots & & \vdots \\ \frac{\partial f_n}{\partial x_1} & \dots & \frac{\partial f_n}{\partial x_n} \end{bmatrix}$$

As with the regular estimation scheme, the biases and velocity are modeled as a first order Markov process. Equations (4.12) linearized about a desired heading ( $\psi_{des}$ ) and placed in the form shown in Equation (4.13) are:

$$\dot{X}_1 = \begin{bmatrix} 0 & 0 & -\sin(\psi_{des}) & r_b \cos(\psi_{des}) & 0 & 0 \\ 0 & 0 & -\cos(\psi_{des}) & -r_b \sin(\psi_{des}) & 0 & 0 \\ 0 & 0 & 0 & 0 & 0 & 0 \\ 0 & 0 & 0 & 0 & -1 & 0 \\ 0 & 0 & 0 & 0 & 0 & 0 \\ 0 & 0 & 0 & 0 & 0 & 0 \end{bmatrix} \begin{bmatrix} e \\ n \\ r_b \\ \psi \\ g_b \\ \psi_b \end{bmatrix} + \begin{bmatrix} \sin(\psi_{des}) & 0 \\ \cos(\psi_{des}) & 0 \\ 0 & 0 \\ 0 & 1 \\ 0 & 0 \\ 0 & 0 \end{bmatrix} \begin{bmatrix} V_x^{radar} \\ \dot{\psi}^{gyro} \end{bmatrix} + w_1 \quad (4.14)$$

Because the yaw and steering dynamics are linear, the control states ( $X_2$ ) can be placed directly into the state space form:

$$\dot{X}_2 = A_2 X_2 + B_2 u + w_2 \quad (4.15)$$

where

$$\dot{X}_2 = \begin{bmatrix} 0 & 1 & 0 & 0 & 0 & 0 \\ -\omega_n^2 & -2\xi\omega_n & 0 & K_R\omega_n & 0 & 0 \\ 0 & 0 & 0 & 0 & 0 & 0 \\ 0 & 0 & 0 & 0 & 1 & 0 \\ 0 & 0 & 0 & 0 & -1/\tau_v & 0 \\ 0 & 0 & 0 & 0 & 0 & 0 \end{bmatrix} \begin{bmatrix} \psi \\ \dot{\psi} \\ v_x \\ \delta \\ \dot{\delta} \\ \delta_b \end{bmatrix} + \begin{bmatrix} 0 \\ 0 \\ 0 \\ 0 \\ -K_v/\tau_v \\ 0 \end{bmatrix} u + w_2 \quad (4.16)$$

The observation matrix ( $C$ ) is described by:

$$\begin{aligned} Y_{meas_1} &= C_1 x_1 + v_1 \\ Y_{meas_2} &= C_2 x_2 + v_2 \end{aligned} \quad (4.17)$$

where:

$$Y_{meas_1} = [E_{GPS} \quad N_{GPS} \quad \psi_{GPS}]^T$$

$$Y_{meas_2} = [\dot{\psi}_{meas} \quad V_{meas} \quad \delta_{pot}]^T$$

$v_1$  and  $v_2$  are sensor noise vectors (3x1 each)

Because the estimation of the biases associated with the yaw rate and velocity measurements are in the dead reckoning filter, the biases must be compensated for in order to utilize the measurements in the control filter as shown below.

$$\begin{aligned} \dot{\psi}_{meas} &= \dot{\psi}^{gyro} - g_b \\ V_{meas} &= V_x^{radar} - r_b \end{aligned} \quad (4.18)$$

The observation matrices for each of the filters are:

$$C_1 = \begin{bmatrix} 1 & 0 & 0 & 0 & 0 & 0 \\ 0 & 1 & 0 & 0 & 0 & 0 \\ 0 & 0 & 0 & 1 & 0 & 1 \end{bmatrix}$$

$$C_1 = 0 \text{ (3x5) if GPS is not available} \quad (4.19)$$

$$C_2 = \begin{bmatrix} 1 & 0 & 0 & 0 & 0 \\ 0 & 1 & 0 & 0 & 0 \\ 0 & 0 & 1 & 0 & 1 \end{bmatrix}$$

It is important to note that setting  $C_1=0$  forces the Kalman gain ( $L$ ) to become zero, such that the measurement values ( $Y_1$ ) have no effect in the estimation during the GPS outages.

The dead reckoning estimator is updated using the EKF Equations (4.10-4.11) given previously. The  $\dot{X}$  in the time update of the EKF (Equation 4.11) is calculated using the nonlinear Equations (4.12). The control estimator uses the same time update equations presented in Equation (4.10). However, because the control estimator is a linear filter, the time update is described by:

$$\begin{aligned} \hat{x}_{k+1} &= \Phi \hat{x}_k + \Gamma u_k \\ P_{k+1} &= \Phi P_k \Phi^T + Q_w \end{aligned} \quad (4.20)$$

where:  $\Phi$ =discretized State Matrix  $A_2$   
 $\Gamma$ = discretized input matrix  $B_2$   
 $Q_w$ =discretized process noise covariance matrix

The same process and sensor noise values given in Table 4.1 and Table 4.2 are used to form the process and sensor noise matrices,  $Q_w$  and  $R_v$ , respectively. When no GPS measurements are available, the EKF uses the time update step (Equation (4.11)) to

integrate forward and estimate all ten states from the remaining available measurements (velocity, yaw rate, and steer angle).

A simulated step response for tracking a line was performed with realistic sensor noises. Four biases (steer angle, heading, yaw gyroscope, and radar of 0.1, 0.2, 0.3 and 0.4, respectively) were added to each of the measurements. The convergence of the bias estimation of the four biases to their true values can be seen in Figure 4.6.

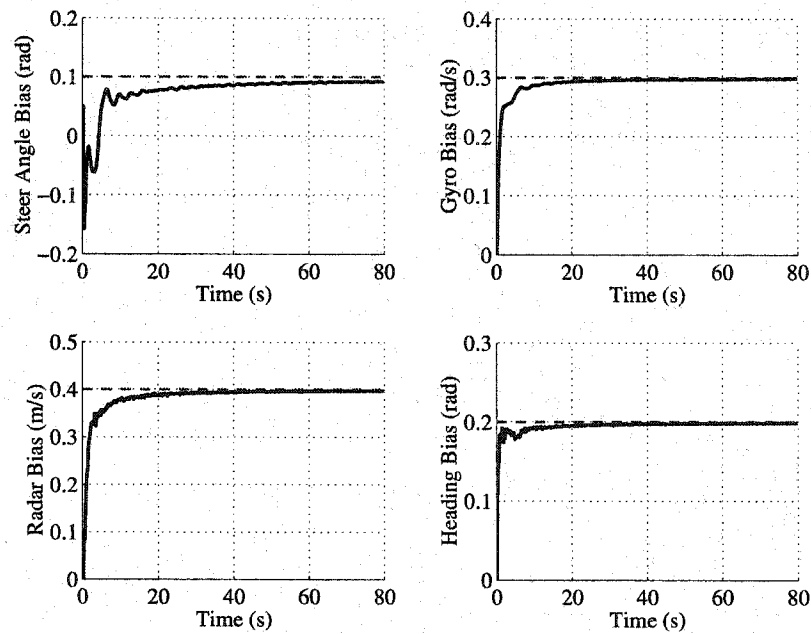


Figure 4.6 Estimation of All Four Biases During a Simulated Straight Line Tracking Run with an Initial Lateral Step Input of 1m.



## 4.4 Experimental Results

The dead reckoning system was implemented on a John Deere 8400 tractor (see Appendix A). The tractor was given a line trajectory to follow in order to validate the cascaded estimation scheme. The majority of the experimental runs were performed at about 2 m/s (4.5 mph). No Euler angle compensation of pitch and roll for the gyroscope yaw rate was performed in this work. Fields were assumed to be level such that the vehicle yaw rate was equal to the yaw rate in the inertial frame. Additionally, if the tractor is controlled along a side slope (about a position defined on the side slope) then the measured yaw rate is appropriate yaw rate, relative to the terrain, and no Euler compensation need be performed.

Figure 4.7 shows separate gyroscope and steer angle bias estimation, as well as the gyroscope and steer angle measurements. The tractor was under automatic steering control tracking a straight line. Therefore, the mean steer angle and yaw rate should be zero (assuming no vehicle crab angle), resulting in bias estimates equal to the mean of the measurements. It can be seen that the steer angle and yaw gyroscope biases are being estimated correctly, independent of each other.

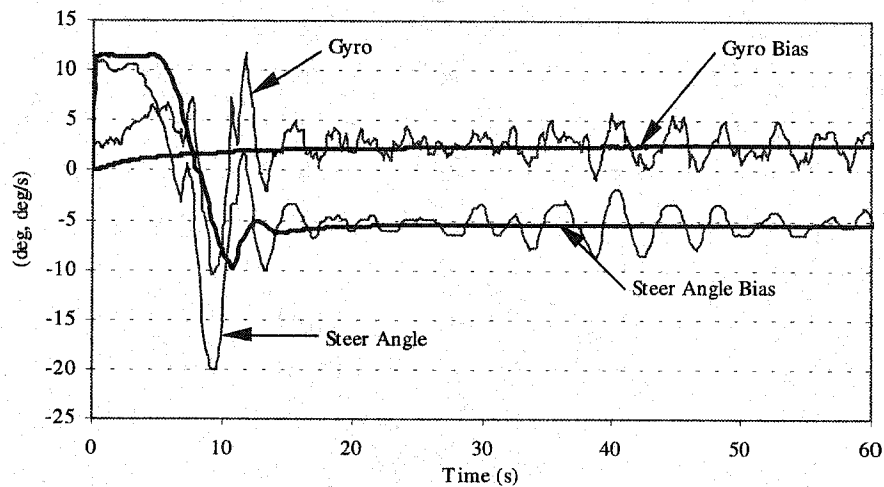


Figure 4.7 Experimental Validation of Separate Bias Estimation of Steer Angle and Gyroscope Biases During Straight Line Tracking.

### 4.4.1 Rough Verification of Bias Estimates

To validate the radar bias estimate, a rough estimate of the bias is formed as follows. A time difference estimate of the vehicle velocity can be obtained from a single difference of two consecutive position measurements as shown in Equation (4.21).

$$\hat{V} = \frac{\sqrt{(E(k+1) - E(k))^2 + (N(k+1) - N(k))^2}}{\Delta t} \quad (4.21)$$

A rough estimate of the radar bias can then be obtained by observing the difference between the velocity estimate and the radar measurement.

$$\Delta V_x = \hat{V} - radar \quad (4.22)$$

The above “measurement” of the radar bias will be quite noisy, as it is taking the difference between a noisy sensor measurement and a noisy velocity estimate. However, if the radar bias estimate is tuned satisfactorily, the bias estimate should filter this noisy difference. Figure 4.8 shows the radar and heading angle bias estimations. The tractor is again under automatic steering control tracking a straight line due North ( $\psi=0$  deg) as in Figure 4.7. The change in crab angle and the ability to track the changing crab angle can be seen over time for this run. This crab angle can be a combination of heading sensor bias (from sensor misalignment) and changing lateral velocity due to uneven terrain. Additionally, the effective filtering of the radar offset is seen in the radar bias estimate.

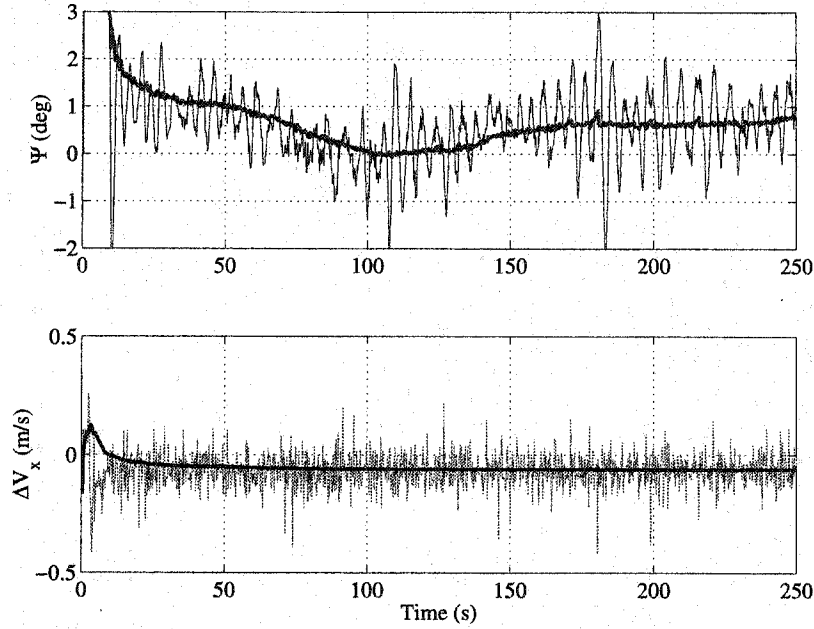


Figure 4.8 Heading and Radar Bias Estimation During Experimental Straight Line Tracking.

Figure 4.9 shows a plot of the difference between the actual heading and the estimated heading using the yaw gyroscope during a GPS outage. This figure is the same run shown in Figure 4.3 (GPS has been removed and brake disturbances were added to alter the vehicle heading), but with the use of the cascaded estimators such that the gyroscope is explicitly being integrated to provide heading estimates during the GPS outage. As seen in the figure, the explicit integration of the yaw gyroscope is able to estimate the heading of the tractor to within  $\pm 0.6$  deg for a 30 s outage as compared with 10-15 deg shown in Figure 4.3. The fact that the error resembles the heading is due to a small error in the gyroscope scale factor. Estimation of this scale factor error is an avenue for future work as discussed in Chapter 8.

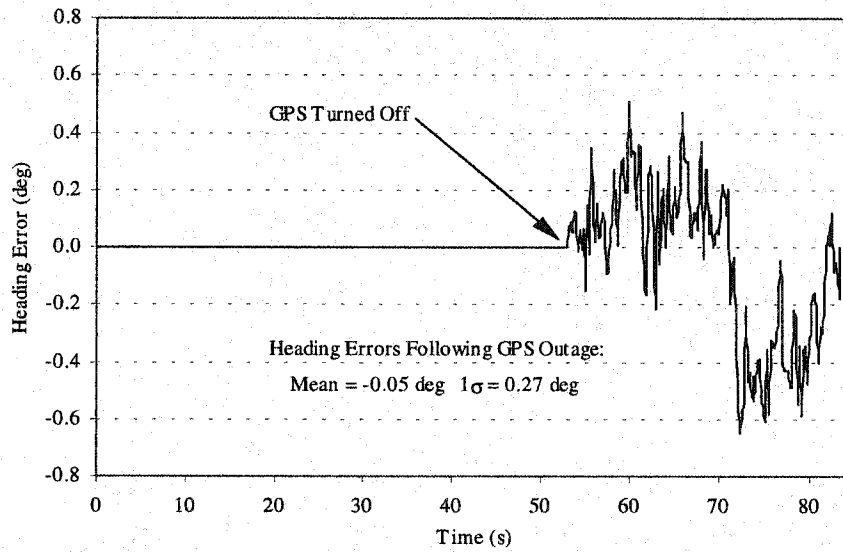


Figure 4.9 Heading Error Through Explicit Integration of the Yaw Gyroscope From the Cascaded Estimation Technique. Brake Disturbances are Added After a Simulated GPS Outage.

## 4.5 Conclusions

This chapter has discussed the use of a cascaded bias estimation technique consisting of two cascaded estimators to estimate all of the states necessary for full state feedback and dead reckoning. The cascaded estimation technique will be shown to provide adequate positioning and state estimation to control a tractor through short GPS outages in the next chapter. The estimator was also shown to be able to estimate the conflicting steer bias and gyroscope bias. The cascaded architecture was shown to have many advantages over a traditional estimation algorithm. The estimator in this chapter was developed in inertial coordinates, but could have been done alternatively in tractor body coordinates. Future researchers should investigate if this approach would decrease the complexity of the estimator by removing the non-linearities due to the rotational transformation from fixed to body coordinates.



## Chapter 5

# Dead Reckoning Analysis

As discussed previously, it is important to provide continuous control of a farm tractor through short GPS outages or loss of communication with the reference station. The ability of an inexpensive dead reckoning system, using a low cost Inertial Navigation System (INS) and initialized using carrier phase differential GPS, to provide adequate position and attitude estimation for the control of a farm tractor during short GPS outages is evaluated. This chapter also explores the errors associated with dead reckoning of the tractor through short GPS outages. Simulated GPS outages are created by removing the GPS position and attitude measurements from the estimator. The GPS measurements are recorded to evaluate the performance of the dead reckoning estimator.

The dead-reckoning estimator described in Chapter 4 (utilizing an Extended Kalman Filter) is shown to provide heading to within  $\pm 1$  degree and position estimation to within 0.3 meters for control of the farm tractor during 20-40 second GPS outages. Furthermore, it may be possible to reacquire carrier-phase integers (i.e., estimate position to within 9 cm) after GPS outages of less than 5 seconds, through the continuous position estimation of the dead reckoning system. Analysis based on the short-term integration of sensor noise is used to determine the error growth on the position estimate over time. It is shown that the integration of the IMU sensor noise at 5 Hz is the major source of error, motivating the use of higher sample rates on the dead reckoning estimator. Results are

given which verify the ability of the dead reckoning system's position and attitude estimation for control of a farm tractor through a short GPS outage.

## 5.1 Error Analysis

The growth of positioning errors over time are a function of the integration routine as well as the sensor noises and biases. Analysis for the growth of heading errors from the discrete integration of sensor noise has been developed in [Gebre-Egziabher, 2001(a)] and is shown below. The following error analysis assumes that the static covariance of the sensor noise does not change with sample rate. In other words, no optimal pre-filtering, based on the sample rate, is performed. An optimal pre-filter or anti-aliasing filter whose bandwidth is reduced with the sample rate will provide more sensor filtering. This would then decrease the covariance of the sensor noise as the sample rate is lowered.

### 5.1.1 Heading Error Analysis

Assuming the bias of the gyroscope has been accurately removed using the estimator in Chapter 4, the remaining gyroscope's sensor reading is:

$$\dot{\psi}^{gyro} = \dot{\psi} + v^{gyro} \quad (5.1)$$

where:  $v^{gyro}$  is serially uncorrelated white sensor noise of the gyroscope.

Integration of the gyroscope to get heading results in:

$$\int (\dot{\psi} + v^{gyro}) = \int \dot{\psi} + \int v^{gyro} = \psi + \psi^e \quad (5.2)$$

Assuming perfect integration of the yaw rate, the heading error ( $\psi^e$ ) is due only to the integration of the sensor's noise.

$$\psi^e = \int v^{gyro} \quad (5.3)$$

Using an Euler integration routine to obtain heading from the yaw gyroscope results in the following discrete equation for the heading error.

$$\psi_{k+1}^e = \psi_k^e + T_s v_k^{gyro} = \sum_{i=1}^k T_s v_i^{gyro} \quad (5.4)$$

where:  $T_s$  = Sample Rate

Squaring and taking the expected value of the above equation results in:

$$E[\psi^e (\psi^e)^T] = E[(\sum T_s v^{gyro})(\sum T_s v^{gyro})^T] = T_s^2 \left( \sum_{i=1}^k E[v_i^{gyro} (v_i^{gyro})^T] \right) \quad (5.5)$$

Knowing that the expected value of the square of the gyroscope's sensor noise is simply the covariance of the gyroscope noise ( $\sigma_{v^{gyro}}^2$ ) results in:

$$\sigma_{\psi^e}^2 = T_s^2 k \sigma_{v^{gyro}}^2 = T_s t \sigma_{v^{gyro}}^2 \quad (5.6)$$

The above equation results in the following equation for the heading error growth from the integration of sensor noise as a function of time:

$$\sigma_{\psi^e} = \sigma_{v^{gyro}} \sqrt{T_s t} \quad (5.7)$$

Figure 5.1 shows the integration of a static gyroscope ( $\sigma_{v^{gyro}} = 0.44$  deg/sec) in the tractor for 1 minute at 5 Hz and 100 Hz. As seen in the figure, Equation (5.7) adequately describes the random walk due to discrete integration of the gyroscope noise. Additionally, the effect of sampling rate on the heading error can be easily seen assuming the same noise statistics for each sample rate. Figure 5.2 shows a Monte-Carlo simulation used to validate the heading error growth.

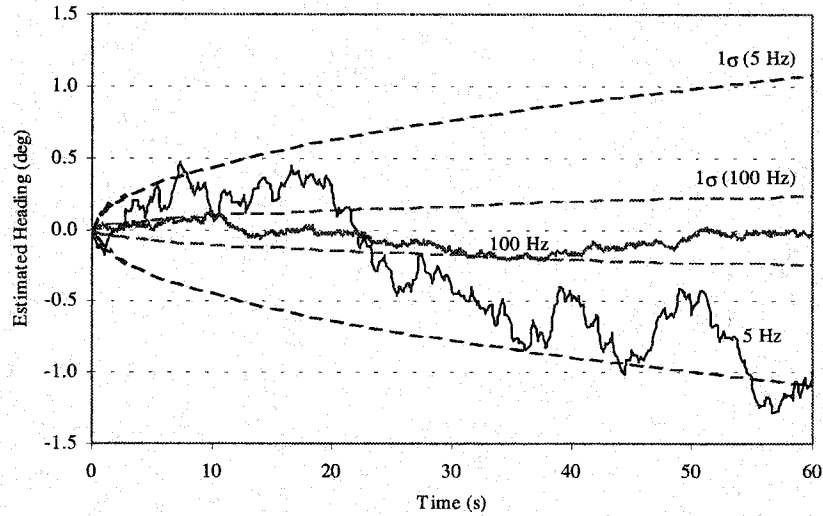


Figure 5.1 Integration of Gyroscope Noise.



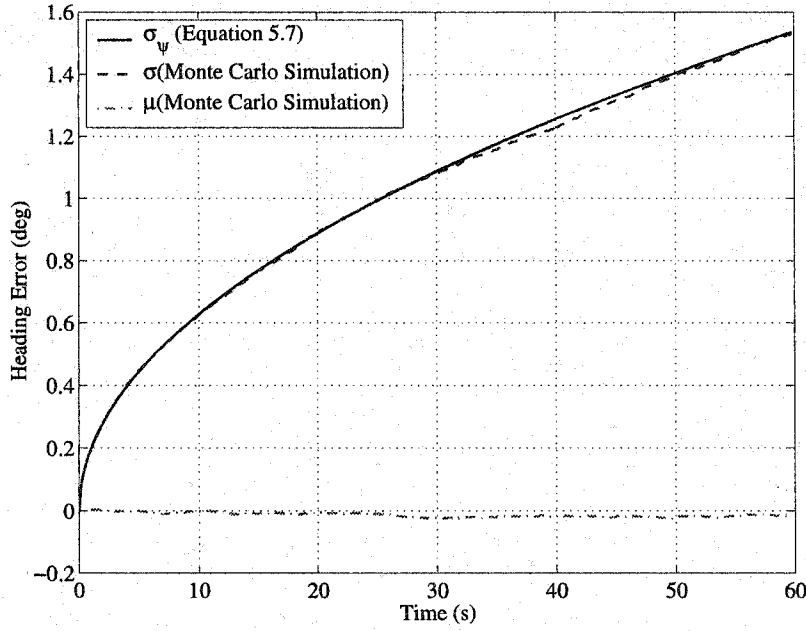


Figure 5.2 Validation of the Heading Error Growth Using a Monte Carlo Simulation.

### 5.1.2 Lateral Error Analysis for the Stationary Case

The above error analysis of [Gebre-Egziabher, 2001(a)] can be extended to the lateral dynamics of the tractor to determine the effect of the discrete integration of the yaw rate and velocity noises on the growth of lateral errors. Assuming that the bias of the radar has been accurately removed using the estimator in Chapter 4, the remaining radar's sensor reading is:

$$V^{radar} = V + v^{radar} \quad (5.8)$$

where:  $v^{radar}$  is serially uncorrelated white sensor noise of the radar.

Integration of the radar times the heading angle to get lateral position ( $y$ ) results in

$$y + y^e = \int (V + v^{radar}) \sin(\psi + \psi^e) \quad (5.9)$$

Assuming the mean velocity and heading are equal to zero, the lateral error ( $y^e$ ) is due to the integration of the sensor's noise times the heading error.

$$y^\varepsilon = \int v^{radar} \sin(\psi^\varepsilon) \quad (5.10)$$

Again, an Euler integration of the sensor outputs results in:

$$y_{k+1}^\varepsilon = y_k^\varepsilon + T_s v_k^{radar} \sin(\psi^\varepsilon) \approx y_k^\varepsilon + T_s v_k^{radar} \psi_k^\varepsilon = \sum_{i=1}^k T_s v_i^{radar} \psi_i^\varepsilon \quad (5.11)$$

Squaring and taking the expected value of the above equation results in:

$$E[y^\varepsilon (y^\varepsilon)^T] = E\left[\left(\sum T_s v_i^{radar} \psi_i^\varepsilon\right) \left(\sum T_s v_i^{radar} \psi_i^\varepsilon\right)^T\right] \quad (5.12)$$

Because the radar noise and heading errors are uncorrelated:

$$E[y^\varepsilon (y^\varepsilon)^T] = T_s^2 \left( \sum_{i=1}^k E[\psi_i^\varepsilon (\psi_i^\varepsilon)^T] E[v_i^{radar} (v_i^{radar})^T] \right) \quad (5.13)$$

Knowing that the expected value of the square of the radar's noise is simply the covariance of the radar noise ( $\sigma_{v^{radar}}^2$ ) and using the expected value for heading from Equation (5.7):

$$\begin{aligned} E[y^\varepsilon (y^\varepsilon)^T] &= T_s^2 \left( \sum_{i=1}^k \left[ T_s^2 \left( \sum_{j=1}^k v_j^{radar} v_j^{radar} \right) \right] \sigma_{v^{radar}}^2 \right) \\ &= T_s^4 \sum_{i=1}^k k \sigma_{v^{gyro}}^2 \sigma_{v^{radar}}^2 = T_s^4 \sigma_{v^{gyro}}^2 \sigma_{v^{radar}}^2 \sum_{i=1}^k k \end{aligned} \quad (5.14)$$

Simplifying the above equation results in the covariance of the lateral error growth:

$$\sigma_{y^\varepsilon}^2 = T_s^4 \sigma_{v^{radar}}^2 \sigma_{v^{gyro}}^2 \left( \frac{1}{2} k^2 + \frac{1}{2} k \right) \approx \frac{1}{2} k^2 T_s^4 \sigma_{v^{radar}}^2 \sigma_{v^{gyro}}^2 = \frac{1}{2} (T_s t)^2 \sigma_{v^{radar}}^2 \sigma_{v^{gyro}}^2 \quad (5.15)$$

The above equation results in the following approximation for the lateral error growth due to integration of the yaw gyroscope and radar noises:

$$\sigma_{y^\varepsilon} \approx T_s t \sigma_{v^{radar}} \sigma_{v^{gyro}} \sqrt{\frac{1}{2}} \quad (5.16)$$

The above estimate of the lateral error growth is due only to integration of the noise in the radar and gyroscope sensors, and only provides the correct estimation of the lateral error growth when the vehicle is not moving (average velocity is equal to zero). This is because the analysis assumes that both processes are zero mean. Figure 5.3 shows a Monte Carlo simulation to validate the lateral error growth at  $V_x=0$  m/s. The covariance of the radar and gyroscope measurement noise is given in Table 4.2.

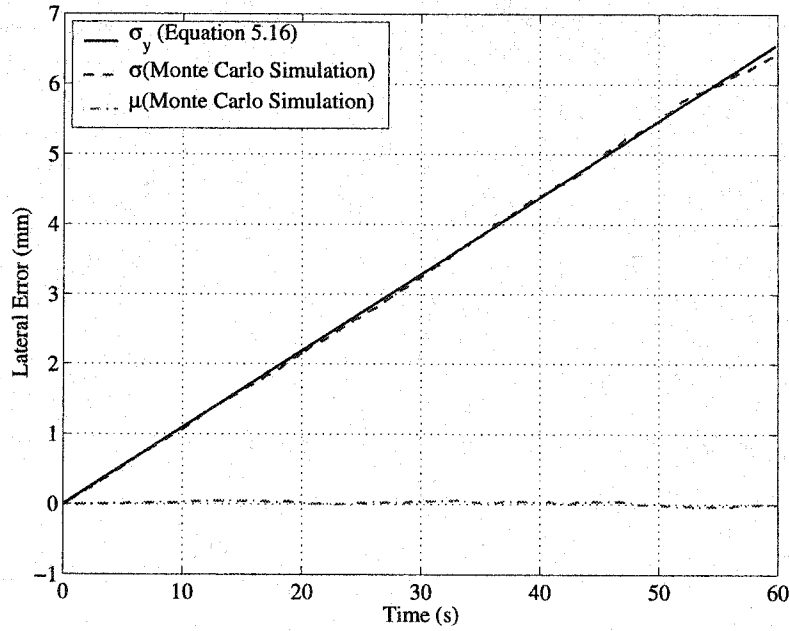


Figure 5.3 Validation of the Lateral Error Growth for the Stationary Case Using a Monte Carlo Simulation.

### 5.1.3 Lateral Error Analysis for the Non-Stationary Case

While the vehicle is moving, the lateral errors are not dominated by the integration of radar noise, but rather the propagation of the position from the heading error found in Equation (5.7). Therefore, utilizing the lateral error dynamics in Equation (3.3) and substituting the heading error from Equation (5.7) results in a better description of the lateral error growth. Neglecting the radar noise and assuming the mean heading is equal to zero, the lateral error ( $y^e$ ) is due to the integration of the vehicle velocity times the heading error.

$$y^e = \int V \sin(\psi^e) \quad (5.17)$$

Again, using an Euler integration of the sensor outputs results in:

$$y_{k+1}^e = y_k^e + T_s V \sin(\psi_{k+1}^e) \approx y_k^e + T_s V \psi_{k+1}^e = \sum_{i=1}^k T_s V \psi_{i+1}^e \quad (5.18)$$

Substituting Equation (5.4) for the heading error into the above equation results in:

$$y_{k+1}^e = \sum_{i=1}^k T_s V \psi_{i+1}^e = \sum_{i=1}^k \left[ T_s V \sum_{j=1}^k v_j^{gyro} \right] = T_s^2 V \sum_{i=1}^k k v_{k-i+1}^{gyro} \quad (5.19)$$

Squaring and taking the expected value of the above equation results in:

$$\begin{aligned} E[y^e (y^e)^T] &= E \left[ T_s^2 V \left( \sum k v_{k-i+1}^{gyro} \right) \left( T_s^2 V \sum k v_{k-i+1}^{gyro} \right)^T \right] \\ &= T_s^4 V^2 \left( \sum_{i=1}^k k^2 E \left[ \left( v_i^{gyro} \right) \left( v_i^{gyro} \right)^T \right] \right) \end{aligned} \quad (5.20)$$

Assuming that gyroscope measurement noises are serially uncorrelated with each other

$$E[y^e (y^e)^T] = T_s^4 V^2 E \left[ \sum_{i=1}^k k^2 \left( v_{k-i+1}^{gyro} \right)^2 \right] = T_s^4 V^2 \left( \sum_{i=1}^k k^2 E \left[ \left( v_i^{gyro} \right) \left( v_i^{gyro} \right)^T \right] \right) \quad (5.21)$$

Substitution the covariance of the gyroscope noise into the above equation results in:

$$\epsilon_y^2 = E[y^e (y^e)^T] = T_s^4 V^2 \sum_{i=1}^k k^2 \sigma_{v^{gyro}}^2 = T_s^4 V^2 \sigma_{v^{gyro}}^2 \sum_{i=1}^k k^2 \quad (5.22)$$

Simplifying the above equation results in the covariance of the lateral error growth:

$$\epsilon_y^2 = T_s^4 V^2 \sigma_{v^{gyro}}^2 \left( \frac{1}{3} k^3 + \frac{1}{2} k^2 + \frac{1}{6} k \right) \approx \frac{1}{3} k^3 T_s^4 V^2 \sigma_{v^{gyro}}^2 = \frac{1}{3} V^2 T_s^3 \sigma_{v^{gyro}}^2 \quad (5.23)$$

The above equation results in the following approximation for the lateral error growth due to integration of the velocity times the yaw gyroscope noise:

$$\epsilon_y \approx V \sigma_{v^{gyro}} \sqrt{\frac{1}{3} T_s^3} \quad (5.24)$$

In reality, the total error growth is the sum of errors from the integration of sensor noise (Equation (5.15)) and heading error (Equation (5.17)). However, the errors from Equation (5.15) are small compared to errors from Equation (5.17) (for the noise covariance values of the sensors used in this thesis) and can therefore be neglected. Figure 5.4 shows a Monte Carlo simulation to validate the lateral error growth at  $V_x=2$  m/s.

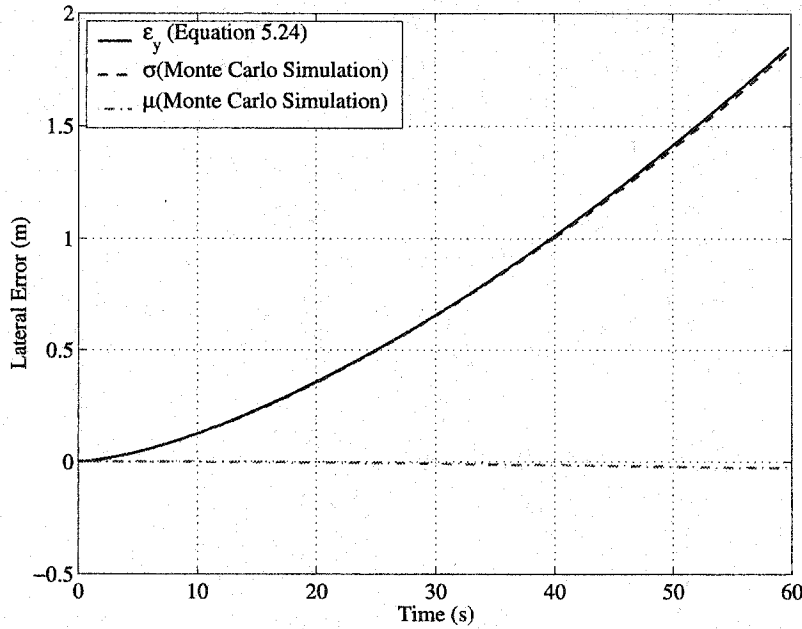


Figure 5.4 Validation of the Lateral Error Growth for the Non-Stationary Case Using a Monte Carlo Simulation.

Additionally, a similar analysis can be performed for the longitudinal dynamics. However, the growth of the lateral errors are a function of sine while the longitudinal error growth is a function of one minus cosine. Therefore, for small heading errors, the lateral errors grow as a function of the heading error and the longitudinal errors grow as a function of the heading error squared. Because the positioning errors associated with the lateral direction are much more significant than the errors in the longitudinal direction, the longitudinal error analysis was neglected.

Changes in crab angle (or lateral velocity from side-slip) are equivalent to a heading error that results in a growth of position errors as shown in Equation (5.16). Therefore, if the crab angle is changing on the same order as the error in heading, the growth in position errors can be as much as twice that obtained solely from heading errors. Unfortunately, increased sample rate cannot decrease the errors associated with changes in crab angle.

Errors in the gyroscope scale factor are negligible for straight-line tracking. However for U-turn operation, a scale error as small as ½% results in a heading error of 0.9 deg.

Additionally integration of the unknown bias will result in a linear growth of the heading error and a parabolic growth of the lateral errors. Although the bias is being estimated from the bias estimation, the bias tends to change over periods of time. However for short durations, the bias can be assumed constant, such that the errors associated with the drift of the bias can be neglected. There are also additional errors associated with the integration routine, which are a function of the routine and the sample rate [Chapra, 1989].

#### 5.1.4 Error Growth Prediction Through Covariance Propagation

Alternatively the state covariance propagation, from the Kalman filter time update in Equation (4.20), can be used to predict the state error growth due to integration of the gyroscope noise. The dynamics in Section 5.1.1 and 5.1.3 can be described by the following state space model:

$$\dot{x} = Ax + Bv^{gyro} \quad (5.25)$$

where:

$$x = \begin{bmatrix} y^e \\ \psi^e \end{bmatrix}, \quad A = \begin{bmatrix} 0 & V \\ 0 & 0 \end{bmatrix}, \quad B = \begin{bmatrix} 0 \\ 1 \end{bmatrix}$$

The above equation results in the following state covariance propagation (approximating the error growth due to integration of the yaw gyroscope noise) [Stengel, 1994]:

$$P = \Phi P_k \Phi^T + Q_d \quad (5.26)$$

where:

$$P = \begin{bmatrix} P_{11} & P_{12} \\ P_{21} & P_{22} \end{bmatrix} = \begin{bmatrix} E[(y^e)^2] & E[y^e \psi^e] \\ E[y^e \psi^e] & E[(\psi^e)^2] \end{bmatrix}$$

$\Phi$  = discretized state matrix ( $A$ )

For small sample rates (relative to the dynamics of the system) the discrete process noise matrix ( $Q_d$ ) can be approximated by [Franklin, 1998].

$$Q_d \approx \Gamma Q_c \Gamma^T \approx T_s^2 B Q_c B^T \quad (5.27)$$

where:

$$Q_c = E\left[\left(v^{gyro}\right)^2\right]$$

$\Gamma$  = discretized input vector ( $B$ )

An exact solution to  $Q_d$  can be obtained using the method in Section D.7 of [Bryson, 1994]. The covariance propagation given by Equation (5.26) results in the same error propagation for the heading error ( $P_{22}$ ) and lateral error ( $P_{11}$ ) as Equation (5.7) and Equation (5.24), respectively.

## 5.2 Experimental Dead Reckoning Results

As stated previously, the dead reckoning system was implemented on a John Deere 8400 tractor. The KVH fiber optic gyroscope (FOG) was used for sensing yaw rates and an onboard radar was used for measuring velocity. The covariances of the noise for these sensors are given in Table 4.2. The tractor was given a line trajectory to follow. The majority of the experimental runs were performed at about 2 m/s (4.5 mph). Time was given to allow the bias estimations to settle. Then both GPS position and attitude measurements were denied to the controller and estimation algorithms. GPS measurements were still recorded to analyze the performance of the dead reckoning algorithm.

Figure 5.5 shows a plot of the difference between the actual heading, measured by GPS, and the estimated heading using the yaw gyroscope during a simulated GPS outage. The uncertainty in the heading error (Equation (5.4)) is also shown. The tractor is equipped with differential braking which gives the ability to add a heading disturbance to the system by braking one side of the tractor. As seen in the figure, even under yaw disturbances (from differential braking) during experimental runs, the growth in heading error developed in Equation (5.7) describes the error quite well. Therefore, it can be concluded that for short durations (on the order of a minute), the major error from gyroscope integration at 5 Hz is due to the discrete integration of the sensor noise. Additionally, the accurate heading estimation from integrating the gyroscope demonstrates the effectiveness of the cascaded estimation architecture in Chapter 4 to accurately estimate and remove the gyroscope bias. Integrating the gyroscope at a higher

sample rate will reduce the heading error and increase the performance of the dead reckoning system. Again, this is under the assumption that any pre-filter does not exist or change, such that the covariance of the sensor noise remains the same regardless of the sample rate. However, as errors from integration of the gyroscope noise decrease (from increasing the sampling rate) other errors may become more dominant.

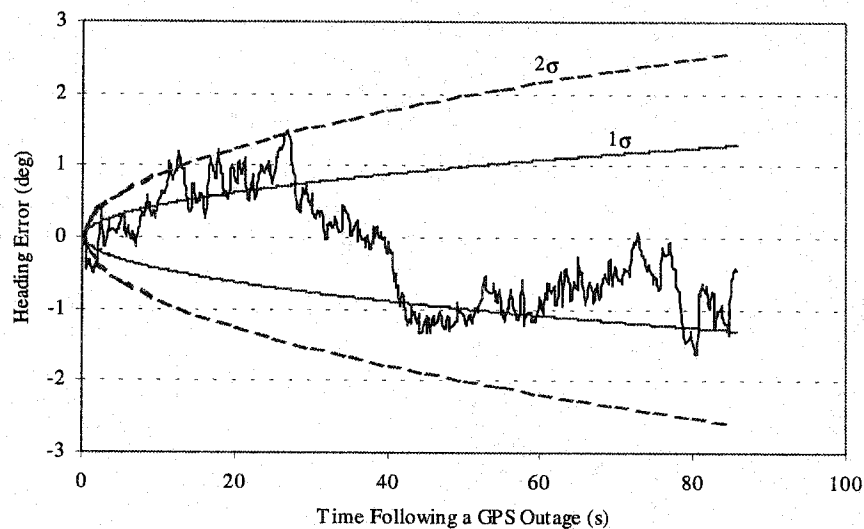


Figure 5.5 Heading Error Following a Simulated GPS Outage.

Figure 5.6 shows the lateral error of three runs performing straight line tracking at a typical tillage speed of 2 m/s. The figure plots the lateral error as a function of time after GPS measurements were removed. Most of the runs had an estimation error within  $\pm 0.3$  m (1 foot) for over 40 seconds of a “GPS Outage.” This figure shows that for short durations of GPS outages the estimator is still able to produce state estimates to control the tractor. The lateral errors remained below 9 cm (half of a GPS Carrier-Phase cycle length) for only 5-10 seconds as shown in the lower figure. The 9 cm error bound is what is necessary to identify the Carrier-Phase integers after a GPS outage. However, continuous positioning accuracy of 0.3 m is adequate for some tillage farm operations (since it is comparable to the average overlap of most human operators [Palmer, 1988]). Additionally, search algorithms can be used to produce integer solutions more rapidly by providing a decreased search space from knowledge of the vehicle position to within 0.3 m.



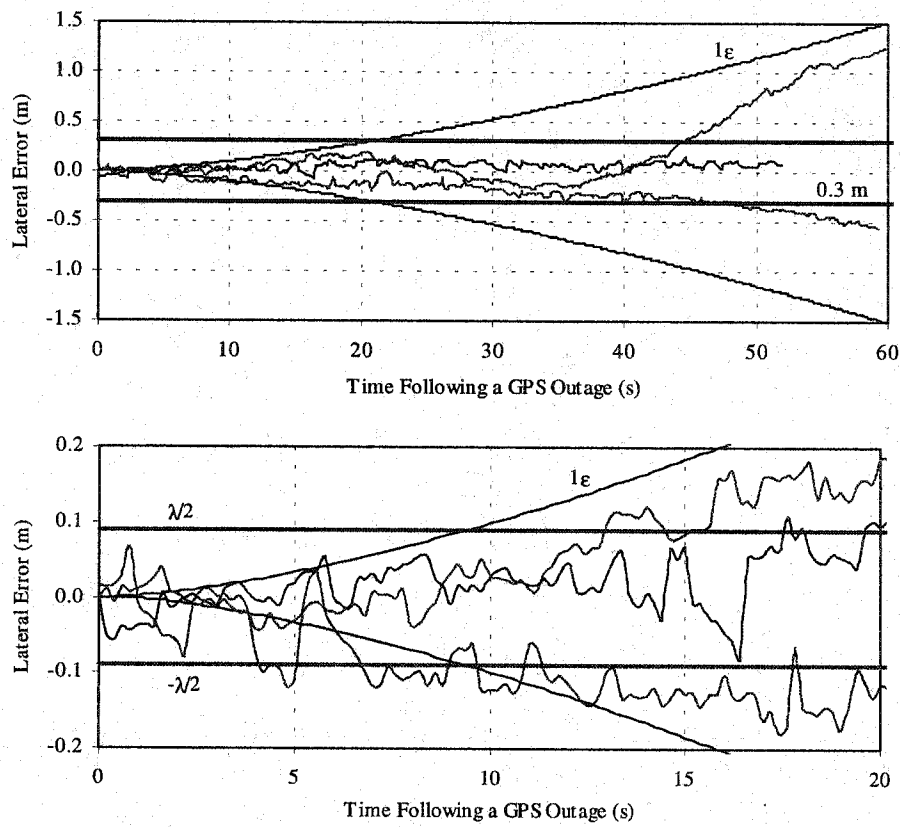


Figure 5.6 Lateral Error Following a Simulated GPS Outage. The Top Figure Shows the  $\pm 0.3$  m (1 foot) Boundaries, While the Bottom Figure is Zoomed In to Show the  $\pm \frac{\lambda}{2}$  Boundaries.

Figure 5.7 shows the difference between the estimated and actual positions for 42 seconds of one data run. The inner circle represents a 9 cm error bound (half a GPS wavelength) while the outer circle represents a 0.3 m error bound. Although the error has grown to 9 cm in only 8 seconds, the tractor has been controlled for 16 m. Therefore, the dead reckoning error is on the order of 0.5%. Additionally, 40 seconds of control within 0.3 m also represents 0.5% of dead reckoning error. The tractor is being controlled along a linear trajectory. As mentioned previously, the lateral errors grow much faster than the longitudinal errors. This can be seen by the fact that the position errors are along the lateral axis. Figures 5.6-5.7 demonstrate the feasibility of being able to recover integers after 10-15 m of dead reckoning at typical farm speeds of 2 m/s.

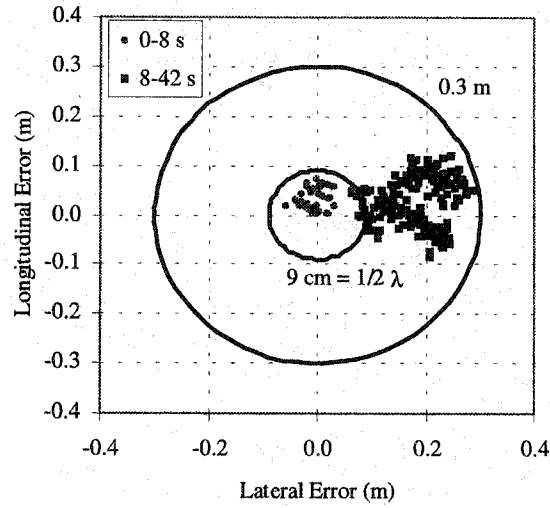


Figure 5.7 Dead Reckoning Position Errors After a Simulated GPS Outage for a Single Dead Reckoning Experiment.

Figure 5.8 illustrates the effects of the three errors on the dead reckoning system: heading error from integration of the gyroscope, errors due to unknown crab angle, and errors due to integration of the radar sensor. The figure shows the difference in dead reckoning from using the gyroscope heading, GPS heading, and GPS velocity heading or course. The direction of travel (velocity heading) and GPS heading are not available during a GPS outage, but are simply used to illustrate that the major error in lateral position can occur from changes in crab angle (i.e., sideslip), which are not known during the outage. The crab angle is being estimated while GPS is available. However, once GPS measurements are lost, the crab angle can no longer be estimated and must be assumed to remain constant. In this figure, the system was controlled along a line using heading estimation from the gyroscope after GPS was turned off. The data was then post-processed using the GPS and velocity headings for comparison. The velocity heading is obtained by looking at the direction of two consecutive position measurements as shown below.

$$\psi_{vel} = \tan^{-1}\left(\frac{V_{east}}{V_{north}}\right) = \tan^{-1}\left(\frac{e_k - e_{k-1}}{n_k - n_{k-1}}\right) \quad (5.17)$$

As seen in the figure, the gyroscope heading is able to estimate the lateral position nearly as well as using the actual vehicle heading (from GPS). This is because the gyroscope can accurately estimate vehicle heading to within one degree for short (30-40 second) periods as seen previously. The difference in lateral error from using the gyroscope estimated heading and the vehicle heading remains less than 0.3 meters.

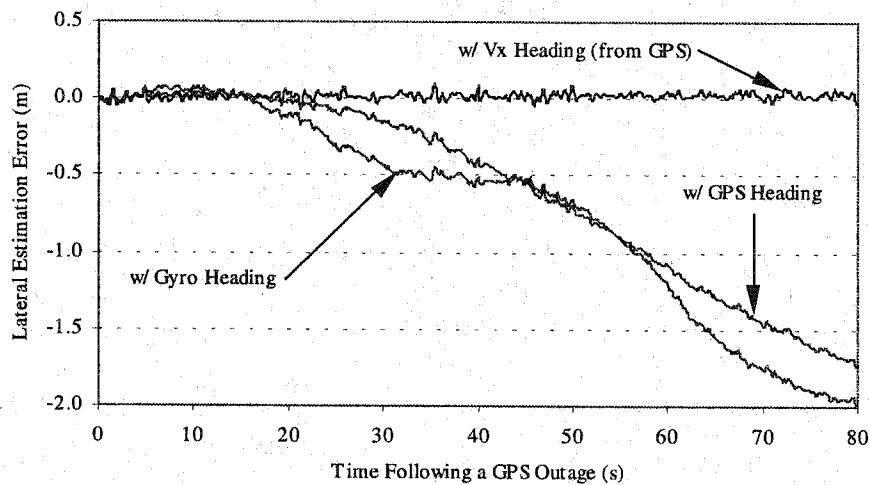


Figure 5.8 Lateral Estimation Errors due to Integrating Various Headings (Demonstrating the Effect of Crab Angle on the Errors).

The dead reckoning system using GPS heading as well as the estimated heading from the gyroscope results in large errors as the crab angle changes. The crab angle in this experiment was constant for about 20 seconds, during which time the lateral errors are quite small. However, after 20 seconds, the crab angle changed less than 1 deg (violating the assumption that it remains constant), which led to a linear growth in the lateral error. This change in crab angle could be attributed to a number of factors such as a tire getting caught in a furrow. Additionally, crab angle has been shown to change with changes in terrain side-slope [Bell, 1998]. If the exact vehicle velocity direction is known, the dead reckoning system can estimate the lateral position very accurately (within 0.1 m during the 80 seconds in Figure 5.8). The growth of errors from using the velocity heading (which cannot be seen due to the scale of the figure) are due to the integration of the radar noise. However, as mentioned previously, these errors become insignificant compared to the lateral errors produced from errors in heading. If the crab angle remains constant, the

dead reckoning system can provide good accuracy. However, even on level ground, disturbances and implements can produce small changes in crab angles that then become the major cause of errors. Because the crab angle is being estimated in real time, the variance of the crab angle over time can be monitored to provide realistic estimate of the dead reckoning errors during a GPS outage.

Figure 5.9 represents the use of the entire dead reckoning algorithm. The first lap around the desired trajectory (shown by a dashed line) was performed clockwise by the tractor under automatic steering control using GPS measurements. GPS measurements were then removed and the tractor drove three additional laps around the track (requiring over 3 minutes) with no position or attitude measurements. The decrease in dead reckoning performance over time can be seen in the increased error at the end of the fourth lap around the track.

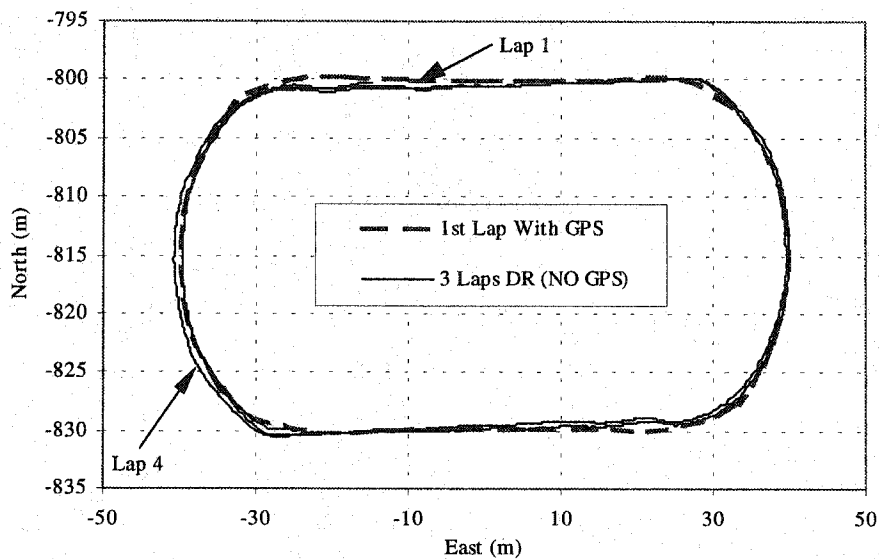


Figure 5.9 Dead Reckoning Performance Around a Track.

The tracking errors for the first lap as well as the errors from the first two dead reckoning laps are shown in Figure 5.10. Errors for the last lap grew substantially, due to a change in the gyroscope bias, and are therefore not shown in the figure. The position and heading errors listed in the figure are for the two laps with no GPS measurements.

The periodicity of the errors is due to an error in the gyroscope scale factor. As mentioned previously, this is an avenue of future work as discussed in Chapter 8.

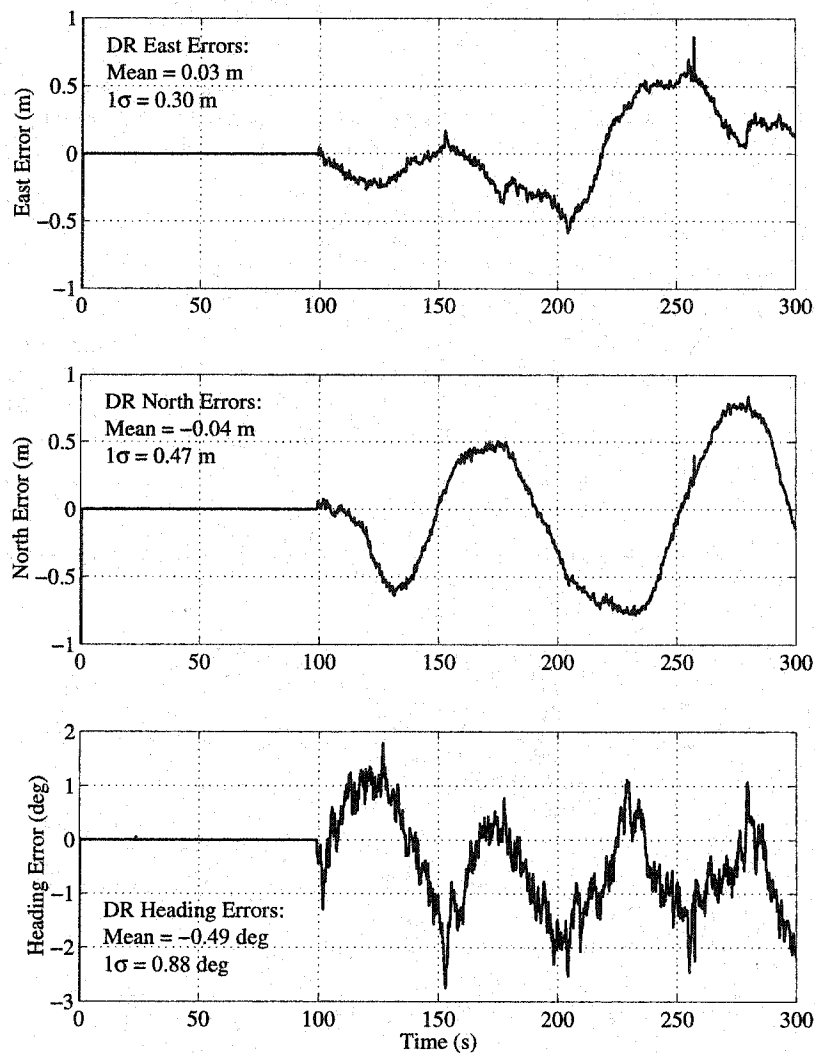


Figure 5.10 Dead Reckoning Errors Around the Track.

## 5.3 Conclusions

The accuracy of the dead reckoning controller using low cost inertial sensors initialized with Carrier Phase GPS was discussed in this chapter. Experimental results were given that demonstrate the capabilities of the inertial-aided dead reckoning system to maintain 9 cm accuracy for 5-8 seconds (or about 10-16 meters). Results also show that the dead reckoning system was able to maintain lateral errors within 0.3 meters for about 30-40 seconds during a GPS outage. Although 9-cm accuracy is necessary to reacquire integers, 0.3 meters provides adequate accuracy for many farm tillage operations (during a short GPS outage). It was also shown that the integration of the gyroscope could estimate the vehicle heading to  $\pm 1$  deg during the 20-40 second outages. Therefore, INS can be coupled with GPS to provide continuous control of a farm tractor with accuracies adequate for tillage operations through the duration of any reasonably expected GPS outage.

Equations for the growth of heading and lateral errors were developed and shown to predict the errors in experimental tests. The errors were seen to be a function of the sample rate, such that increasing the sampling rate of the yaw gyroscope and velocity sensor could decrease the errors (assuming the covariance of the sensor noise did not change as a function of sample rate). Dead-reckoning performance of a farm tractor can be predicted using the presented analysis. This will allow designers to look at tradeoffs of using various sensors, as well as evaluate the merits of integrating GPS with inertial sensors for control of farm equipment. However, it was shown that changes in crab angle can become the largest contribution of lateral errors of the dead reckoning system. Changes in crab angle cannot be estimated during a GPS outage, and errors associated with crab angle are not a function of sample rate.



## Chapter 6

# Partial INS Based Attitude for Control of a Tractor

This chapter explores the use of a Partial Inertial Navigation System (PINS) based attitude methodology, as an alternative to multiple antenna GPS attitude, for the control of the farm tractor. Previous chapters have assumed that full attitude measurements of the tractor are available through a multiple GPS antenna system. The PINS system is comprised of one lateral accelerometer for measuring roll and one yaw rate gyroscope. This system currently provides a less expensive attitude solution than the multiple GPS antenna system. While the PINS heading will drift over time, if left uncorrected, it does not suffer from GPS errors resulting from multi-path and antenna blockages. A Kalman filter incorporates the PINS measurements with cm-level Carrier-Phase Differential GPS (DGPS) measurements from one position antenna for complete position and attitude estimation of an off-road vehicle. The cm-level accuracy of DGPS allows for precise calibrations of the PINS system to eliminate drift. Because GPS attitude measurements are not available, an estimate of vehicle heading and roll must be constructed. A heading estimator using noisy heading measurements from a single GPS antenna, known as vehicle course, is incorporated with a rate gyroscope to provide accurate heading estimates. This heading estimate assumes no sideslip or crab angle. Because there is no heading measurement using GPS in this chapter, it is not possible to estimate crab angle



as was done in Chapter 4. A simple low pass filter was designed (based on an analysis of the roll frequency) and shown to provide satisfactory estimates of vehicle roll. Because most farm applications occur at constant speed, it is usually not necessary to account for low frequency vehicle accelerations as in [Hayward,1999]. The large amounts of higher frequency vibration accelerations experienced in off-road vehicles can be filtered out.

This chapter shows that a low cost PINS system is capable of providing the attitude accuracy necessary for cm-level control of an off-road vehicle. Results are shown using the PINS system, in conjunction with DGPS position measurements, to autonomously control the farm tractor. This chapter also compares the lateral control performance of various sensor options in simulation. Experimental results using low-cost inertial sensors are compared to the use of GPS based attitude for the control of a farm tractor. These results show the ability of the low cost PINS attitude system integrated with a single GPS receiver on the tractor to provide lateral tracking accuracies of 3 cm ( $1\sigma$ ) on level ground with a calibrated y-axis accelerometer. These results are comparable to the accuracies obtained using the GPS attitude system.

## 6.1 Effect of Roll

The major need for roll measurements is created by the fact that the GPS antenna is located at the top of the cab of the tractor so that it may be visible to as many of the overhead satellites as possible. As seen in Figure 6.1, vehicle roll ( $\phi$ ) creates lateral position errors due to the non-collocation of the GPS antenna and the control point (CP) which is located on the ground between the rear wheels. The lateral error at the CP is simply:

$$y_{error} = -h \sin(\phi) \quad (6.1)$$

where  $y_{error}$  is the lateral difference between the GPS position and the CP.

Even if the terrain is fairly flat, small irregularities in the ground will lead to position errors and can even cause the controlled system to become unstable. Analysis has shown that for a typical lever arm height ( $h$ ) correction of 3 meters, positioning errors from roll measurement noise ( $1\sigma$ ) exceeding 0.4 deg will exceed the of DGPS measurement noise

[Bell, 1999]. Therefore, to utilize the cm level accuracy of DGPS, roll measurement noise must be less than 0.4 deg.

Pitch motion of the vehicle creates longitudinal positioning errors. However in the steering control of the farm tractor, there is no ability to control motion in the longitudinal direction. Because only lateral tracking is being controlled, pitch motion was ignored in this work.

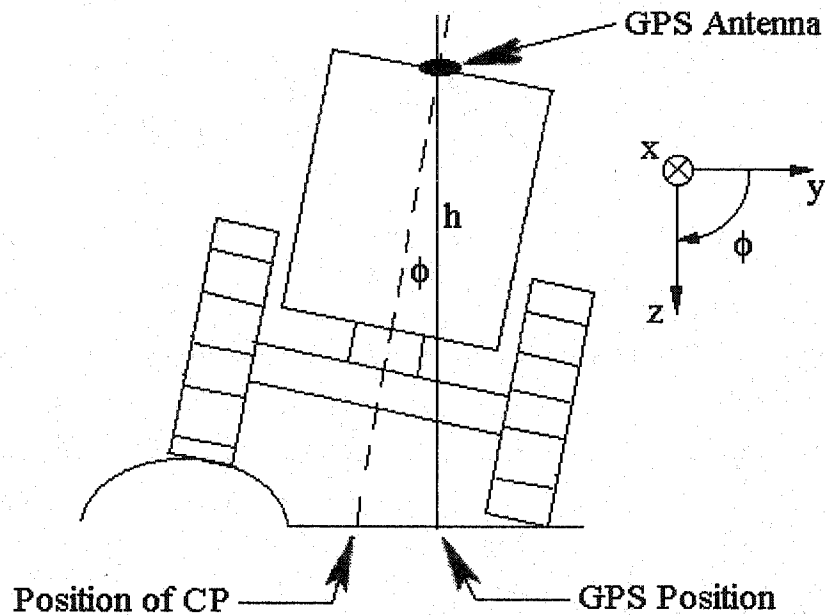


Figure 6.1 Effect of Positive Roll on GPS Measurements.

## 6.2 Estimation Algorithm Using PINS Attitude

The work in this chapter is concerned only with comparing control of the tractor using GPS attitude to control using PINS based attitude. Because this chapter is not concerned with dead reckoning, no radar measurements are used. The estimation algorithm used for this work is very similar to the estimation algorithm discussed in Chapter 4. However, because there are no GPS attitude measurement (as in Chapter 4)

and a few different sensor combinations, the estimation algorithm is discussed again for this chapter. Figure 6.2 shows a schematic of an off-road vehicle including its CG and control point (CP).

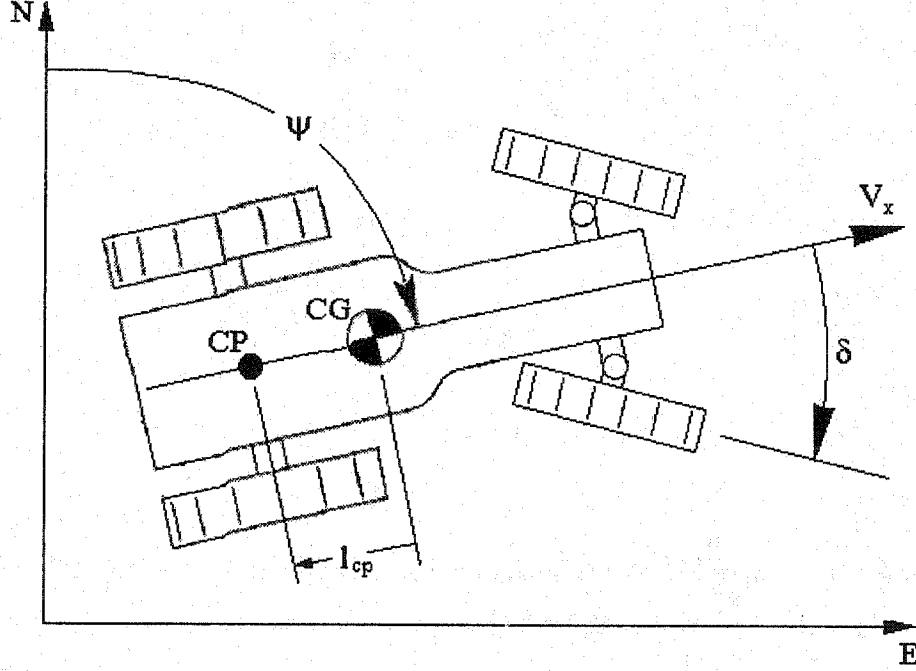


Figure 6.2 Schematic of a Tractor.

As was done previously, the lateral velocities at the CG of the vehicle will be neglected in the control and estimation algorithms used in this chapter. Under this assumption, the equations of motion which describe the off-road vehicle shown in Figure 6.2 can be divided into the forward and lateral dynamics shown in Equations (6.2) and (6.3).

$$\dot{N} = V_x \cos(\psi) + \dot{\psi} l_{cp} \sin(\psi) \quad (6.2)$$

$$\begin{aligned} \dot{E} &= V_x \sin(\psi) + \dot{\psi} l_{cp} \cos(\psi) \\ \ddot{\psi} &= -2\zeta\omega_n \dot{\psi} - \omega_n^2 \psi + K_R \omega_n^2 \delta \end{aligned} \quad (6.3)$$

$$\ddot{\delta} = \frac{1}{\tau_v} \dot{\delta} + \frac{K_v}{\tau_v} u$$

where:

$u$  = control input

$E$  = east position  
 $N$  = north position  
 $V_x$  = forward velocity  
 $\psi$  = heading  
 $\dot{\psi}$  = yaw rate  
 $\ddot{\psi}$  = yaw acceleration  
 $\delta$  = steer angle  
 $\dot{\delta}$  = steering slew rate

$K_R$ ,  $\omega_n$ ,  $\zeta$  are the tractor yaw dynamic parameters from the NYD model discussed in Chapter 2. The valve parameters,  $\tau_v$  and  $K_v$ , are given in Section 3.1.1.

## 6.2.1 Reconstructing an Estimate of Heading

Again, in this chapter there are no heading measurement from GPS. Therefore, an estimate of heading must be reconstructed from the given set of sensors. Equations (6.2-6.3) could be placed into one state matrix to estimate all of the necessary states for control of the tractor. However, the gyroscope would not specifically be used to help smooth the heading measurements. Therefore, a simple two state kinematic Kalman filter is first constructed to estimate the vehicle heading and yaw gyroscope bias. The filter uses the yaw gyroscope as an input and a rough estimate of vehicle course from consecutive GPS position measurements as a state measurement. Additionally, as discussed in Chapter 4, problems can occur when trying to estimate the gyroscope and steer angle biases in one estimator. Modeling the gyroscope bias as a first order Markov process with a time constant of 200 seconds results in the kinematic heading model:

$$\begin{bmatrix} \dot{\psi} \\ \dot{g}_{bias}^{yaw} \end{bmatrix} = \begin{bmatrix} 0 & -1 \\ 0 & -1/200 \end{bmatrix} \begin{bmatrix} \psi \\ g_{bias}^{yaw} \end{bmatrix} + \begin{bmatrix} 1 \\ 0 \end{bmatrix} \dot{\psi}_{gyro} + w_{yaw} \quad (6.4)$$

$$\psi_{vel} = \begin{bmatrix} 1 & 0 \end{bmatrix} \begin{bmatrix} \psi \\ g_{bias}^{yaw} \end{bmatrix} + v_{\psi}$$

where:  $v_{\psi}$  is the GPS velocity heading measurement noise with covariance  $0.01 \text{ rad}^2$   
 $w_{yaw}$  is a yaw process noise vector with covariance:

$$Q_w = \begin{bmatrix} 5 \times 10^{-6} \text{ rad}^2 & 0 \\ 0 & 1 \times 10^{-6} \frac{\text{rad}^2}{\text{s}^2} \end{bmatrix}$$

Initial values for the discrete heading process noise matrix ( $Q_w$ ) were obtained using the input sensor noise covariance and Equation (5.27). Values were then slightly modified, to give the desired filtering characteristics, resulting in the above  $Q_w$  matrix.

The Markov time constant of 200 seconds is the estimated time constant of the bias drift from an Allen Variance analysis of the Fiber Optic Gyroscope in [Gebre-Egziabher, 2001(a)]. The covariance of the process noise is determined from the gyroscope's sensor noise and bias drift properties. A linear Kalman filter is then applied to the above kinematic model to provide estimates of the vehicle heading and yaw gyroscope bias. The linear Kalman filter is comprised of a measurement update and time update [Stengel, 1994], which is performed at each time step ( $k$ ). The measurement update is described by:

$$\begin{aligned} L_k &= P_k C^T (C P_k C^T + R)^{-1} \\ \hat{x}_k &= X_k + L_k (y_{meas} - C \hat{x}_k) \\ P_k &= (I - L_k C) P_k \end{aligned} \quad (6.5)$$

where:  $L$  = Kalman Gain Vector  
 $P$  = State Estimation Covariance Matrix  
 $C$  = Observation Matrix  
 $R$  = Sensor Noise Matrix  
 $I$  = Identity Matrix  
 $x$  = State Estimate Vector  $\begin{bmatrix} \psi & g_b^{yaw} \end{bmatrix}^T$

The assumed measurement noise covariance (used in  $R$ ) on the heading measurement was  $0.01 \text{ rad}^2$ . This covariance value is higher than the GPS velocity-based heading measurement noise in order to include errors in the heading measurement induced by vehicle roll dynamics. The time update is described by:

$$\begin{aligned} \hat{x}_{k+1} &= \Phi \hat{x}_k + \Gamma u_k \\ P_{k+1} &= \Omega P_k \Omega^T + Q_w \end{aligned} \quad (6.6)$$

where:  $\Phi$  = discretized state matrix without the Markov time constant  
 $\Omega$  = discretized state matrix with the Markov time constant  
 $\Gamma$  = discretized input vector  
 $Q_w$  = discretized process noise covariance matrix

For the discrete estimator described by the model given in Equation (6.4),  $\Phi$  is found by discretizing the state matrix ( $A$ ) without the Markov time constant shown below:

$$A = \begin{bmatrix} 0 & -1 \\ 0 & 0 \end{bmatrix} \quad (6.7)$$

and  $\Gamma$  is the discretized input vector ( $B$ ).

$$B = [1 \ 0]^T \quad (6.8)$$

It is important to note that when propagating the states forward in the time update, the Markov time constant is not used in the state matrix ( $A$ ). The Markov time constant is only used to determine  $\Omega$ , which is used in propagating the state covariance matrix ( $P$ ). This is because in reality the actual input driving the gyroscope bias is not known, and therefore the “best guess” is that it remains constant during the time update.

The heading measurement can be estimated from the GPS velocity heading measurement (from a single GPS antenna, as in [Kornfeld, 1998] or in [Bevly, 2000(a)]) or from consecutive position measurements as shown in Equation (6.9).

$$\psi_{vel} = \tan^{-1} \left( \frac{V_{east}}{V_{north}} \right) = \tan^{-1} \left( \frac{E_k - E_{k-1}}{N_k - N_{k-1}} \right) \quad (6.9)$$

Because GPS velocity information is quite accurate (without any differential corrections) the heading measurement from the velocity vector is fairly accurate. However, the velocity measurements will include all extraneous velocities, including those induced by vehicle roll. Assuming that there are no changes in the side slip such that the difference between the vehicle heading and direction of travel remains the same, the gyroscope filters out this added noise in the heading measurement (and estimates the gyroscope bias) regardless of other model errors. Additionally, the gyroscope will be integrated in the time update step of the Kalman filter to produce heading estimates during a GPS outage.

Estimation of the heading from this separate filter was found to be much more accurate (than the heading estimate from one Kalman filter using the model given in Equations (6.2-6.3)) because it specifically uses the gyroscope measurements to smooth the noisy heading measurements.

Figure 6.3 shows the separate yaw bias estimation, as well as the steer angle measurement and the gyroscope measurements. This run is similar to the run in Figure 4.4, however now it can be seen that the yaw gyroscope bias is being estimated correctly, regardless of the steer angle offset.

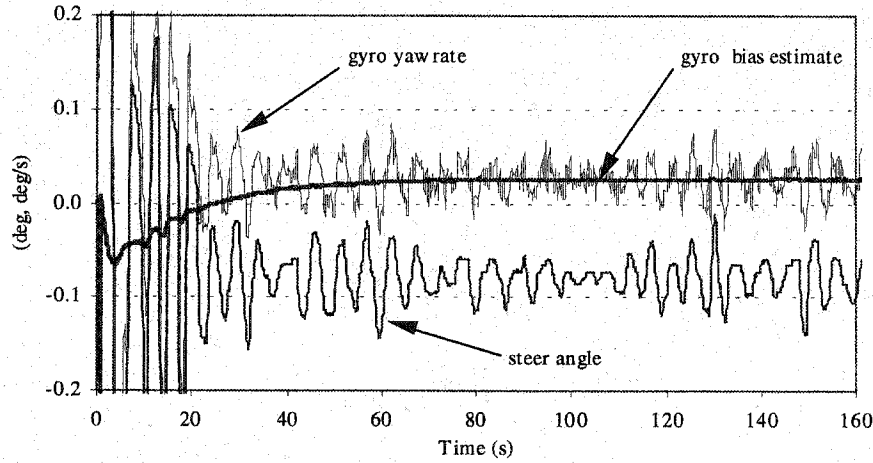


Figure 6.3 Separate Yaw Gyroscope Bias Estimation.

The use of a separate estimation technique allows for estimation of the steer angle bias as in Chapter 4. As mentioned previously, these two biases cannot be estimated together in one Kalman filter as it sometimes leads to instability in the estimator. Again, no compensation of the gyroscope yaw rate for non-zero roll and pitch was performed in this work.

## 6.2.2 Estimation of the Remaining Tractor States

The remaining tractor dynamics (given in Equations (6.2-6.3)) can be placed into the following state space structure:

$$\dot{X} = A(\psi)X + Bu + w_x \quad (6.10)$$

where:  $w_x$  = process noise vector (8x1) with covariances from Chapter 4 (Table 4.1)

and the remaining estimated states are  $\hat{X} = [\hat{E} \quad \hat{N} \quad \hat{V}_x \quad \hat{\psi} \quad \hat{\psi} \quad \hat{\delta} \quad \hat{\delta} \quad \hat{\delta}_b]^T$

The steer angle bias ( $\delta_b$ ) and velocity of the tractor are assumed to be slowly varying and modeled as being driven by random process noise with the same process noise covariances as the estimator in Chapter 4. Note that heading is not a state in Equation (6.10).

Because the vehicle heading is estimated in a separate filter and is not a state in Equation (6.10), the model described by Equation (6.10) is linear. Therefore the linear Kalman Filter given previously in Equations (6.5) and (6.6) can be used to propagate the estimates of the tractor states. The estimate of heading from the heading estimator given in Equation (6.4) must be fed into the state matrix (A) of the tractor dynamics model. For the estimator described by the model given in Equation (6.10),  $\Phi$  is determined by discretizing the state matrix (A):

$$A(\psi) = \begin{bmatrix} 0 & 0 & \cos(\psi) & l_{CP} \sin(\psi) & 0 & 0 & 0 & 0 \\ 0 & 0 & \sin(\psi) & l_{CP} \cos(\psi) & 0 & 0 & 0 & 0 \\ 0 & 0 & 0 & 0 & 0 & 0 & 0 & 0 \\ 0 & 0 & 0 & 0 & 1 & 0 & 0 & 0 \\ 0 & 0 & 0 & -\omega_n^2 & -2\xi\omega_n & K_R\omega_n^2 & 0 & 0 \\ 0 & 0 & 0 & 0 & 0 & 0 & 1 & 0 \\ 0 & 0 & 0 & 0 & 0 & 0 & -1/\tau_v & 0 \\ 0 & 0 & 0 & 0 & 0 & 0 & 0 & 0 \end{bmatrix} \quad (6.11)$$

and  $\Gamma$  is found by discretizing the input matrix (B):

$$B = \begin{bmatrix} 0 & 0 & 0 & 0 & 0 & 0 & K_v/\tau_v & 0 \end{bmatrix}^T \quad (6.12)$$

The observation matrix (C) is described by:

$$y_{\text{meas}} = Cx + v \quad (6.13)$$

where:  $y_{\text{meas}} = [E_{GPS} \quad N_{GPS} \quad \dot{\psi}_{\text{gyro}} - g_b^{yaw} \quad \delta_{\text{pot}}]^T$

$v$  = sensor noise vector (5x1) with covariances from Chapter 4 (Table 4.2);

$$C = \begin{bmatrix} 1 & 0 & 0 & 0 & 0 & 0 & 0 & 0 \\ 0 & 1 & 0 & 0 & 0 & 0 & 0 & 0 \\ 0 & 0 & 0 & 1 & 0 & 0 & 0 & 0 \\ 0 & 0 & 0 & 0 & 0 & 1 & 0 & 1 \end{bmatrix} \quad (6.14)$$

The estimator presented in Chapter 4 also estimated a slowly varying crab angle or heading bias due to lateral velocities. Since no heading measurement is used in this chapter it must be assumed that there is no heading bias and that the vehicle is headed along its forward velocity. This assumption is fine on flat terrain. However on largely sloped terrain, the tractor actually exhibits significant crab angles and the assumption is no longer valid [Bell, 1998]. Some type of compass or magnetometer could be used for a heading measurement, but these sensors generally have a bias associated with them making the crab angle indistinguishable from the heading sensor bias. The magnetometer



bias may be calibrated out *a priori*, as demonstrated in [Gebre-Egziabher, 2001(b)], and then used as a heading measurement. Additionally, the magnetometer's heading output is highly coupled to vehicle roll and pitch due to inclination and declination of Earth's magnetic field [Gebre-Egziabher, 2000]. A method for estimating the roll of a farm vehicle, which can also be used for estimating pitch, is developed in the preceding section. These roll and pitch estimates could then be used to correct the magnetometer outputs using the methods developed in [Gebre-Egziabher, 2000]. Even in circumstances with significant amounts of crab angle, a heading measurement is not absolutely necessary. As long as the crab angle is not changing faster than the bandwidth of the estimator in Section 6.2.1, the estimator will provide a good estimate of vehicle course or direction of travel. Ultimately it is the vehicle's course (and not actual heading) that is required for control of the tractor.

### 6.2.3 Reconstructing an Estimate of Roll

As discussed in Section 6.1, an estimate of vehicle roll is required to correct the GPS position measurement on the roof of the tractor. Without GPS attitude measurements, an estimate of the vehicle roll must be constructed in order to perform this correction. The roll motion of the vehicle occurs from terrain inputs (as described in Figure 6.1) as well as from vehicle dynamics coupled through the suspension. As a simplification, the coupling between the roll and vehicle dynamics is neglected in this work. Therefore, the roll states are modeled independently as shown in the roll model equation below.

$$\begin{bmatrix} \dot{\phi} \\ \ddot{\phi} \\ \dot{g}_b^{roll} \end{bmatrix} = \begin{bmatrix} 0 & 1 & 0 \\ 0 & 0 & 0 \\ 0 & 0 & 0 \end{bmatrix} \begin{bmatrix} \phi \\ \dot{\phi} \\ g_b^{roll} \end{bmatrix} + \begin{bmatrix} 0 & 0 \\ 1 & 0 \\ 0 & 1 \end{bmatrix} \begin{bmatrix} w_1 \\ w_2 \end{bmatrix} \quad (6.15)$$

$$\begin{bmatrix} \phi_{acc} \\ \dot{\phi}_{gyro} \end{bmatrix} = \begin{bmatrix} 1 & 0 & 0 \\ 0 & 1 & 1 \end{bmatrix} \begin{bmatrix} \phi \\ \dot{\phi} \\ g_b^{roll} \end{bmatrix}$$

where:

- $\phi$  = roll angle
- $\dot{\phi}$  = roll rate
- $g_b^{roll}$  = roll gyro bias
- $w_1$  &  $w_2$  are disturbance inputs

The roll states can now be estimated using the same Kalman filter described previously. However, the roll states are only driven by disturbances (i.e. process noise) because there is no commanded input. Therefore, good knowledge of the covariance of the disturbance inputs,  $w_1$  and  $w_2$ , is required to estimate the states correctly. However, since an estimate of the roll rate state is not required, Equation (6.15) can be rearranged to use the roll rate measurement from a gyroscope mounted in the roll axis as an input to a kinematic model shown in Equation (6.16).

$$\begin{bmatrix} \dot{\phi} \\ \dot{g}_b^{roll} \end{bmatrix} = \begin{bmatrix} 0 & -1 \\ 0 & 0 \end{bmatrix} \begin{bmatrix} \phi \\ g_b^{roll} \end{bmatrix} + \begin{bmatrix} 1 \\ 0 \end{bmatrix} \dot{\phi}_{gyro} + w_{roll}$$

$$\phi_{acc} = \begin{bmatrix} 1 & 0 \end{bmatrix} \begin{bmatrix} \phi \\ g_b^{roll} \end{bmatrix} + v_{acc}$$
(6.16)

where:  $v_{acc}$  is the roll measurement noise with covariance  $3 \times 10^{-4} \text{ rad}^2$   
 $w_{roll}$  is the roll measurement noise with covariance:

$$Q_w = \begin{bmatrix} 4 \times 10^{-6} \text{ rad}^2 & 0 \\ 0 & 1 \times 10^{-6} \frac{\text{rad}^2}{\text{s}^2} \end{bmatrix}$$

The Kalman filter described by Equations (6.5) and (6.6) can now be applied to the above kinematic model to provide estimates of the vehicle roll angle and roll gyroscope bias.

Figure 6.4 shows a spectral analysis of vehicle roll on a typical field (measured using GPS at 10 Hz) for a tractor traveling 2 m/s. As seen in the figure, the vehicle roll disturbance is mostly at low frequency, “rolling off” at around 0.12 Hz. A resonant peak can also be seen near 1 Hz. This is a high frequency ground disturbance acting on the cab of the vehicle. The low frequency nature of the vehicle roll precludes simply filtering GPS position measurements. If the roll disturbance was solely high frequency vibrations, the GPS antenna measurements at the roof of the vehicle could be filtered, since the tractor would be unable to track these high frequency lateral motions.

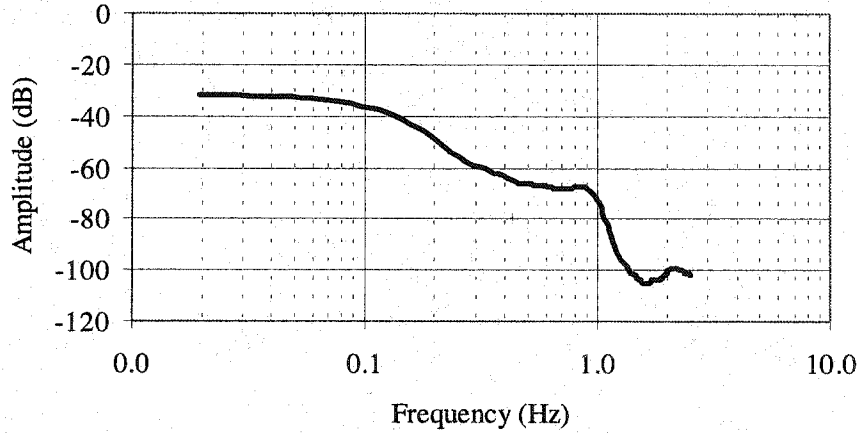


Figure 6.4 Spectral Analysis of Tractor Cab Roll (at 2 m/s).

However, the fact that the vehicle roll consists mostly of a low frequency content allows for the use of inexpensive accelerometers. Sensors such as accelerometers suffer from high frequency noise, but can be filtered to measure the frequency content seen in Figure 6.4. Because the roll disturbances are of such low frequency, the roll gyroscope does not add much more information to the filtered accelerometer. For this reason, only the accelerometer was used to measure roll for control of the tractor. The roll estimator (which uses the roll gyroscope) described in Equation (6.16) was only used for comparison to the accelerometer measurements. It was noticed that indeed the filtered roll accelerometer produced similar results to the full 2-state estimation model.

The accelerations measured from the accelerometer include roll as well as lateral acceleration created from vehicle yawing and side slip [Gillespie, 1992] as shown in Equation (6.17).

$$\ddot{y}_{meas} = -g_c \sin(\phi) + V_x \dot{\psi} + \dot{V}_y \quad (6.17)$$

where

$$\begin{aligned} \ddot{y}_{meas} &= \text{measurement from the accelerometer} \\ g_c &= \text{gravitational constant (9.81 m/s}^2\text{)} \\ \beta &= \text{vehicle side slip angle} \end{aligned}$$

Equation (6.17) assumes that the longitudinal velocity ( $V_x$ ) and yaw rate ( $\dot{\psi}$ ) are orthogonal. Because  $\dot{V}_y \ll V_x \dot{\psi}$ , lateral accelerations at the vehicle CG due to side slip

can be neglected. Therefore only corrections of the accelerometer measurement due to vehicle yaw rate are considered. The resulting corrected roll measurement is:

$$\phi_{meas} = \sin^{-1} \left( \frac{\ddot{y}_{meas} - V_x \dot{\psi}}{g} \right) \quad (6.18)$$

A simple first order digital low pass filter with a bandwidth of 0.12 Hz was used to filter the accelerometer measurements (at a sample rate of 5 Hz) as shown in Equation (6.19).

$$\frac{\phi(z)}{\phi_{meas}(z)} = \frac{0.85}{z - 0.85} \quad (6.19)$$

Although this cutoff frequency is filtering away the higher frequency roll seen in Figure 6.4 (at about 1 Hz), the tractor's control bandwidth is such that it could not track the high frequency lateral motion caused from this higher frequency roll. Therefore, no performance is lost by filtering the roll sensor at 0.12 Hz.

The GPS position measurements at the roof of the vehicle must be translated to the control point on the ground using the "lever arm" correction:

$$P_{CP} = T \times P_{lever-arm} + P_{meas} \quad (6.20)$$

Equation (6.20) represents the transformation (lever arm correction) from the GPS positions measured on the roof of the tractor in an East-North-Down coordinate system to the tractor control point (CP) on the ground. The transformation matrix ( $T$ ) for a yaw ( $\psi$ ), pitch ( $\theta$ ), roll( $\phi$ ) Euler angle sequence is defined by [Greenwood, 1988]:

$$T = \begin{bmatrix} \cos(\psi) \cos(\theta) & \cos(\psi) \sin(\theta) \sin(\phi) - \sin(\psi) \cos(\phi) & \cos(\psi) \sin(\theta) \cos(\phi) + \sin(\psi) \sin(\phi) \\ \sin(\psi) \cos(\theta) & \sin(\psi) \sin(\theta) \sin(\phi) + \cos(\psi) \cos(\phi) & \sin(\psi) \sin(\theta) \cos(\phi) - \cos(\psi) \sin(\phi) \\ -\sin(\theta) & \cos(\theta) \sin(\phi) & \cos(\theta) \cos(\phi) \end{bmatrix} \quad (6.21)$$

The antenna measuring the position of the tractor was located on the front right corner of the roof of the tractor cab. Therefore the lever arm vector ( $P_{lever-arm}$ ) from the position antenna to the CP (located on the ground between the rear axles for this chapter) is defined as:

$$P_{lever-arm} = \begin{bmatrix} x \\ y \\ z \end{bmatrix} = \begin{bmatrix} -1.61 \text{ m} \\ -0.57 \text{ m} \\ 3.06 \text{ m} \end{bmatrix} \quad (6.22)$$

As mentioned previously, pitch of the vehicle does not create lateral errors and therefore was not used in this chapter. Therefore, Equation (6.20) simplifies to (assuming zero pitch):

$$\begin{bmatrix} N \\ E \\ D \end{bmatrix}_{CP} = \begin{bmatrix} \cos(\psi) & -\sin(\psi)\cos(\phi) & \sin(\psi)\sin(\phi) \\ \sin(\psi) & \cos(\psi)\cos(\phi) & -\cos(\psi)\sin(\phi) \\ 0 & \sin(\phi) & \cos(\phi) \end{bmatrix} P_{lever-arm} + \begin{bmatrix} N \\ E \\ D \end{bmatrix}_{meas} \quad (6.23)$$

However, if there was a concern over longitudinal errors, the same approach of low pass filtering an accelerometer could be applied to the pitch axis (since the frequency component of pitch motion is nearly identical to that of roll).

## 6.3 Simulation Results

The same linear quadratic regulator (LQR) presented in Chapter 3 was used to control the lateral error ( $y$ ) of the tractor with the control point at the CG of the vehicle ( $l_{cp} = 0$ ). The control algorithm is actually independent of whether or not GPS or PINS attitude measurements are used. This is due to the fact that the control algorithm only uses the estimates of specific states, and not the measurements themselves (assuming that the estimator can produce the required state estimates given its measurements). This flexibility allows for optimization of the GPS/INS integration without affecting the control algorithm of the tractor.

A simulation study was done to provide a comparison of the (closed loop) line tracking at 2 m/s of various sensor sets. Realistic sensor noises (described in the next section and given in Table 6.2) were used. A combination of low frequency vehicle roll ( $\pm 5$  deg at 0.1 Hz) as well as white roll measurement noise was added to the vehicle. The roll measurement noise is due to actual roll noise as well as roll measurement noise. The following five cases were simulated:

- Case I-GPS Attitude
- Case II-No GPS Attitude (i.e., no roll measurement)
- Case III-No GPS Attitude with a Gyroscope
- Case IV-Noisy Roll Measurement
- Case V-Noisy Roll Measurement with a Gyroscope

Standard deviations of the heading estimate errors are shown in Figure 6.5a and the standard deviation of the resulting lateral position errors are shown in Figure 6.5b. A summary of the errors for the various cases are also presented in Table 6.1.

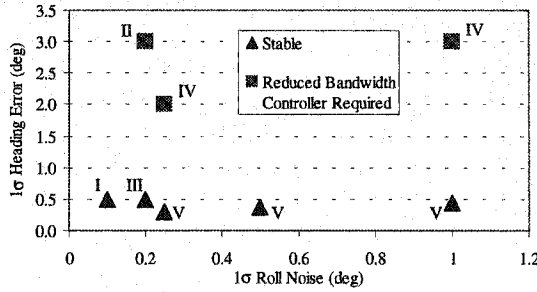


Figure 6.5a Heading Error vs. Roll Noise for Various Sensor Sets.

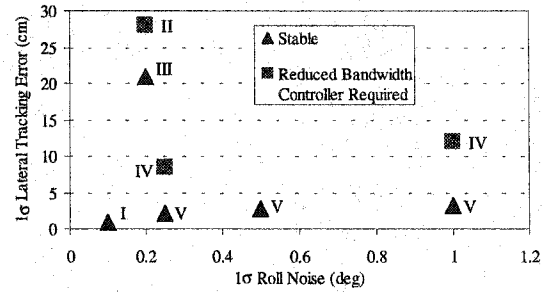


Figure 6.5b Lateral Tracking Error vs. Roll Noise for Various Sensor Sets.

Table 6.1 Simulation Study Results: Heading Estimation and Lateral Errors ( $1\sigma$ ) for Various Sensor Sets.

Case	I	II	III	IV	IV	V	V	V
$1\sigma$ Roll Noise (deg)	0.1	0.2	0.2	0.25	1.0	0.25	0.5	1.0
$\sigma(\hat{\psi}_{\text{error}})$ (deg)	0.5	3.0*	0.5	2.0*	3.0*	0.3	0.37	0.45
$\sigma(y_{\text{error}})$ (cm)	1.0	28.0*	21.0	8.5*	12.0*	2.1	2.7	3.2

Asterisks are given next to values where the system was unstable for the LQR control weights given in the previous section. Therefore results for these cases are for a controller with reduced penalties and a reduced bandwidth. It is important to note that the decrease in controller bandwidth ignores the roll disturbances at the cost of reducing the ability to reject “real” position disturbances. It is evident by the results in the table, that the gyroscope’s ability to provide a better estimation of heading also provides an increase in the lateral tracking performance (even with noisy roll measurements). It is important to note that Case IV will exhibit the same performance as a system using one regular state estimator. This is because the gyroscope (in a regular estimator) would not specifically filter the noisy heading measurement.

## 6.4 Experimental Results

The experimental validation of the PINS attitude for control of the tractor was again performed on the John Deere 8400 tractor discussed in Appendix A. A KVH fiber optic gyroscope (FOG) was used for sensing yaw rates. Although off-road vehicles are subject to large amounts of mechanical vibrations, the non-mechanical FOG can provide excellent yaw sensing under these conditions. The yaw gyroscope provides the ability to estimate heading and yaw rates more accurately, therefore increasing the control performance of the vehicle. The increased estimation of yaw rates additionally helps the roll estimate due to the yaw correction described in Equation (6.18). A Humphrey's accelerometer and a Systron Donner Gyroscope were used in the roll axis of the vehicle.

The majority of the experimental runs were performed at about 2 m/s (4 mph) along straight-line trajectories. This is a typical speed for most farm tillage operations. GPS attitude corrected position measurements were recorded for performance analysis of the PINS control. Data was collected to compare the errors from GPS attitude measurements, GPS position based attitude measurements, and PINS measurements. A list of the sensor noises is shown in Table 6.2. The noise associated with the single antenna velocity and heading estimate is dependent on vehicle speed. The values listed below are typical for speeds ranging between 2-3 m/s (4-6 mph). It is important to note that most INS sensors have biases that are usually not constant over time and temperature, and therefore must be calibrated. It is also important to note that the static sensor noise on the accelerometer can be misleading. The actual accelerometer noise will be much higher due to the fact that the accelerometer is sensitive to high frequency accelerations and vibration noise, creating the need to filter the accelerometer. The critical value of concern is the roll measurement noise after sampling and filtering of the accelerometer.

Table 6.2 Static Sensor Noises ( $1\sigma$ ).

State	GPS		INS	
$\psi$ (deg)	Multiple Antenna	0.1	Honeywell Magnetometer	0.60
	Single Antenna (Equation (6.9) @ $V_x \sim 2\text{m/s}$ )	2.0		
$\dot{\psi}$ (deg/s)	Multiple Antenna	1.0	KVH FOG	0.44
$V_x$ (m/sec)	Single Antenna	0.03	Doppler Radar	0.12
$\phi$ (deg)	Multiple Antenna	0.1	Humphrey Accelerometer	0.04
$\dot{\phi}$ (deg/s)	Multiple Antenna	1.0	Systron Donner Rate Gyro	0.60

Figure 6.6 shows a plot of GPS roll measurements and the measurements from the accelerometer for a controlled run along a straight line in a fairly level field at 2 m/s. The filtered accelerometer is then compared to the GPS roll measurements along with the difference in the two measurements in Figure 6.7. It is important to notice that the roll measurement error for the filtered accelerometer is below the 0.4 deg threshold required to utilize the DGPS position accuracy as mentioned previously [Bell, 1999].

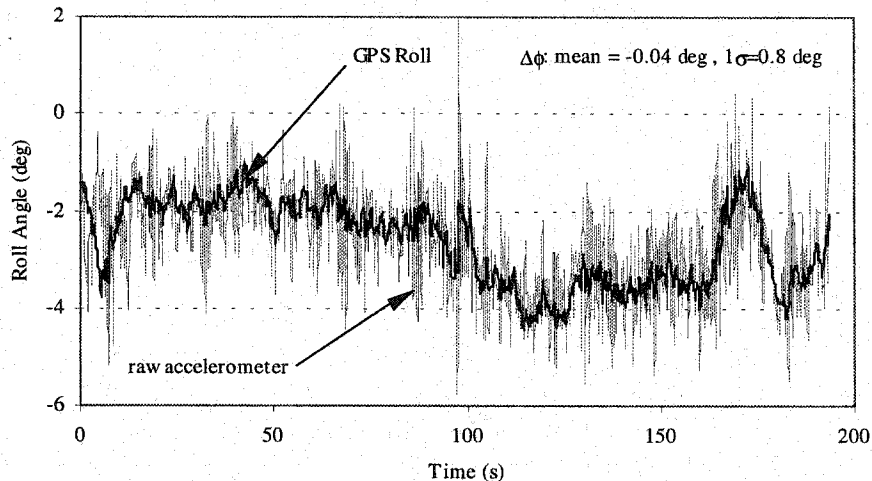


Figure 6.6 Accelerometer Roll and Roll from GPS.



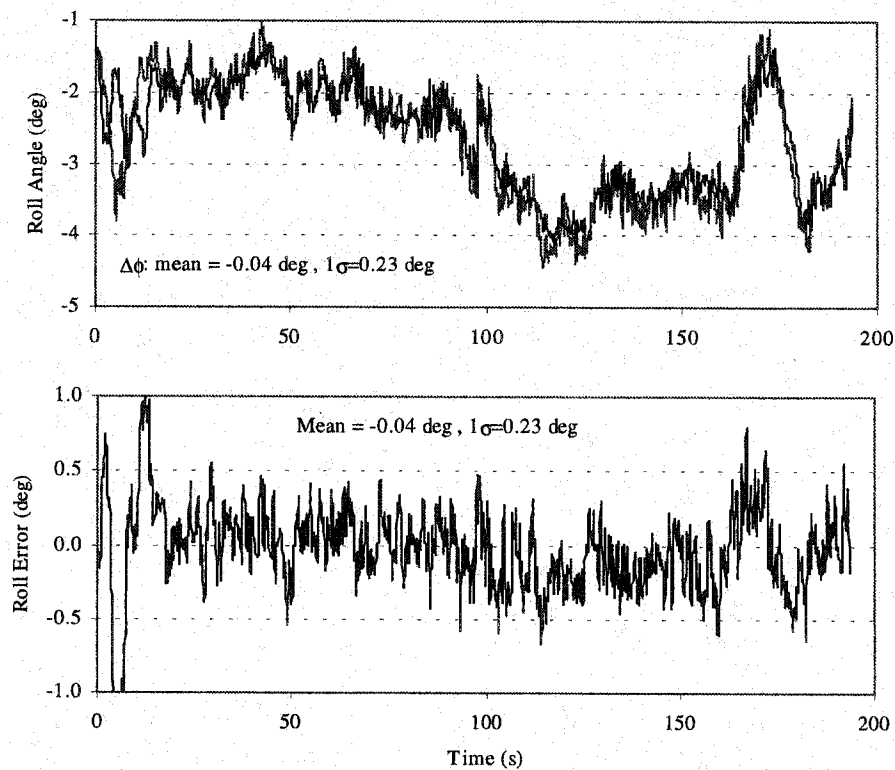


Figure 6.7 Filtered Accelerometer Roll, GPS Roll, and Their Difference.

Figure 6.8 shows the lateral error for straight line tracking on a fairly level field. The errors are calculated using the GPS attitude measurements to provide the “true” position. Figure 6.9 shows the heading estimation for the step response. The top portion of the figure shows the noisy velocity heading as well as the GPS attitude heading. The bottom portion of the figure shows the estimated heading using a Kalman filter from the model given in Equation (6.4). As can be seen in Figure 6.9, the heading estimator is providing a fairly accurate estimate of the vehicle heading in the presence of large heading noise from the velocity vector of one GPS antenna. This shows the ability of the gyroscope to help smooth the noisy heading measurements which led to the instabilities for Case II and Case IV of the simulation in the previous section. The small limit cycle observed in the vehicle heading is due to unmodeled non-linearities including, hydraulics, actuator dead band and linkage misalignments in the steering mechanism.

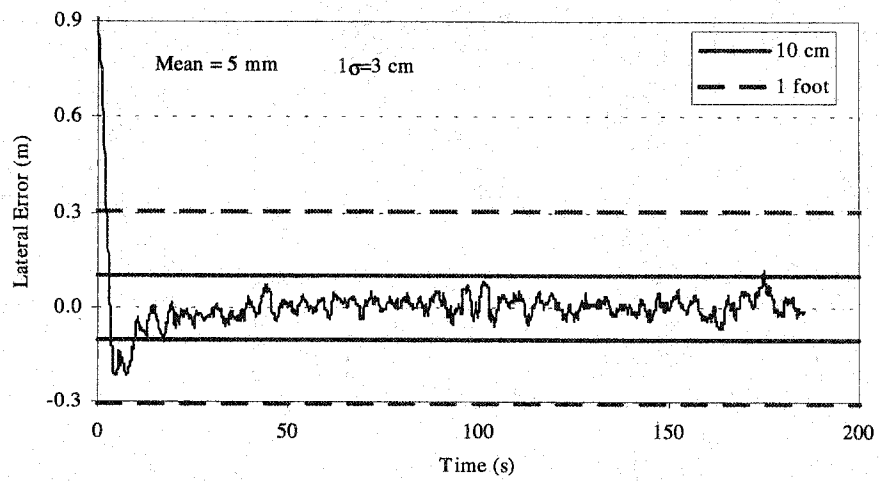


Figure 6.8 Experimental Step Response Without GPS Attitude Measurements.

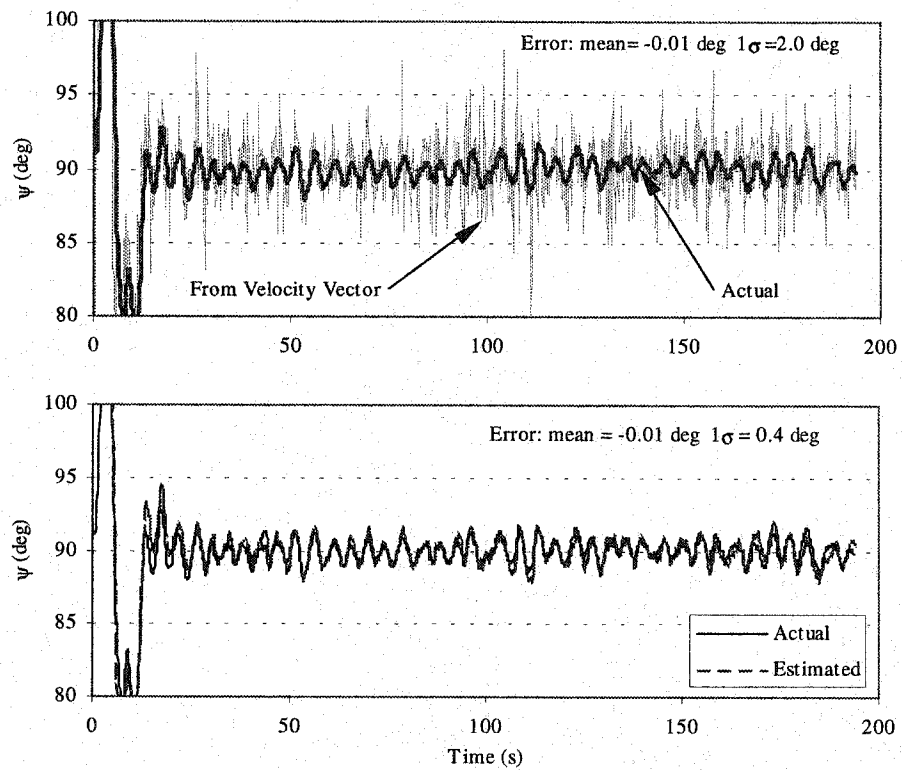


Figure 6.9 Heading Estimation for the Experimental Step Response.

Figure 6.10 shows an experimental run controlling the tractor in a field. The initial errors in Figures 6.8 and 6.10 are from the initial line acquisition. Additionally, Figure 6.11 shows the actual and estimated heading and Figure 6.12 shows the heading errors for the run done in Figure 6.10.

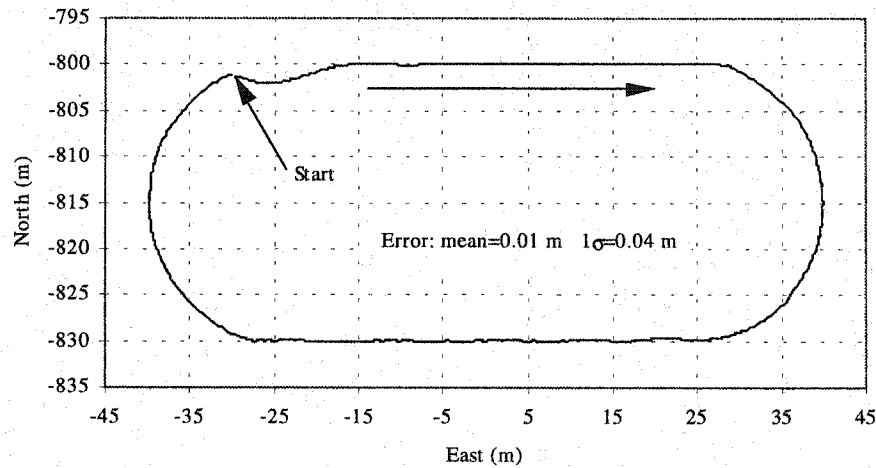


Figure 6.10 Control of the Tractor in a Field.

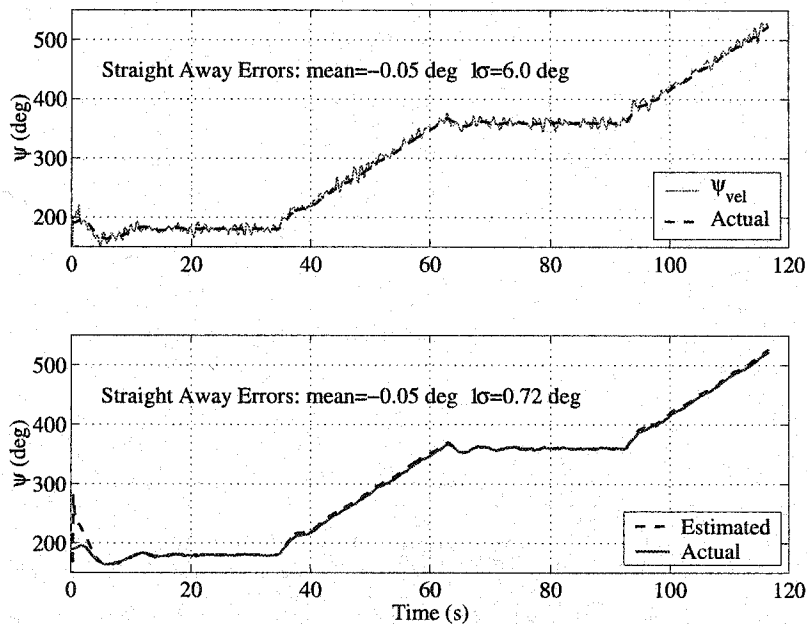


Figure 6.11 Heading Estimation for the Field Run.

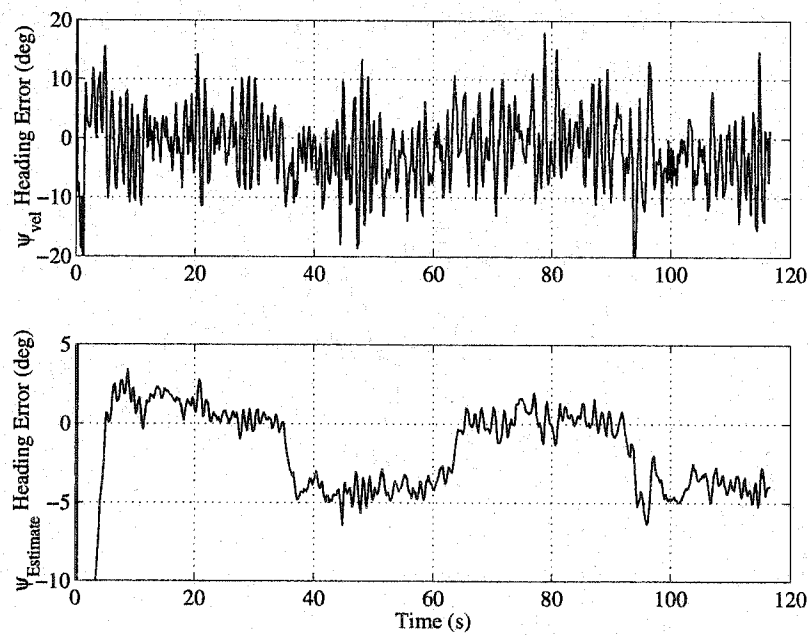


Figure 6.12 Heading Errors and Heading Estimate Errors for the Field Run (Note the Change in Axes).

Table 6.3 presents a comparison of the attitude systems for the control of the tractor over several different runs tracking a line for approximately 120 m at 2 m/s. All errors are with reference to GPS positions corrected using GPS attitude measurements. It is important to note that this reference has 2-3 cm of error ( $1\sigma$ ). The mean and standard deviation for the “no lever arm” case will be highly dependent on the amount of roll and change in roll over the field. All of the runs occurred on fairly level terrain with less than  $\pm 5$  deg of roll and agree quite well with the simulation results presented in Table 6.1

Table 6.3 Comparison of Attitude Systems for Control of the Tractor.

	Tractor Tracking Errors	
	Mean (m)	$1\sigma$ (m)
No Lever Arm Correction	0.10	0.12
PINS Only	0.007	0.0315
GPS Attitude	0.001	0.0234

## 6.5 Conclusions

This chapter has shown that inertial sensors, integrated with a single GPS receiver can provide the attitude accuracy to perform cm-level control of a farm tractor. The PINS controlled tractor is shown to produce attitude estimates nearly comparable to the attitude measurements obtained from a 4-antenna GPS solution. Results show that the roll characteristics of the tractor allow an inexpensive accelerometer to be filtered in order to provide roll measurements near the accuracy of the GPS attitude system. Finally, results show that performance of the PINS controlled tractor is comparable to that of a tractor using GPS attitude. It was also shown that a simple separate bias estimation technique could estimate the yaw gyroscope bias in the presence of a steer angle bias as well as provide accurate heading estimates of the vehicle.

Special care was taken to insure that the accelerometer biases were calibrated before experiments. It is known that most INS sensors have bias drifts associated with them (although there are certain types of inclinometers that have very good bias stability). For this reason, a solely INS attitude solution may not be practical for providing robust cm level accuracy over all conditions. However, this chapter has shown that the inertial sensors can provide the attitude accuracy to perform cm-level control of a farm tractor. Therefore, the PINS solution may provide a good back up sensor solution, where the INS biases can be calibrated using GPS attitude measurements similar to the methodology discussed in Chapter 4. In practice, some type of fusion of the GPS attitude and inertial solutions will most likely be used. This type of redundancy will increase the robustness of the system to sensor failures.

## Chapter 7

# Towed Implement Control

This chapter explores the use of a simple kinematic implement model, and carrier-phase Differential GPS measurements ( $1\sigma=2$  cm) on both the tractor and towed implement to directly control the position of the implement. This control is performed through the steering actuation of the tractor. A simple analytical model is developed for the tractor/implement combination. The kinematic model is linearized, allowing the parameters of the model to be identified using system identification techniques [Ljung, 1987]. The linearization of the model also allows state-space control and estimation techniques to be applied. A controller is then designed and implemented on the experimental system to control the position of the implement on a given path across the field. Full state feedback (requiring 7 states) is used to control the implement. An LQR algorithm is used to produce the feedback gains for the controller and an Extended Kalman Filter (EKF) is used to estimate all of the states required for the full state feedback algorithm. The model is validated with experimental data using carrier-phase Differential GPS position on the tractor as well as on the implement. The linearization of the tractor-implement model is validated through an open loop simulation as well as through a series of line tracking and step response experiments on a John Deere tractor with a chisel plow. Initial experimental results demonstrate that a linear compensator can accurately control the towed implement to within 10 cm of the desired trajectory.

## 7.1 Tractor-Implement Model

Figure 7.1 shows a schematic of the tractor pulling a towed implement. The implement's point of zero lateral velocity (ZLV) as well as the implement control point (cp) are shown in the figure. The ZLV is the point on the implement where the lateral velocity is equal to zero, stemming from the use of a kinematic model to describe the implement. The control point defines the location of the GPS positioning antenna on the implement, as well as the implement position ( $e_b$ ,  $n_I$ ), in this thesis. The position, yaw, and steering dynamics of the tractor have been discussed in previous chapters.

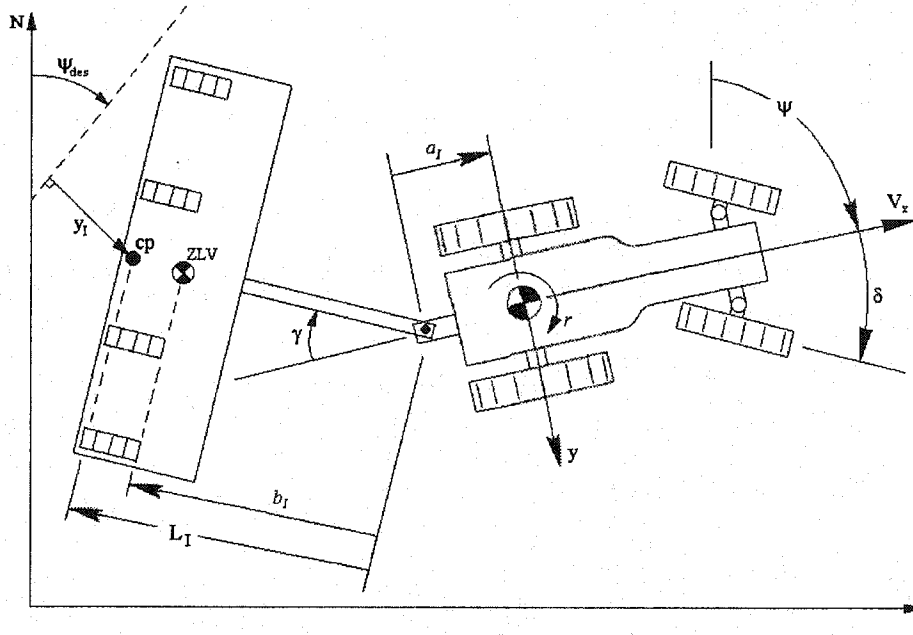


Figure 7.1 Schematic of a Farm Tractor and Towed Implement Combination.

A kinematic model of the implement can be used to describe the relationship between tractor velocity ( $V_x$ ) and yaw rate ( $r$ ) to implement angle as given in Equation (7.1).

$$\dot{\gamma} = -r \left[ 1 + \frac{a_I}{b_I} \cos(\gamma) \right] - \frac{V_x}{b_I} \sin(\gamma) \quad (7.1)$$

The above model is derived by simply looking at how tractor velocity and yaw rates translate into velocities at the tow pin (as discussed in Section C.1). The resulting tow pin velocities can then be used to determine the rotational velocity of the implement assuming zero lateral velocity at the ZLV point. Linearizing Equation (7.1) around small

implement angles and placing it into a transfer function from tractor yaw rate ( $r$ ) to implement angle results in:

$$\frac{\gamma(s)}{r(s)} = \frac{-(1 + \frac{a_I}{b_I})}{s + \frac{v_x}{b_I}} = \frac{-K_I}{s + \omega_I} \quad (7.2)$$

The resulting linear model is a simple first order lag from tractor yaw rate to implement angle. The parameters in Equation 7.2 were identified using a system identification approach [Ljung, 1987] similar to the approach taken to identify the yaw dynamics of the tractor in Chapter 2. The tractor was manually driven around at various speeds while inducing yaw rates to produce various implement angles.

Figure 7.2 shows how the identified values vary with forward velocity with the implement down as well as with the implement up. A least squares best fit of the points in Figure 7.2 allows for identification of the variables  $a_I$  and  $b_I$  in Equation 7.2 for the implement down (solid line) as well as the implement up (dashed line). The results of the least squares fit along with the physically measured quantities of  $a_I$  and  $b_I$  are given in Table 7.1. It is interesting to notice that the position of the implement's ZLV point (the point with zero lateral velocity) moves forward when the implement is in the ground. It makes intuitive sense that the implement's blades "plowing into the ground" change the rotation point of the implement. Therefore, for the physical measurements of  $a_I$  and  $b_I$ , the ZLV point was assumed to be at the implement's axle (tires) when the implement was up and at the midpoint of the plow blades when the implement was down.

Table 7.1 Implement Model Parameters.

Parameter	System Identified	Measured
$a_I$	1.16 m	1.14 m
$b_I$ (implement down)	4.42 m	5.0 m
$b_I$ (implement up)	5.63 m	5.8 m



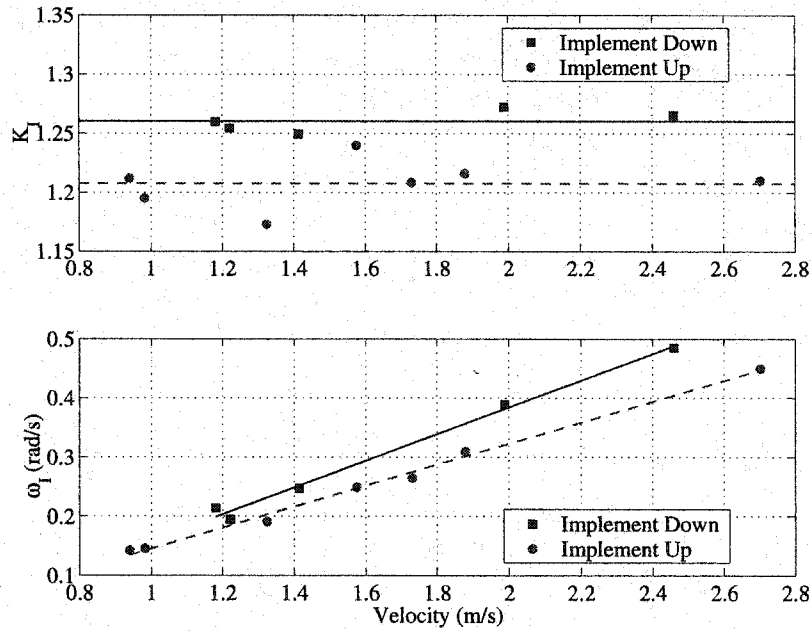


Figure 7.2 Implement Model Parameters vs. Velocity for the Implement Down (Solid) and Implement Up (Dashed).

The best fits for the model parameters shown in Figure 7.2 are used to validate the model in Figure 7.3. Figure 7.3 shows the vehicle velocity, yaw rate and implement angle (calculated from the inverse kinematics given the tractor position and heading and the implement position as shown in Appendix C) as well as the implement angle from the linear model in Equation 7.2. Recall that the model has been linearized using small angle approximations (which generally holds for angles less than 20 deg). As seen in the figure, the linearized model fits the actual data fairly well for angles less than 30 deg. The error between the model and actual angles due to the linearization can also be seen in the regions of implement angles above 30 deg. However, most implement operations should maintain implement angles of less than 30 deg such that the linearization is valid for control of the implement.

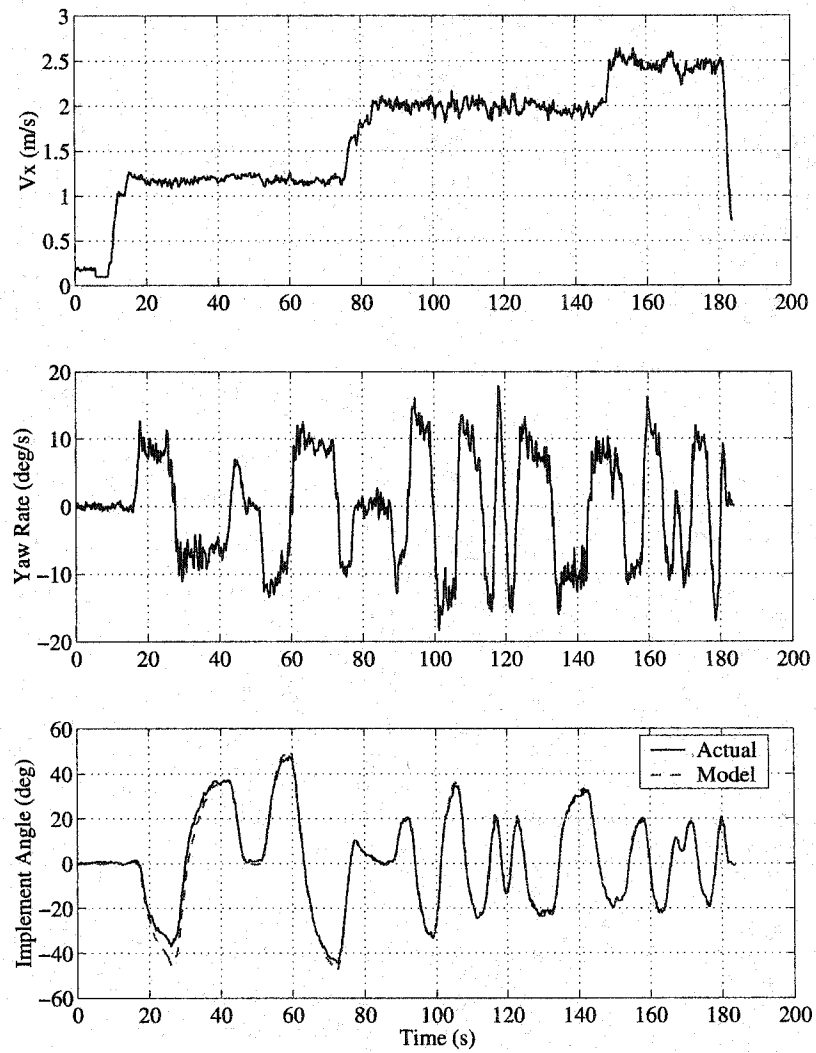


Figure 7.3 Implement Model Validation.

Figure 7.4 shows the open loop roots of the tractor-implement combination. Six of the roots are the same as the roots of the tractor system discussed in Chapter 3. The implement adds one additional real pole at about -0.4 rad/sec.

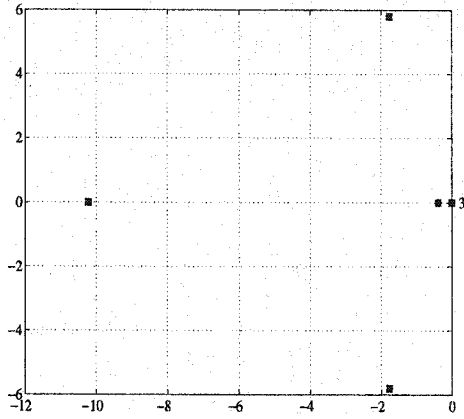


Figure 7.4a Continuous Open Loop Poles of the Tractor-Implement Combination.

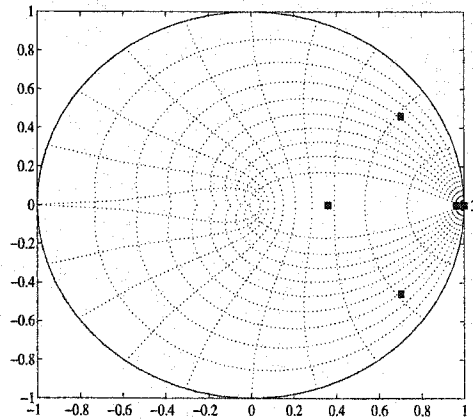


Figure 7.4b Discrete Open Loop Poles of the Tractor-Implement Combination (Ts=0.1 sec).

## 7.2 Implement Control Algorithm

A linear quadratic regulator (LQR) was used to control the lateral error ( $y_I$ ) of the implement (as opposed to the lateral error of the tractor as in Chapter 3). Setting the control point along the center line of the implement at a distance  $L_I$  from the tow pin (as shown in the schematic in Figure 7.1) and assuming small heading errors and implement angle, the lateral dynamics of the implement are described by:

$$\dot{y}_I = V_x \psi_{err} - L_I \dot{\gamma} - (a_I + L_I) \ddot{\psi} \quad (7.3)$$

where  $y_I$  is the lateral position of the implement with respect to the tracking line as shown in Figure 7.5 and  $\psi_{err}$  is the difference between the actual and desired heading as given in Equation (7.9). The derivation of Equation (7.3) is given in Section C.2 of the Appendices.

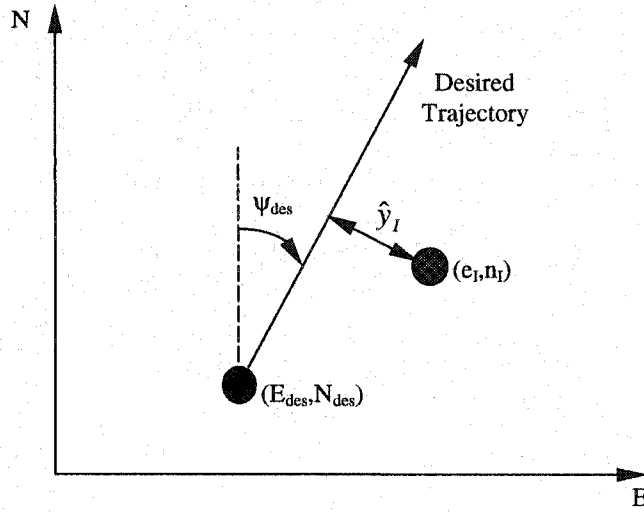


Figure 7.5 Schematic of a Desired Implement Trajectory.

Rewriting Equation (7.2) into the form:

$$\dot{\gamma} = -K_I \psi - \omega_I \gamma \quad (7.4)$$

The remaining dynamics necessary for full state feedback control are the tractor yaw dynamics (developed in Chapter 2) and the steering dynamics (given in Chapter 3). Rewriting the yaw dynamics from Equation (2.13) yields

$$\ddot{\psi} = -2\zeta\omega_n\dot{\psi} - \omega_n^2\psi + K_R\omega_n^2\delta \quad (7.5)$$

and rewriting the steering dynamics given in Chapter 3 yields

$$\ddot{\delta} = \frac{-1}{\tau_v}\dot{\delta} + \frac{K_v}{\tau_v}u \quad (7.6)$$

Equations (7.3-7.6) must be placed into the state space form shown in Equation (7.7) for the lateral control states ( $X_c$ ):

$$\dot{X}_c = A_c X_c + B_c u \quad (7.7)$$

The linear lateral dynamics can then be used to calculate the LQR control gains for the control law:

$$u = -K_c X_c \quad (7.8)$$

where:  $X_c = \begin{bmatrix} \hat{y}_I & \hat{\gamma} & \hat{\psi}_{err} & \hat{\psi} & \dot{\hat{\psi}} & \hat{\delta} & \dot{\hat{\delta}} \end{bmatrix}$

(Note: The ^ denotes estimates of the states.) Methods for calculating  $\hat{y}_l$  and  $\hat{\psi}_{err}$  are given below. All other estimates come from the Extended Kalman Filter estimation method described in the next section. The heading error is simply the difference in the desired and actual heading.

$$\hat{\psi}_{err} = \hat{\psi} - \hat{\psi}_{des} \quad (7.9)$$

The lateral error of the implement (shown previously in Figure 7.5) is the distance of the implement control point to the desired line and can be found by:

$$\hat{y}_l = (\hat{e}_l - E_{des})\cos(\psi_{des}) - (\hat{n}_l - N_{des})\sin(\psi_{des}) \quad (7.10)$$

The LQR compensator gain vector ( $K_c$ ) was solved at each time step (by solving the Riccati equation in real time) using the following control state weighting matrix ( $Q_x$ ) and control input weighting value ( $R_u$ ) as described in [Stengel, 1994]:

$$\begin{aligned} Q_x &= \text{diag}[Q_y \quad Q_\gamma \quad Q_\psi \quad Q_\psi \quad Q_\psi \quad Q_\delta \quad Q_\delta] \\ &= \text{diag}[1 \quad 0 \quad 0 \quad 0 \quad 0 \quad 1 \quad 0] \\ R_u &= 0.1 \end{aligned} \quad (7.11)$$

The above weighting matrices results in a control vector gain ( $K_c$ ) at 2 m/s of:

$$K_c = [2.69 \quad -13.81 \quad 23.14 \quad 0.79 \quad 0.20 \quad 4.57 \quad 0.42]$$

Placing weight on the steer angle state increases the damping in the closed loop system by penalizing the amount of steer angle allowable. The above compensator results in a closed loop bandwidth of 0.5 rad/sec dominated by the complex root pair shown in Figure 7.6.

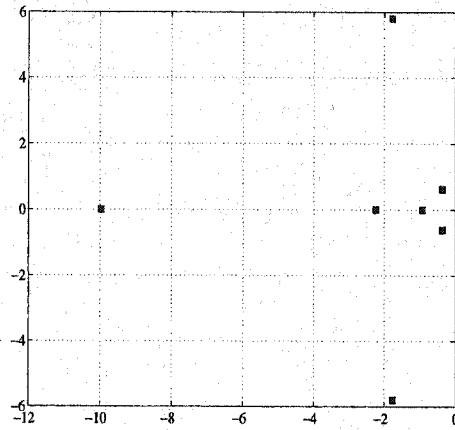


Figure 7.6a Continuous Closed-Loop Poles of the Tractor-Implement Combination.

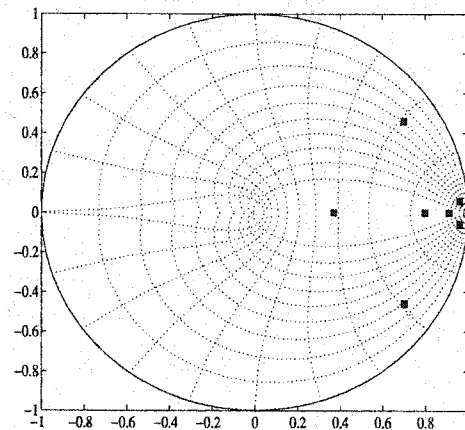


Figure 7.6b Discrete Closed-Loop Poles of the Tractor-Implement Combination ( $T_s=0.1$  sec).

In this thesis the tractor's yaw dynamic model developed in Chapter 2 is assumed to remain unchanged with the addition of the implement. Because the implement is towed, the implement should exert little lateral force on the tractor (for small implement angles). Several yaw dynamic identification runs (as was done in Chapter 2) for the tractor were taken with the implement up and down. These identified data runs can be seen in Figure 7.7 along with the NYD model from Chapter 2. The tractor yaw dynamics exhibit a very similar behavior with the towed implement to that seen in Chapter 2 (with no implement). However the natural frequency has decreased slightly due to the implement. Increasing the mass of the tractor or front tire relaxation length will cause the natural frequency of the analytical FTR model to decrease. However, the FTR model will not match the small amount of added damping seen in the tractor yaw dynamics with the implement. Although the tractor model has changed slightly, the implement's closed loop bandwidth of 0.5 rad/s allows the use of the same NYD model. Additionally, because the closed loop bandwidth of the controlled system is considerably below the yaw dynamics of the tractor, it may be possible to simplify the controller using the kinematic yaw rate model of the tractor shown in Equation (7.12).

$$r = \frac{V_x}{L} \delta \quad (7.12)$$

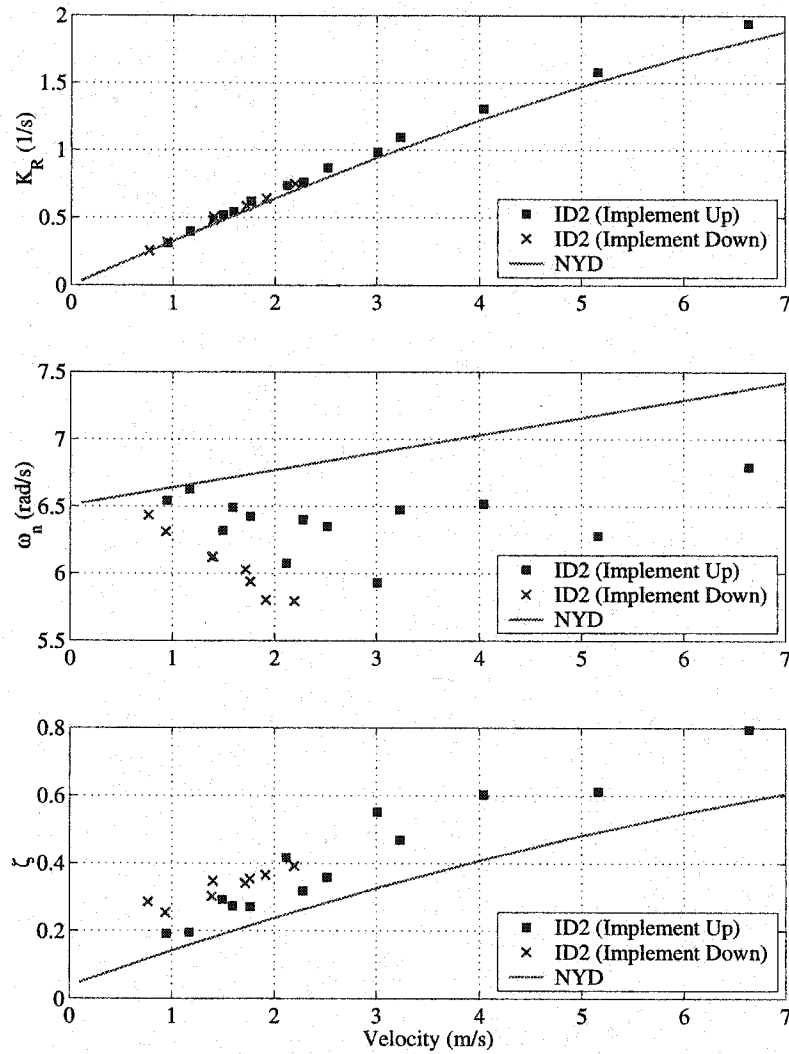


Figure 7.7 Identification of the Second Order Yaw Dynamic Model of the Tractor with a Towed Implement.

### 7.3 Implement Estimation Algorithm

The dynamics that describe the tractor implement are given in Equations (7.3-7.6). The tractor position dynamics are described by (from Equation (4.1) with  $l_{CP}=0$  and neglecting lateral velocities ( $V_y$ ) at the CG):

$$\begin{aligned}\dot{E}_T &= V_x \sin(\psi) \\ \dot{N}_T &= V_x \cos(\psi)\end{aligned}\tag{7.13}$$

The tractor yaw dynamics and steering dynamics were given in Equation (7.5) and Equation (7.6), respectively. The implement position dynamics (at the cp) are described by:

$$\begin{aligned}\dot{e}_I &= \dot{E}_T - (L_I \dot{\gamma} + L_I \dot{\psi}) \cos(\gamma + \psi) - a_I \dot{\psi} \cos(\psi) \\ \dot{n}_I &= \dot{N}_T + (L_I \dot{\gamma} + L_I \dot{\psi}) \sin(\gamma + \psi) + a_I \dot{\psi} \sin(\psi)\end{aligned}\tag{7.14}$$

The implement position dynamics can be derived directly from the velocity at the control point or by taking the time derivative of the implement position kinematics as shown in Section C.3. Substituting Equations (7.1) and (7.13) into Equation (7.14) results in:

$$\begin{aligned}\dot{e}_I &= V_x \sin(\psi) + \left[ \frac{L_I}{b_I} a_I \dot{\psi} \cos(\gamma) + \frac{L_I}{b_I} V_x \sin(\gamma) \right] \cos(\gamma + \psi) - a_I \dot{\psi} \cos(\psi) \\ \dot{n}_I &= V_x \cos(\psi) - \left[ \frac{L_I}{b_I} a_I \dot{\psi} \cos(\gamma) + \frac{L_I}{b_I} V_x \sin(\gamma) \right] \sin(\gamma + \psi) + a_I \dot{\psi} \sin(\psi)\end{aligned}\tag{7.15}$$

There are 16 states listed in Table 7.2 which must be estimated in order to accurately control the implement. Several of the states are needed for full state feedback as discussed later in Section 7.4. Ten of the states come from the dynamics of the tractor-implement combination given in Equations (7.4-7.6, 7.13, and 7.15). The remaining six states are velocity and five biases estimated in order to improve the accuracy of the control architecture.



Table 7.2 Estimated States for Towed Implement Control.

Tractor	Implement
$\hat{x}_T = [\hat{E}_T \quad \hat{N}_T \quad \hat{V}_x \quad \hat{\psi} \quad \hat{\dot{\psi}} \quad \hat{\ddot{\psi}} \quad \hat{\psi}_b \quad \hat{\delta} \quad \hat{\dot{\delta}} \quad \hat{\delta}_b \quad \hat{g}_b \quad \hat{r}_b]^T$ $E$ = tractor east position $N$ = tractor north position $V_x$ = forward velocity $\psi$ = heading $\dot{\psi}$ = yaw rate $\ddot{\psi}$ = yaw acceleration $\psi_b$ = heading bias or "crab angle" $\delta$ = steer angle $\dot{\delta}$ = steering slew rate $\delta_b$ = steer angle bias $g_b$ = gyro bias $r_b$ = radar bias	$\hat{x}_I = [\hat{e}_I \quad \hat{n}_I \quad \hat{\gamma} \quad \hat{\gamma}_b]^T$ $e$ = east position $n$ = north position $\gamma$ = angle $\gamma_b$ = angle bias

A cascaded estimator very similar to the estimator described in Chapter 4 was used for estimating all of the states needed for accurate implement control. The dead-reckoning estimator, given in Chapter 4, and used to estimate the tractor states, remains unchanged. The estimated states from the dead reckoning estimator are:

$$\hat{X}_1 = [\hat{E}_T \quad \hat{N}_T \quad \hat{r}_b \quad \hat{\psi} \quad \hat{g}_b \quad \hat{\psi}_b]^T$$

The remaining dynamics used to estimate the states necessary for control are the tractor yaw dynamics (7.5), the steering dynamics (7.6), implement position dynamics (7.15), and the implement angle dynamics (7.1). This leaves the remaining states to be estimated in the second estimator.

$$\hat{X}_2 = [\hat{\dot{\psi}} \quad \hat{\ddot{\psi}} \quad \hat{V}_x \quad \hat{\delta} \quad \hat{\dot{\delta}} \quad \hat{\delta}_b \quad \hat{e}_I \quad \hat{n}_I \quad \hat{\gamma} \quad \hat{\gamma}_b]^T$$

Because the dynamics described in Equations (7.1), (7.5), (7.6) and (7.15) are non-linear, they must be linearized about an operating point at each time step in order to place the dynamics in the form shown in Equation (7.7). This is done by solving for the Jacobian ( $J$ ) at each time step such that:

$$\dot{X} = JX + Bu \quad (7.16)$$

where:

$$J = \begin{bmatrix} \frac{\partial f_1}{\partial x_1} & \dots & \frac{\partial f_1}{\partial x_n} \\ \vdots & & \vdots \\ \frac{\partial f_n}{\partial x_1} & \dots & \frac{\partial f_n}{\partial x_n} \end{bmatrix}$$

As in Chapter 4, the biases and velocity of the tractor are assumed to be driven by a white process noise such that:

$$\begin{bmatrix} \dot{V} & \dot{\delta}_{bias} & \dot{\gamma}_{bias} \end{bmatrix} = w_{bias}$$

where  $w_{bias}$  is a random process noise vector.

All of the covariance values assumed for the process noise for the tractor states remain unchanged from Chapter 4 (listed in Table 4.1). The covariances of the process noise for the four additional implement states are listed in Table 7.3

Table 7.3 Additional Covariance Values for Process Noise of the Implement States.

Implement State	Covariance
$e_I$	$0.1 \text{ m}^2$
$n_I$	$0.1 \text{ m}^2$
$\gamma$	$0.01 \text{ rad}^2$
$\gamma_b$	$1.0 \times 10^{-6} \text{ rad}^2$

As was done in Chapter 4, the radar and gyroscope biases estimated in the first filter are used to correct the sensors used as measurements in this second filter. The observation matrix ( $C$ ) is defined by the measurement model equation:

$$Y_{meas} = CX + v \quad (7.17)$$

where:  $Y_{meas} = \begin{bmatrix} \delta^{pot} & \psi^{gyro} - g_{bias} & V_x^{radar} - r_{bias} & e_I^{GPS} & n_I^{GPS} & \gamma^{inv\_kin} \end{bmatrix}^T$

$v$  = unknown sensor noise vector (9x1);

The same sensor noise covariances for each of the sensors from Chapter 4 (listed in Table 4.2) are used in this chapter. Recall that carrier-phase Differential GPS is used to

measure the position of the implement as well as the position of the tractor. Therefore the covariance of the measurement noise is the same for the implement position and tractor position measurements. The covariance of the pseudo implement angle measurement ( $\gamma^{inv-kin}$ , calculated using the inverse kinematics detailed in Section C.4) was assumed to be  $3.0 \times 10^{-4} \text{ rad}^2$ . Note that there are three sensor biases in the second estimator such that:

$$\begin{aligned}\delta^{pot} &= \delta + \delta_{bias} \\ V_x^{radar} &= V_x + r_{bias} \\ \gamma^{inv-kin} &= \gamma + \gamma_{bias}\end{aligned}\tag{7.18}$$

The Extended Kalman Filter (EKF) is comprised of a measurement update and time update [Stengel, 1994], which are performed at each time step ( $k$ ). The measurement update is described by:

$$\begin{aligned}L_k &= P_k C^T (C P_k C^T + R)^{-1} \\ \hat{X}_k &= \hat{X}_k + L_k (y_{meas} - C \hat{X}_k) \\ P_k &= (I - L_k C) P_k\end{aligned}\tag{7.19}$$

where:  $L$  = Kalman Gain Vector  
 $P$  = State Estimation Covariance Matrix  
 $C$  = Observation Matrix  
 $R_v$  = Sensor Noise Matrix  
 $I$  = Identity Matrix  
 $\hat{X}$  = State Estimate Vector

The time update is described by:

$$\begin{aligned}\hat{X}_{k+1} &= \dot{X}_k \Delta t \\ P_{k+1} &= \Phi P_k \Phi^T + Q_w\end{aligned}\tag{7.20}$$

where:  $\Phi$  = discretized Jacobian ( $J$ ) at each time step  
 $Q_w$  = discretized process noise matrix  
 $\Delta t$  = sample rate  
 $\dot{X}$  is obtained from Equations (7.1, 7.5, 7.6, 7.13, & 7.15)

The EKF provides estimates of all the states in Table 7.2 at every time step. The process noise matrix ( $Q_w$ ) was taken to be a diagonal matrix, which assumes no correlation for the process noise of any of the states. The values of each diagonal were the process noise covariance of the corresponding state as listed in Table 4.1 and Table 7.3. Similarly the

sensor noise matrix ( $R_v$ ) was taken to be diagonal using the sensor noise values in Table 4.2 and  $3.0 \times 10^{-4} \text{ rad}^2$  for the pseudo implement angle measurement ( $\gamma^{\text{inv\_kin}}$ ).

## 7.4 Experimental Implement Control Results

The implement control was tested on the aforementioned John Deere tractor pulling a 7.93 m (26 foot) wide chisel plow shown in Figure 7.8. A GPS antenna was placed at the rear of the implement ( $L_I=6.51 \text{ m}$ ) to provide 2 cm positioning of the implement (in addition to the GPS receiver on the tractor). The control point for the implement was set at the GPS antenna location.



Figure 7.8 GPS Guided Farm Tractor and Implement.

The tractor was given line trajectories to follow, starting from some offset from the line to simulate step responses. The majority of the experimental runs were performed at about 2 m/s (4.5 mph). Figure 7.9 shows a simulation of a unit step response for lateral control of the tractor. Figure 7.9a uses a control algorithm to control the position of the tractor, while Figure 7.9b has the feedback wrapped around the position of the implement. As seen in the figure, by controlling the implement, the tractor overshoots quite a bit in order to bring the implement lateral error to zero approximately 50% faster

(and in a very similar fashion to the way the controller brings the lateral error of the tractor to zero in Figure 7.9a).

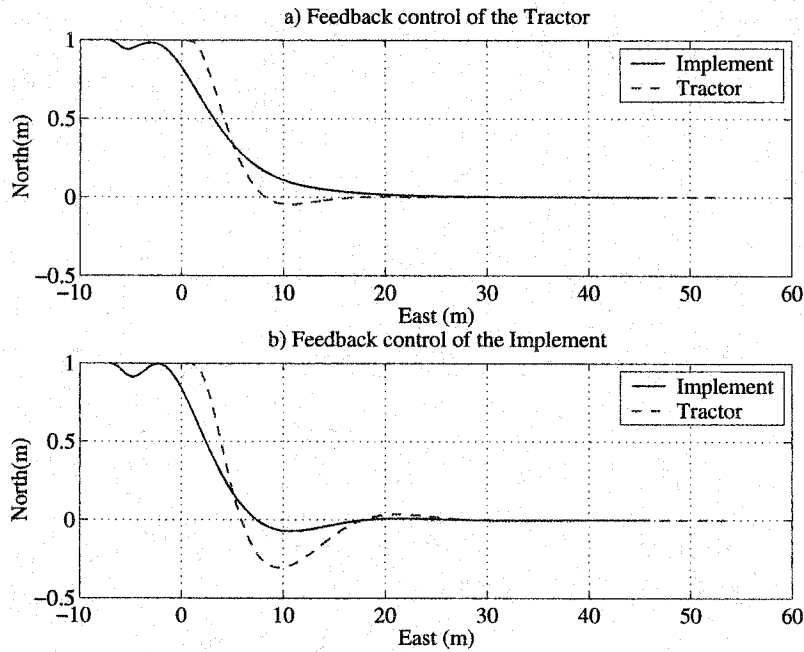


Figure 7.9 Simulation of Tractor-Implement Step Responses.

Figure 7.10 shows an experimental step response of the tractor and towed implement. The desired trajectory is a line at 0 m North. As seen in the figure there exists a slight offset in the implement position even on flat terrain. This bias will most certainly be more pronounced and vary in an uncertain manner on hilly terrain. It is also evident that the implement controller is commanding the large overshoot of the tractor in order to bring the implement to the desired line as in the simulation shown in Figure 7.9b. Comparisons of the simulated and experimental step responses for two different initial condition runs are shown in Figure 7.11.

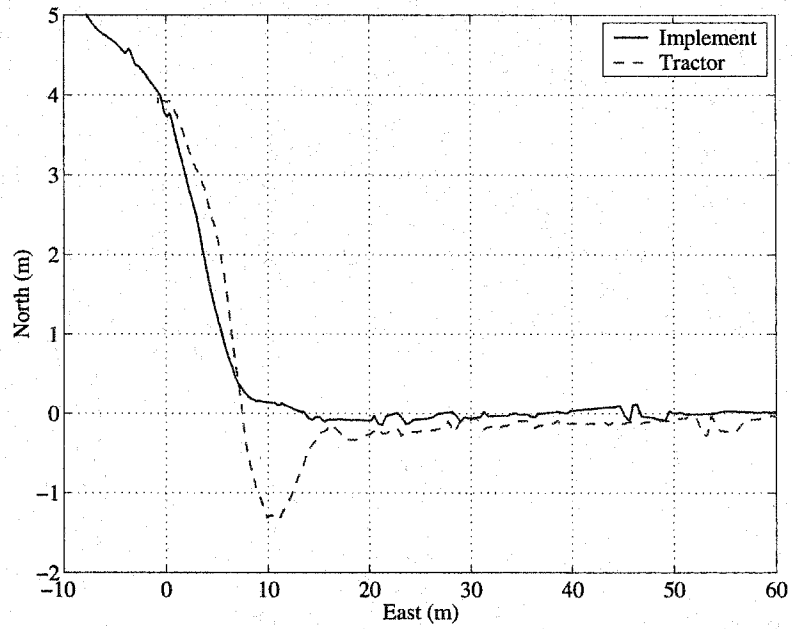


Figure 7.10 Experimental Implement Step Response.

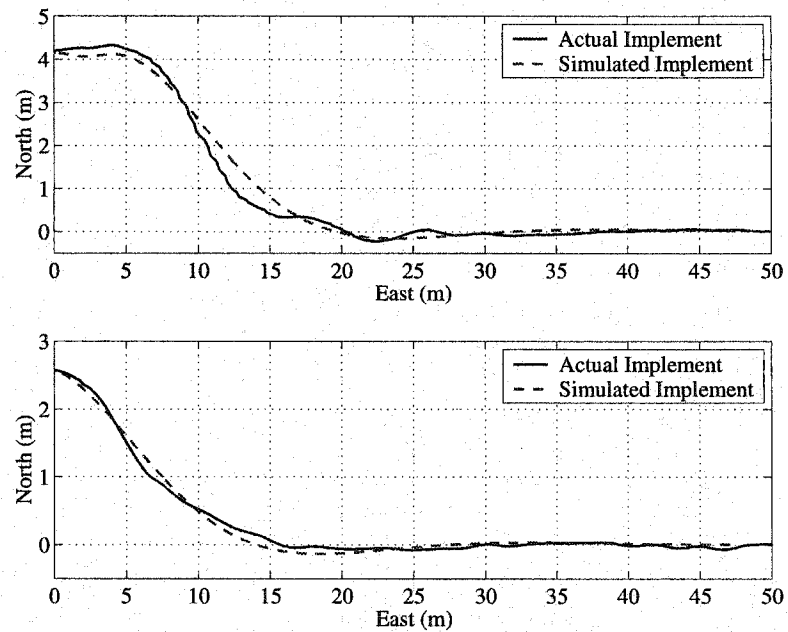


Figure 7.11 Comparison of Simulated and Experimental Implement Control Step Responses for Two Different Initial Conditions.

Figure 7.12 shows the lateral implement error (as measured with GPS) from four various step responses from varying distances from the desired tracking line, as well as a zoom in of one step response. The ensemble error of the lateral controller (once the desired line was reached) on the four runs was 1.4 cm with a standard deviation of 6.5 cm. Additionally, as shown in the bottom half of the figure, the implement errors remained within 10 cm. Recall that the accuracy of the GPS position sensor is 2 cm. The lateral accuracy measurements in Figure 7.12 include this 2 cm of GPS position noise.

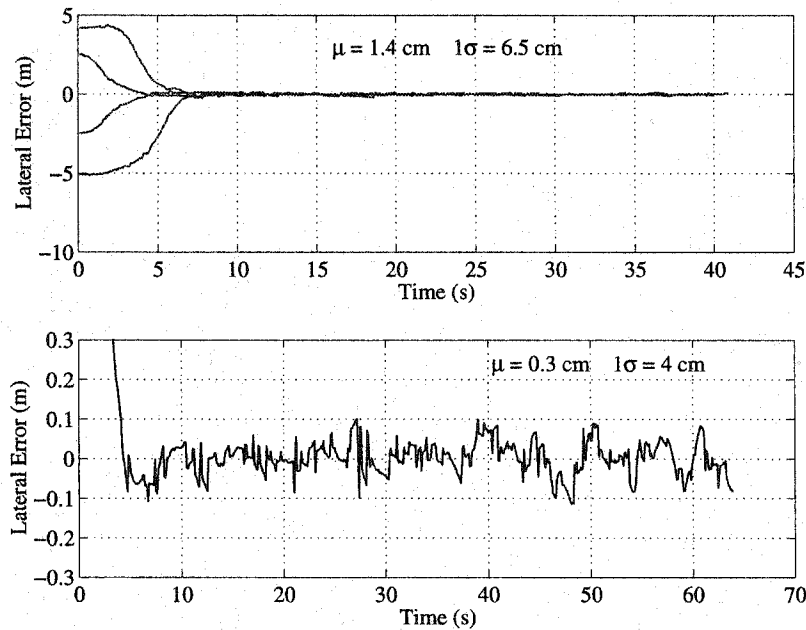


Figure 7.12 Implement Lateral Tracking Errors.

Figure 7.13 is a simulation of the implement control about an arc. The tractor implement starts with a 1 m step response tracking a straight line near (0 m,0 m). The implement is controlled about a 15 meter radius arc centered at (45 m,15 m). Both the implement and tractor positions for the simulated experiment are shown in the figure. Additionally, the lateral tracking errors of the implement and tractor positions and the implement angle from the simulated run are shown in Figure 7.14 and Figure 7.15, respectively.

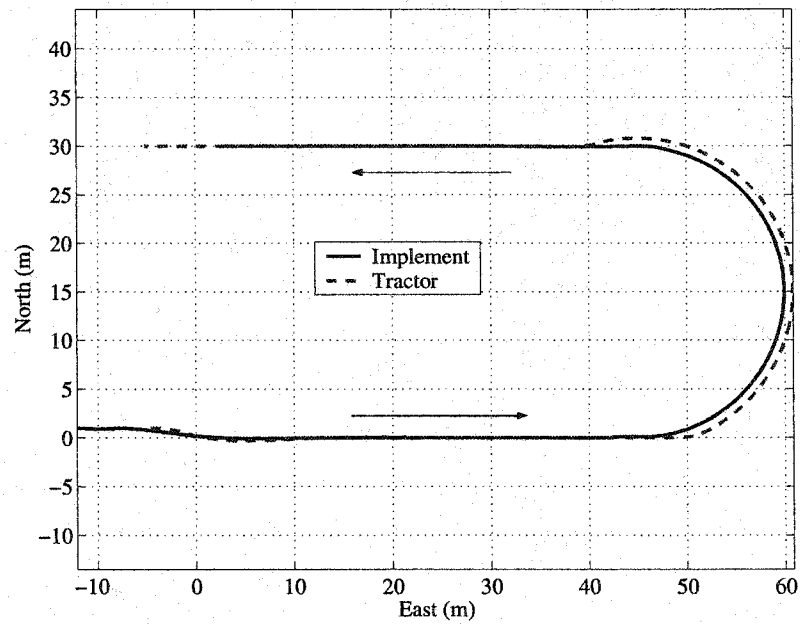


Figure 7.13 Simulated Control of the Implement Along an Arc.

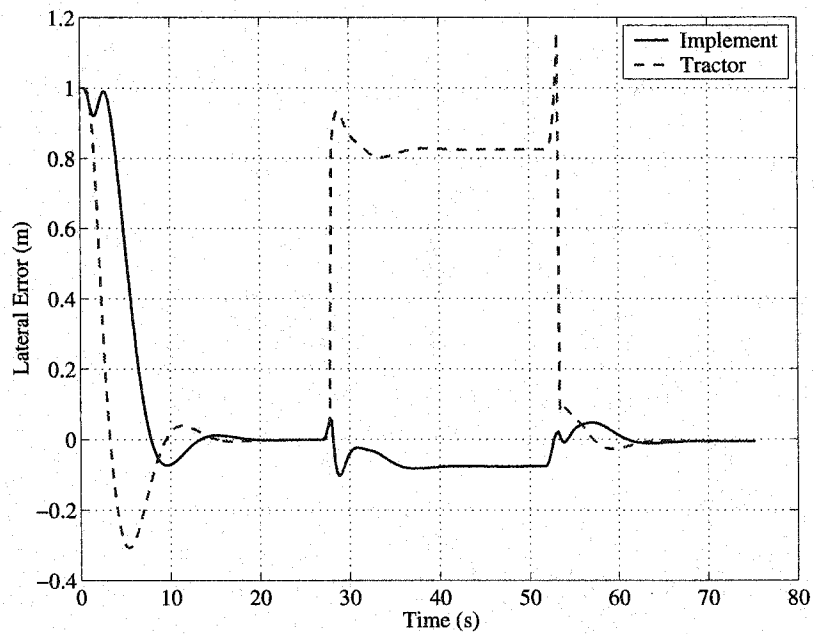


Figure 7.14 Lateral Errors of Implement and Tractor Position for the Simulated Arc Trajectory.



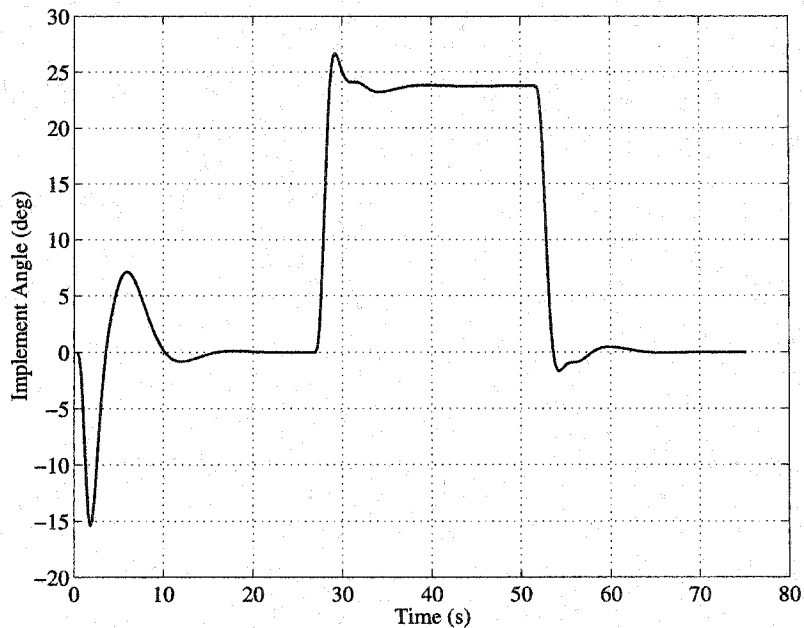


Figure 7.15 Implement Angle During Simulated Control Along an Arc.

Finally, Figure 7.16 shows the implement controller tracking a 35 m diameter circle centered at (0 m,50 m). Note that the implement does not start tracking the arc at the tangent of the arc. Rather, the implement was tracking a line and then was asked to track the circle once it reached the edge of the arc. The lateral error while tracking the arc was 2.5 cm with a standard deviation of 3.5 cm. The lateral errors of the implement and tractor position are shown in Figure 7.17. Notice that in order to achieve approximately 5 cm RMS tracking error with the implement, the tractor position is about *1 meter* outside the desired arc. This discrepancy shows the importance of being able to control the implement position on curved trajectories.

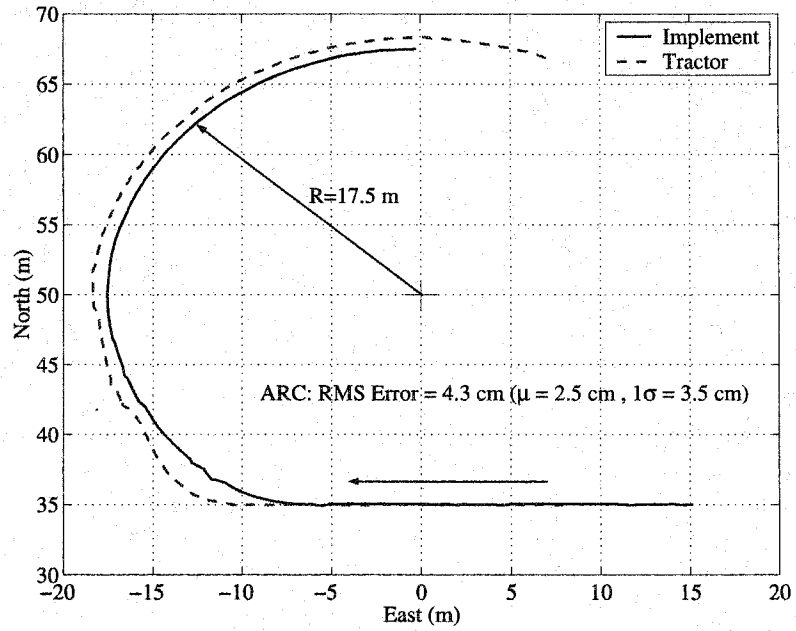


Figure 7.16 Experimental Control of the Implement Along an Arc.

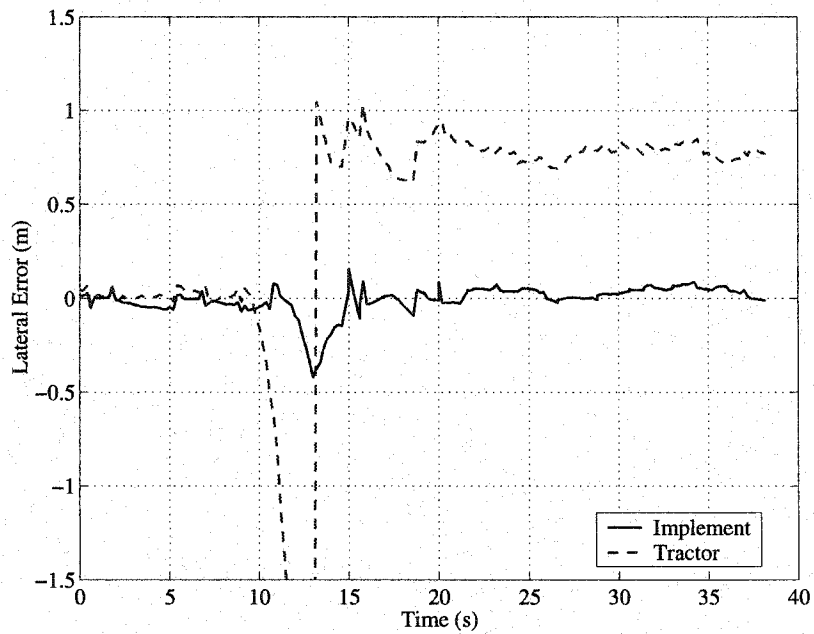


Figure 7.17 Lateral Errors of Implement and Tractor Position for the Experimental Arc Trajectory.

## 7.5 Conclusions

This chapter has demonstrated the position control of a tractor towed implement using Carrier-Phase Differential GPS measurements on both the tractor and implement. A simple kinematic model of the implement was used for the control algorithm. The parameters for the kinematic model were identified *a priori* and validated with an open loop simulation by comparing the model and actual implement angles. An LQR controller was then developed for the implement-tractor combination. Experimental step responses and line tracking tests were performed on flat terrain in order to provide initial evaluation of the methodologies. The experiments show the feasibility of a simple LQR algorithm to control the implement by producing lateral tracking accuracies of 5 cm ( $1\sigma$ ). Additionally, it was shown that settling times are decreased by 50% and curves can be directly tracked through feedback control on implement position. However, no conclusions can be drawn at this time as to the controller's effectiveness as trajectories become more demanding and slope angles increase.

At this time it is also unknown how much the model parameters of the tractor and implement vary with changing soil, implement type, implement load and *implement depth*. These types of changes may vary the tractor model and also vary the implement's ZLV location (which changes the model parameters in Equation (7.2)). The identified model parameters were close to physical measurements of the implement. If, however, the location of ZLV is found to be variable, it may be necessary to identify these parameters in real time in order to adapt the compensator for the variations in tractor conditions. As mentioned previously, it may be quite possible to simplify the tractor model since the closed loop bandwidth of the implement controller is well below the yaw dynamics of the tractor. This may allow for easier adaptation of the model in real time. Ultimately, the need for adaptation will also depend on the accuracy requirements placed on implement control. Acceptable accuracies may be obtained using the physically measured parameters of the implement with some robust controller that ensures stability over the implement model's variations.

## Chapter 8

# Conclusions and Future Work

### 8.1 Conclusions

The models and the control and estimation algorithms discussed in this thesis will ultimately lead to significant improvements in performance, productivity, and robustness, for automatically steered farm vehicles. There has been much previous research on automatic steering control of farm vehicles using GPS. This thesis has extended these previous works to include control at high speeds, GPS/INS integration, and control of towed implements. Specific conclusions and contributions of this thesis can be summarized as follows.

- Accurate high speed control, for operations such as spraying, to within 4 cm ( $1\sigma$ ) and up to 16 mph, can be obtained using the new identified tractor yaw dynamic model. An analytical model with a significant front tire relaxation length can capture the dynamic characteristics of this new identified model.
- A cascaded estimation architecture can estimate all biases and states required for accurate control. The algorithm provides more accurate estimation of the sensor biases and tractor states as well as more accurate dead reckoning state estimation during GPS outages. Additionally, the cascaded architecture simplifies the real time

calculations for estimating all of the states required for control and dead reckoning navigation of the farm tractor.

- The cascaded estimation algorithm can provide position estimates through dead reckoning for control of the tractor through GPS outages. The first (6<sup>th</sup> order) filter can estimate the position and heading of the vehicle, even during periods with no GPS measurements, as well as the inertial sensor biases. The second (6<sup>th</sup> order) filter can estimate the remaining states required for full state feedback. The algorithm allows continuous control of the tractor to within one foot for short (20-40 second) GPS outages. Additionally,  $\frac{\lambda}{2}$  (9 cm) tracking accuracies are achievable for approximately 5 seconds without any GPS measurements, allowing for carrier wave integer recovery.
- The growth of heading and position errors occurring from integration of sensor noises (dead reckoning) during short GPS outages can be predicted using the error growth equations developed in this thesis. These error growth models adequately predict the experimental dead reckoning error growth through short GPS outages.
- Accurate lateral control, to within 4 cm ( $1\sigma$ ), can be obtained without GPS attitude measurements. This method requires a low cost accelerometer and gyroscope to provide attitude estimation for the tractor.
- Towed implements can be controlled to within 10 cm of a desired path using the implement control algorithms developed in this thesis. Additionally, curves can be directly tracked and step response time decreased by approximately 50% by using direct feedback control of the implement position. A kinematic model of the towed implement can adequately describe the implement dynamics required for control of the implement.

## 8.2 Future Work

Automation of off-road vehicles, specifically automatically steered farm equipment using GPS, will become widespread in the near future. Initial architectures are in place that make it possible to do the most fundamental steering control. However, as these systems become more widespread, several issues must be resolved. Farm equipment experiences a wide range of operating conditions (varying loads, ground conditions, implements, tire configurations, etc.), which significantly change the models upon which the control and estimation algorithms are based. Currently, extensive *a priori* system identification and hand tuning of the control weights as well as the Kalman filter parameters are used. Algorithms that can adapt to changing environments will be necessary to expand their use to multiple farming applications. Current low volume sales of automated farm equipment allows engineers to calibrate each vehicle upon installation of the guidance equipment. However, automated calibration techniques will become necessary in order to provide larger volume sales.

An adaptive control algorithm based on on-line parameter identification has been developed for a neutral steer tractor model [Rekow, 2000]. Another adaptive technique based on the identification of a “steering coefficient” through the use of an Extended Kalman Filter was also developed [Bell, 1999]. Now that a more accurate yaw model has been developed in this thesis, one avenue of future research is to apply the adaptive techniques of Bell and Rekow to this newly developed model. However, for many farm operations, such as straight lines, these yaw dynamics may be hard to observe [Rekow, 2001].

The yaw dynamic model developed in Chapter 2 was shown to be dependent on a parameter called the tire relaxation length, which depends on the diameter of the tire. Therefore, this important parameter will vary for nearly every vehicle on a farm. Effects of various soils on the tire cornering stiffness and tire relaxation lengths will cause variations in the yaw dynamic model. Other conditions such as field conditions or soil types, tire ballast, and weight distribution may also significantly change the tractor model. The effect of the controlled response of the tractor due to an error in the modeled CG location was also shown in Chapter 3. Therefore some type of real time system

identification or robust control will be necessary to account for the changing dynamics. Additionally, the implement model given in Chapter 7 was shown to be quite dependent on implement depth. The parameters of the implement model will undoubtedly be influenced by changing implements, ground conditions, as well as implement depth. In order to make implement control robust to these changes, an adaptive algorithm will be required that can identify the changing parameters or adapt to the parameter variations.

Even though much progress has been demonstrated in the area of GPS controlled farm tractors, more research will be required to continue to increase the capabilities of these systems. Several such future suggestions, many of which include the broad area of adaptation, are listed below.

*On-line Identification.* New methods for performing on-line system identification and adaptive/self tuning compensators to improve the control and estimation of vehicle states must be developed. Most on-line system identification approaches, including Least Mean Squares (LMS), Recursive Least Squares (RLS), and the Extended Kalman Filter (EKF), are based on an ARX model assumption. This model form has previously proved to be a poor identification algorithm in the presence of low signal to noise ratios. Additionally, system identification in closed loop systems provides biased model parameters due to the correlation of output error and input. More importantly, closed loop systems are not persistently excited, leading to low signal to noise ratios, while tracking certain trajectories, making it difficult to identify certain modes or parameters of the system. One new approach to address the problem of persistent excitation may be to cast the estimation into a hybrid system (a system consisting of continuous and discrete elements) problem formulation. This would allow an estimation algorithm to identify certain parameters when they are most observable and switch to another estimation mode when other parameters, such as the turning dynamics during a planned turn, are more observable. The idea of optimal switching and robustness of the switching system identifier must be addressed. Additionally, algorithms must be developed that ensure no undesired transients are introduced when switching from regime to the next (known as “bumpless” switching). On-line adaptation will be an integral part of making vehicle

control (and many other) systems robust, without sacrificing performance capabilities of the system.

*Self-Tuning Controller and Estimator.* State space techniques such as LQR control and Kalman filter estimation have become increasingly wide spread in industry and academia. However, these methods still assume certain knowledge of the system, such as the sensor and process disturbances. Although sensor noise can be easily modeled, identification of process disturbances to self-tune the Kalman filter is not as trivial. Some theoretical work has been done on the identification of process disturbances. However most, if not all, have provided simulation results only and have not demonstrated the capability on real systems. An LQR algorithm provides an “optimal” control algorithm given a set of LQR weighting matrices. However, these weights are picked somewhat arbitrarily, or are hand tuned until satisfactory performance is obtained. For example, as shown in Chapter 3, placing a weight on the steer angle state provided good controller performance. Because these architectures are used in many vehicle navigation and control applications, the ability to self-tune these algorithms becomes important.

*Real Time Disturbance Identification.* In order to adaptively tune the Kalman filter, an estimate of the process disturbances acting on the system must be known. This process noise can change with field conditions (varying roughness), velocity, as well as tractor configuration. For example, “sloshing” of liquid fertilizer in belly-mounted fertilizer tanks could cause the estimator to become unstable without a proper model of this disturbance. Some disturbances are not white as is assumed under the Kalman filter model. Disturbances such as previous furrows in the ground, called “beds” can cause sinusoidal or colored disturbances. The disturbance identification technique would be used to estimate biases, both constant and cyclical, as well as the covariance of each of the disturbances. Additionally, time constants of estimated biases, such as the vehicle crab angle or steer angle bias, could change due to changes in the terrain. The estimation of the disturbance covariance matrix would allow the Kalman Filter to be tuned in real time to optimally estimate the states of the vehicle. Tracking and robustness could be improved if these various disturbances could be modeled in real time.



*Inertial Sensor Scale Factor Estimation.* In this thesis, all scale factors on inertial sensors (the accelerometer in Chapter 6 and the gyroscope in Chapters 4-5) were assumed to be known. In Chapter 5, it was shown how errors in the scale factor can lead to errors in the dead reckoning estimation. However, only sensor biases were estimated in this thesis. This is because estimating the scale factor is a nonlinear estimation problem. Additionally, and probably more importantly, sensor scale factors are less observable. For example, during straight line tracking, the gyroscope's scale factor is not observable. However, a method which estimates the sensor's bias while the vehicle is driving in a straight line, and then identifies the sensor's scale factor at the end of the field when the vehicle must turn around could be developed. As with the vehicle parameter identification mentioned previously, this creates a need for a well designed switching estimation algorithm which must be carefully analyzed for stability. The ability to estimate sensor scale factors in real time will provide better dead reckoning accuracy, especially during U-turn operations or other curved trajectories.

*Modeling/Control of Other Agricultural Vehicles.* As automated farming becomes widespread, it will be desirable to automate all aspects of the farm. If a farm is planted using GPS, then why not harvest using GPS. The range of vehicles on a farm is quite broad, ranging from front steered vehicles as used in this thesis, to rear steered vehicles, articulated vehicles, tank steer (track) vehicles, etc. Models for tank steer and articulated vehicles have been developed in [Crolla, 1983]. However, these models have never been used for control and therefore their validity never verified for use in a closed-loop system. Another vehicle that would be of extreme interest for modeling and control is a "High Boy" spray vehicle like the John Deere 4710. This vehicle has an active suspension system and 90 foot spray boom for smooth spraying up to 22 mph. It would be interesting to see what effect the suspension has on the model dynamics. Additionally, the vehicle has 6 foot diameter front and rear tires, to provide crop clearance. As discussed in Chapter 2 the large tires of agricultural vehicles require a relaxation length in the tire model (that is related to the tire diameter) to capture the yaw dynamics. It would be interesting to see if these larger tires of the spray vehicle do indeed extenuate the effect of the tire relaxation length in the yaw model. Additionally, a thorough tradeoff

analysis of model complexity versus control accuracy should be conducted with each vehicle.

*Human-like Adaptation to Driving.* Growing up on a farm, I learned to drive a tractor at the age of 10. It was not difficult to go from knowing how to drive a tractor, to being able to steer a combine, or other tractors. A complicated model, or knowledge of the deadband zone in the steering column was not required. At age 27, I drove a tracked vehicle for the first time. At first I was a little “wobbly,” but within a few seconds I had “adapted” to its driving characteristics quite well. Humans have no problem adjusting to steering these vehicles at any speed. However, in Chapter 2, it was shown that the omission of the tire relaxation length could cause the control algorithm to become unstable. It would be interesting to determine what humans use as references and models to allow us to be so extremely robust in driving various vehicles. This human factors information would allow automatically steered controllers to be placed on any vehicle (that a human could be expected to drive) as it comes off the assembly line, eliminating the need to model each new version of farm vehicle developed.

*Path Planning.* With the ability to accurately control a tractor through a field comes the freedom to farm a field on any particular path. Any path can be commanded and tracked by an automatically steered tractor. Therefore it is no longer limited to what a human is comfortable tracking. Optimization schemes could be run to assess the most efficient way to plow a field, minimizing turning times. When planting in beds or harvesting crops, farmers often skip a set number of rows (which they could easily count during these operations). For other operations, a farmer cannot “eyeball” the spacing accurately enough. However with an automatically steered tractor this is an easy possibility. A tractor could plow a field, skipping an implement width the entire time, then come back and fill in the gaps – if this proved to be the optimized method, given the tractor/implement characteristics such as turning radius and implement width.

*Collision/Obstacle Avoidance.* Many fields will contain fixed obstructions such as telephone poles, large boulders, windmills, etc., as well as moving obstructions such as other farm vehicles. Hitting, for example, a telephone pole with high voltage lines with

an implement can not only be dangerous to the operator, but will also damage the guidance equipment. Algorithms which try to perform the desired task without causing a collision must be developed. These algorithms must account for the specific dynamic characteristics, such as the tractor/implement model, in order to avoid various obstacles, yet still control the implement accurately around the obstruction. One of the most significant barriers to real productivity gains from such a system will be safety and risk avoidance. These systems will have to be proven safe and possibly certified (with OSHA, for example) as aircraft are certified. Various “fail-safe” features of the vehicles must be explored. This will ultimately lead to the ability to use fully autonomous tractors which in turn can bring many additional benefits to the agricultural community.

## 8.3 Closing

It goes without saying that farming and farmers provide an essential service. However, there continues to be a decrease in the ratio of farm producers to consumers. Therefore, farms must better manage their resources to provide optimal production. Because of this need, many new technologies, including automatically steered farm tractors using GPS, have already become a reality in the marketplace and on farms. As these systems become more widespread, the tasks which farmers demand of their automatically steered tractors will grow. Farmers will want automatic steering for spraying and through short GPS outages. Additionally, farmers will eventually want to control the position of the implement. This will lead to advances in new agricultural techniques such as farming on side-hills, pulling larger implements with more precision, or narrower spaced planting. These advances will require accurate knowledge of the yaw dynamics, INS/GPS integration, and implement control algorithms developed in this thesis. These new capabilities, which have been the focus of this thesis, will need to be integrated into current systems in order to provide leading edge technologies and advanced capabilities to farmers.

## Appendix A

### Experimental Hardware

All of the work performed in this thesis was implemented on a John Deere 8400 tractor, under loan to Stanford University from John Deere, shown in Figure A.1. The major components of the automatically steered tractor are:

- Trimble TANS Vector
- IntegriNautics carrier-phase Differential GPS system
- Linear Potentiometer (John Deere Part No. AZ52077)
- Motorola HC12 Microprocessor
- Experimental Electro-Hydraulic Valve
- Industrial Computer Source PC
- Radar (John Deere Part No. RE152877)
- KVH Autogyro Fiber Optic Gyroscope
- Systron Donner Gyroscope (AQRS-00064-104)
- Humphrey Accelerometer (LA01-0501-1)
- Pacific Crest RFM96 Radio Modems
- FreeWave Radio Modems (DGR-115/115H)

The four antenna TANS Vector GPS unit provides three-dimensional positioning accuracy of 2 cm and an attitude accuracy of 0.1 deg in each axis. Full attitude is required to transpose the GPS measurements from the roof of the tractor to a control point on the ground below the axle of the tractor [Bell, 1999]. The tractor uses the linear potentiometer to measure the steering wheel angle and an electrically actuated steering

valve is used to provide a steering slew rate. A Motorola 68HC12 microprocessor interacts with the steering valve and potentiometer and communicates with the master computer via serial communication. The master computer runs the control and estimation algorithms at a 5Hz update rate using a Lynx real time operation system. The tractor was equipped with a radar for measuring velocity. The radar is standard on most new tractors. It is used for providing an accurate measure of the vehicle speed for operations such as planting and spraying (where application rate is critical) as well as providing a means to estimate wheel slip. A KVH fiber optic gyroscope (FOG) was used for sensing yaw rates. Although off-road vehicles are subject to large amounts of mechanical vibrations, the non-mechanical FOG can provide excellent yaw sensing under these conditions. However, typical mechanical gyroscopes generally create sensing errors when subjected to vibrational accelerations. The  $1\sigma$  sensor noise on the FOG and radar are 0.44 deg/sec and 0.12 m/s, respectively. Sensor noises of the various sensors used in this work are summarized in Tables 4.2 and 6.2.

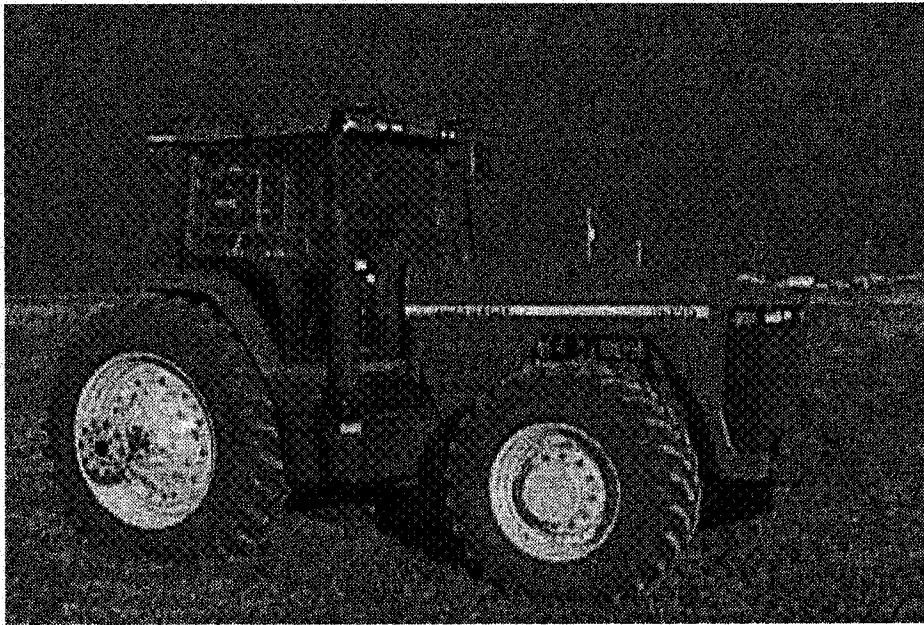


Figure A.1 GPS Guided Farm Tractor.

The John Deere 8400 has the following characteristics:

- 225 hp turbo charged in-line 6 cylinder diesel engine
- 16 forward gears up to 22 MPH

- Four wheel drive
- Lockable rear differential
- Adjustable Ballast
- 18,700 pound unballasted gross weight
- Powershift transmission
- Length of 207 inches, axle width of 118 inches and height of 120 inches

The major components of the system are shown in Figure A.2. The upper left hand corner shows the linear steer angle potentiometer which is mounted between the front steer wheel and the frame of the tractor. The lower left hand corner shows the inertial sensors (KVH gyroscope and Humphrey accelerometer) used in this thesis. The inertial sensors were simply placed on the floor board inside the cab of the tractor. The lower right hand corner shows the four GPS antennas mounted to the roof of the cab. The four antennas were required by the Trimble Vector attitude system. The upper right hand corner shows the mounting of the “brains” of the system. The computer, GPS receiver, radio modem, and Trimble Vector were all mounted in the rack shown in the figure.

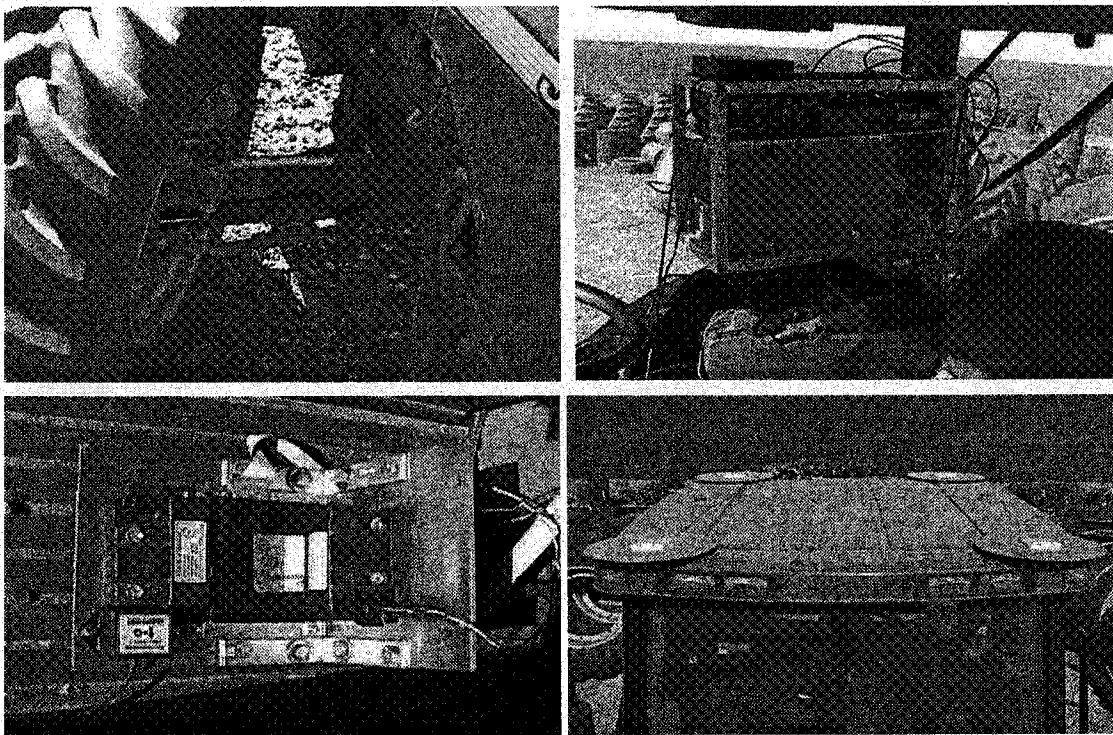


Figure A.2 Components of the GPS Farm Tractor.

The diagram illustrates the GPS-based steering control system architecture. It shows the flow of data from various sensors and antennas through processing blocks to the control software.

- Reference Station Antenna** (top center) connects to a **GPS Receiver**, which then connects to a **Radio Modem**.
- Tractor Antennas** (top left) connect to a **Vector** block, which outputs **Tractor Attitude (Yaw, Roll, Pitch) [ $\psi \ \theta \ \phi$ ]** to the **CONTROL SOFTWARE**.
- A **GPS Receiver** (middle left) receives data from the **Vector** block and outputs **Tractor Position [East North Up]** to the **Positioning Software**.
- The **Radio Modem** (middle center) connects to the **Positioning Software** on both sides.
- An **Implement Antenna** (top right) connects to a **GPS Receiver**, which outputs **Implement Position [East North Up]** to the **Positioning Software**.
- The **Positioning Software** (middle right) outputs **Implement Angle [ $\gamma$ ]** to the **Inverse Kinematics** block.
- The **Inverse Kinematics** block (middle) receives inputs from the **Tractor Position**, **Implement Position**, and **Tractor Attitude**, and outputs **Implement Angle [ $\gamma$ ]** to the **CONTROL SOFTWARE**.
- The **CONTROL SOFTWARE** (bottom center) receives inputs from the **Tractor Position**, **Implement Position**, **Implement Angle [ $\gamma$ ]**, and a **Desired Implement Position [East North]** block. It contains a **Kalman Filter** and **LQR Control** block.
- A **Steer Angle Potentiometer** (bottom left) outputs  **$\delta$**  to the **CONTROL SOFTWARE**.
- The **CONTROL SOFTWARE** outputs the **u (commanded steer input)** (bottom center).

## Appendix B

### Identification of the HC12 Delay and its Effect on the Yaw Dynamic Modeling

As discussed in Appendix A, a Motorola 68HC12 microprocessor was used to measure the steering potentiometer and communicated with the master computer via a serial port (at 9600 baud). This communication delay led to a “mysterious” zero in the initial system identification given in Chapter 2. In later experimental tests, data was collected via the 68HC12 as well as with an A/D board onboard the master computer as shown previously in the schematic in Figure 2.2. The difference in measurements at the A/D board and from the 68HC12 were examined to determine the 68HC12’s effect on the system identification presented in Chapter 2. Once the delay was identified, it was accounted for in the data used for identifying the tractor yaw dynamics.

First, software was written to collect only steer angle measurements from the A/D board and the HC12. The relationship between the two different steer angle measurements was assumed to be a linear transfer function as:

$$\frac{\delta_{HC12}}{\delta_{A/D}} = H(z) \quad (B.1)$$

A Box-Jenkins first order model (one pole and no zeros) was used to fit the transfer function given in Equation (B.1). This analysis was completed for several sample rates. The discrete pole location of the Box-Jenkins fit for the various sample rates is shown in



Figure B.1. A pure delay would result in a pole at  $z=0$ . Therefore from Figure B.1, the delay can be approximated as 0.038 seconds.

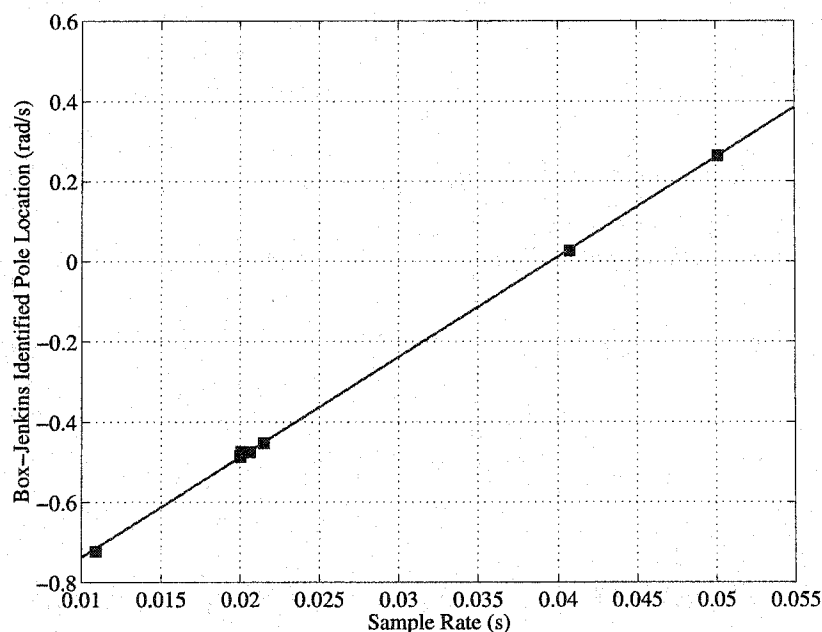


Figure B.1 Pole Location of a First Order Model of  $H(z)$  for Various Sample Rates.

Figure B.2 shows the empirical transfer function of the input-output data as well as the first order Box-Jenkins fit of the transfer function. Also shown is the frequency response of a pure delay of 0.038 seconds. Therefore it was concluded that there was indeed a delay in the HC12 measurements (of at least 0.038 seconds) in the data taken for system identification. As seen in the figure, the pure delay of 0.038 seconds characterizes the difference in phase between the two measurements quite well (especially in the frequency range of the tractor yaw dynamics).

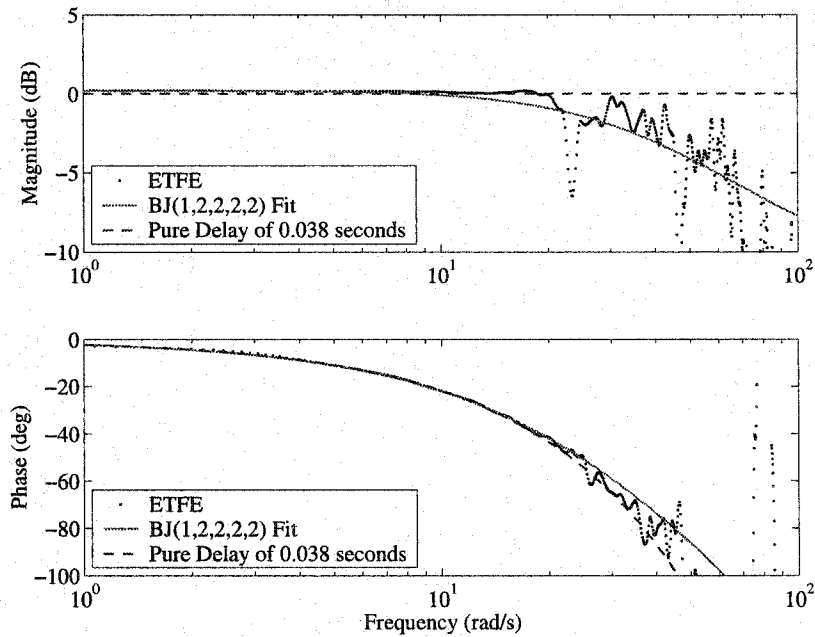


Figure B.2 Spectral Analysis (ETFE), First Order Box-Jenkins Model, and a Pure Time Delay Model of  $H(z)$ .

The phase lag of the HC12 steer angle measurements seen in Figure B.2 attributed to a fictitious zero in the initial yaw dynamic model fits. Although the delay was found to be 0.038 seconds when recording only HC12 and A/D steer angle measurements, when analyzing the data taken for system identification, the delay appeared to be more on the order of 0.075 seconds. The software used to take data for system identification was not only recording the steer angle measurements, but also the GPS position and attitude of the tractor, as well as tractor yaw rate measurements from the gyroscope. This additional complexity may have caused the HC12 measurements to be delayed by an additional sample above the 0.038 second delay. Recall that the nominal sample rate for the yaw model system identification was 0.05 seconds.

Figure B.3 shows the zero locations using a second order Box-Jenkins fit with one time delay (BJ[2 2 2 2 1]). This results in a transfer function with two poles and one zero. As seen in the figure, the zero is not negligible in the data taken with the HC12. However, data taken with the A/D board must be delayed 0.075 seconds in order to create a similar zero location in the input-output data. The zero also appears be proportional to

$V^{-1}$  which can be predicted by the bicycle model. However, the zero in the TR and FTR models, which better characterized the tractor yaw mode, is canceled by an additional pole (and therefore is characterized by a model that effectively has no zero).

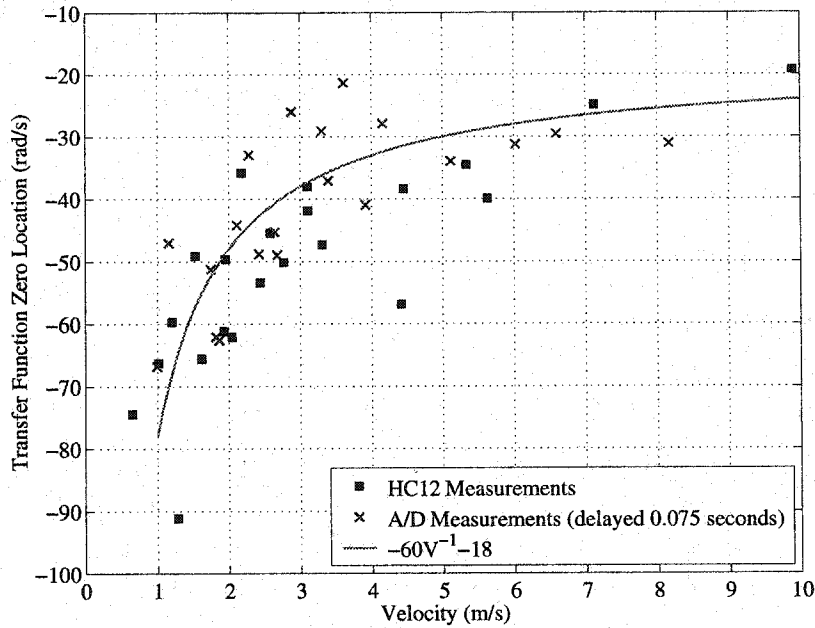


Figure B.3 Comparison of Identified Zero Location with A/D Measurements (Delayed by 0.075 Seconds) and HC12 Measurements.

Figure B.4 shows the modeling errors from various order fits (with and without a zero in the transfer function) using the A/D measurements. Figure B.5 shows the modeling errors from the various order fits using the raw HC12 measurements (Figure B.5a) and the HC12 measurements shifted forward by 0.075 seconds (Figure B.5b). Note that the zero is only important (in terms of modeling error) for the identification using the raw HC12 measurements.

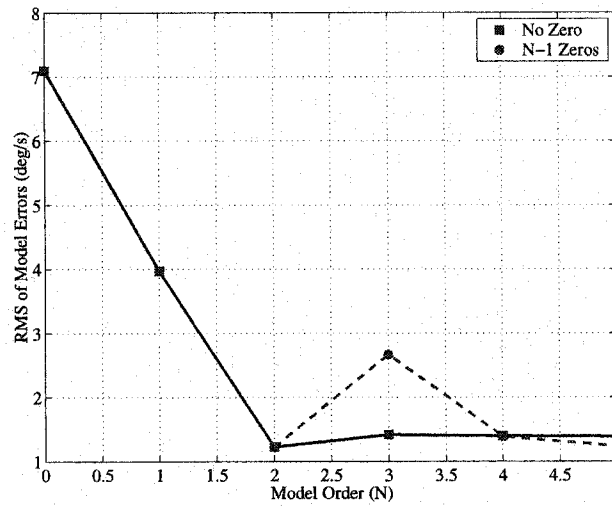


Figure B.4 Model Errors vs. Model Order for No Zeros and N-1 Zeros for Identification Using A/D Measurements.

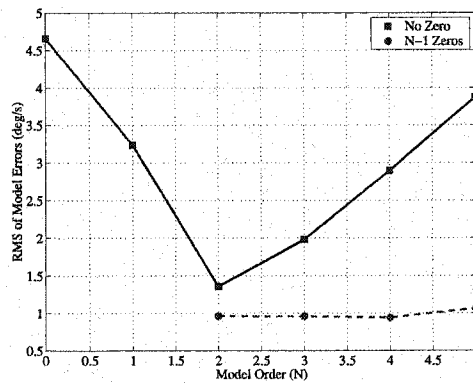


Figure B.5a Model Errors vs. Model Order for No Zeros and N-1 Zeros for Identification Using HC12 Measurements.

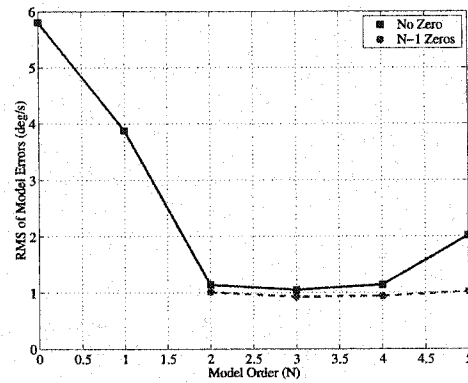


Figure B.5b Model Errors vs. Model Order for Identification Using HC12 Measurements Shifted Forward by 0.075 Seconds.

Finally, Figure B.6 shows the transfer function characteristics of the system identified yaw model for all data sets using the HC12 steer angle measurements and the A/D steer angle measurements. Note that the delay in the HC12 steer angle measurements only affects the location of the zero in the model. The zero locations occurring to the right of the imaginary axis (positive zeros) in Figure B.6 are from discrete zeros of the identified

model outside of the valid identification frequency range. These zeros therefore have virtually no effect (or benefit) in modeling the input/output data.

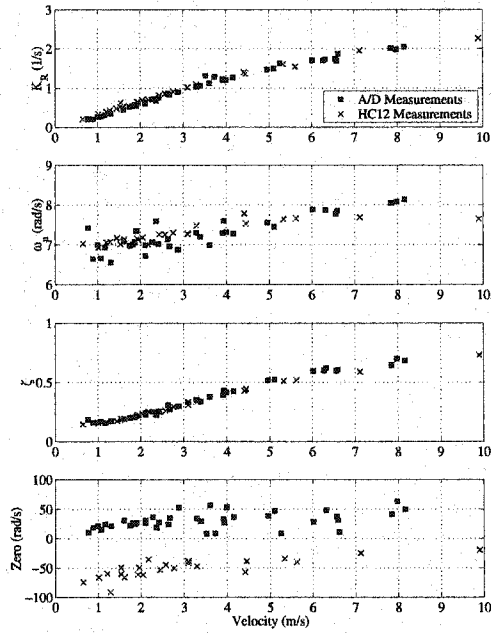


Figure B.6a Comparison of ID2 Data with A/D Measurements and HC12 Measurements.

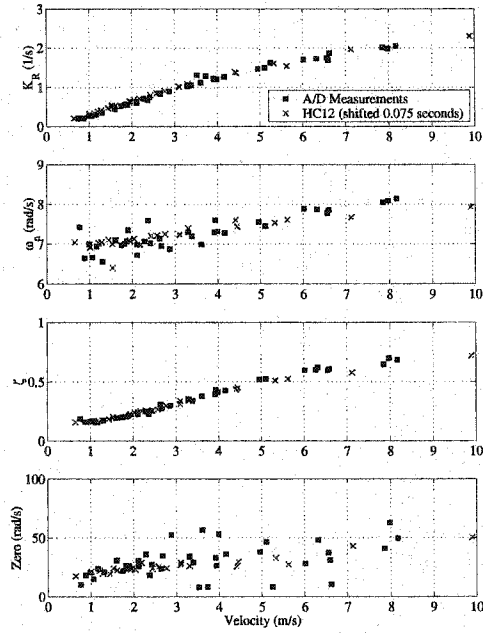


Figure B.6b Comparison of ID2 Data with A/D Measurements and HC12 Measurements Shifted Forward by 0.075 Seconds.

To conclude, all HC12 measurements were assumed to be delayed by 0.075 seconds and were therefore shifted forward by 0.075 seconds in all of the system identification for both single and dual rear wheels presented in Chapter 2. Shifting the HC12 measurements forward by 0.075 seconds created models which did not require a zero to adequately capture the yaw dynamics of the tractor.

## Appendix C

### Implement Dynamics and Kinematics

This appendix presents the derivations of the implement angular dynamics, lateral dynamics, as well as the implement's forward kinematics and position dynamics used in the control and estimation algorithms presented in Chapter 7. Additionally, the algorithm for calculating the implement angle (using inverse kinematics) used as a measurement by the estimation algorithm in Chapter 7 is presented.

#### C.1 Angular Dynamics

Figure C.1 shows the implement-tractor combination, including the lateral implement position ( $y_I$ ), the implement's lateral velocity ( $V_L$ ), and the implement's  $x$  and  $y$  velocities ( $V_{I_x}$  and  $V_{I_y}$ , respectively). The implement ZLV, corresponding to the point on the implement with zero lateral velocity, is also shown in the figure.

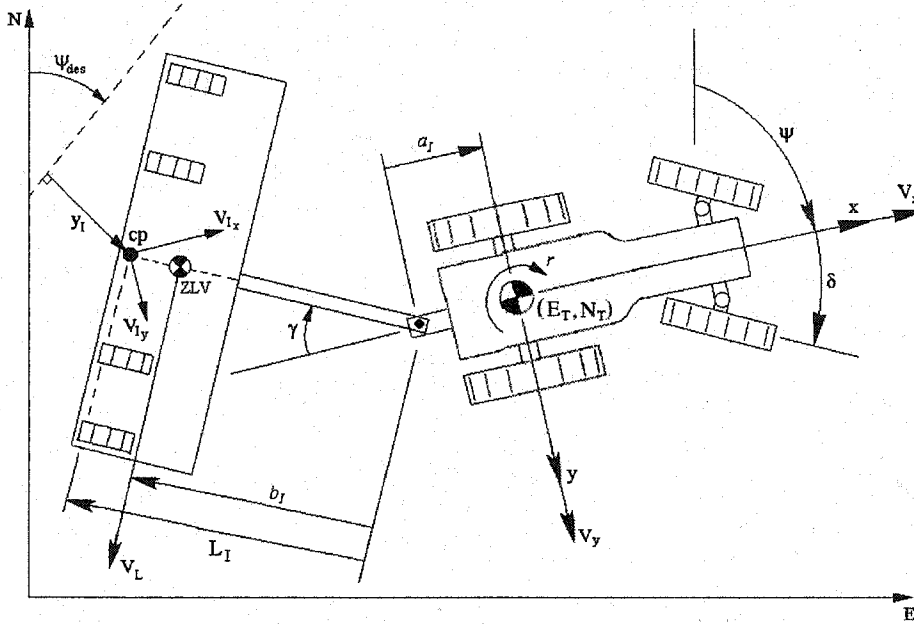


Figure C.1 Schematic of a Farm Tractor and Implement for Calculating the Implement Angular and Lateral Dynamic Models.

The kinematic implement model assumes that there is no lateral velocity at the axle (or at some point, ZLV, along the implement) such that:

$$V_L = 0 \quad (C.1)$$

The sum of the lateral velocities at the ZLV include those due to tractor linear and rotational velocities as well as the rotational velocity of the implement as shown below.

$$V_L = \sum (V_{ZLV})_L = b_I \dot{\gamma} + b_I \dot{\psi} + a_I \dot{\psi} \cos(\psi) + V_x \sin(\gamma) = 0 \quad (C.2)$$

Rearranging terms in Equation (C.2) results in the kinematic implement model describing the rotational rate of the implement.

$$\dot{\gamma} = -\dot{\psi} \left[ 1 + \frac{a_I}{b_I} \cos(\gamma) \right] - \frac{V_x}{b_I} \sin(\gamma) \quad (C.3)$$

## C.2 Lateral Position Dynamics

The velocities of the implement in the  $x$  and  $y$  directions (shown in Figure C.1) are:

$$\begin{aligned}(V_I)_x &= V_x + L_I \sin(\gamma)\dot{\gamma} + L_I \sin(\gamma)\dot{\psi} \\ (V_I)_y &= V_y - L_I \cos(\gamma)\dot{\gamma} - (L_I \cos(\gamma) + a_I)\dot{\psi}\end{aligned}\tag{C.4}$$

The overall lateral velocity of the implement is then defined as:

$$\dot{y}_I = (V_I)_x \sin(\psi) + (V_I)_y \cos(\psi)\tag{C.5}$$

Substituting Equation (C.4) into (C.5) results in:

$$\begin{aligned}\dot{y}_I &= V_x \sin(\psi) + L_I \sin(\gamma)\dot{\gamma} \sin(\psi) + L_I \sin(\gamma)\dot{\psi} \sin(\psi) \\ &\quad + V_y \cos(\psi) - L_I \cos(\gamma)\dot{\gamma} \cos(\psi) - (L_I \cos(\gamma) + a_I)\dot{\psi} \cos(\psi)\end{aligned}\tag{C.6}$$

Assuming small angles and neglecting the square of small angles results in the implement lateral position dynamic equation:

$$\dot{y}_I = V_x \psi - L_I \dot{\gamma} - (L_I + a_I)\dot{\psi}\tag{C.7}$$



### C.3 Position Kinematics and Dynamics

Figure C.2 shows the implement-tractor combination, including the implement position  $(e_i, n_i)$  and implement angle  $(\gamma)$ .

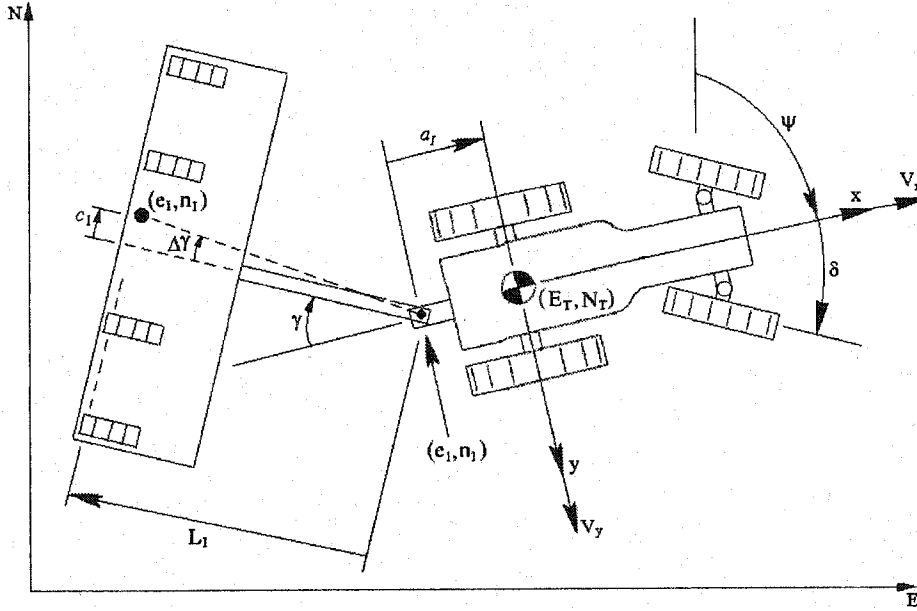


Figure C.2. Schematic of the Tractor and Implement for Calculating Forward and Inverse Kinematics

The position of the implement in the tractor frame is described as:

$$\begin{aligned}(x_I)_T &= -a_I - L_I \cos(\gamma) + c_I \sin(\gamma) \\ (y_I)_T &= -L_I \sin(\gamma) - c_I \cos(\gamma)\end{aligned}\tag{C.8}$$

All the work in this thesis assumes that the position of interest is along the center line of the implement such that  $c_I = 0$ . The position of the implement in the Inertial frame (North-East-Down) is defined as:

$$\begin{aligned}e_I &= E_T + (x_I)_T \sin(\psi) + (y_I)_T \cos(\psi) \\ n_I &= N_T + (x_I)_T \cos(\psi) - (y_I)_T \sin(\psi)\end{aligned}\tag{C.9}$$

Substituting Equation (C.8) (with  $c_I = 0$ ) into Equation (C.9) results in the following forward kinematics describing the implement position:

$$\begin{aligned}e_I &= E_T + (-a_I - L_I \cos(\gamma))\sin(\psi) - L_I \sin(\gamma)\cos(\psi) \\ n_I &= N_T + (-a_I - L_I \cos(\gamma))\cos(\psi) + L_I \sin(\gamma)\sin(\psi)\end{aligned}\tag{C.10}$$

Taking the time derivative of the above equation results in:

$$\begin{aligned}\dot{e}_I &= \dot{E}_T + (-a_I - L_I \cos(\gamma))\cos(\psi)\dot{\psi} + L_I \sin(\gamma)\dot{\gamma} \sin(\psi) \\ &\quad + L_I \sin(\gamma) \sin(\psi)\dot{\psi} - L_I \cos(\gamma)\dot{\gamma} \cos(\psi) \\ \dot{n}_I &= \dot{N}_T + (a_I + L_I \cos(\gamma))\sin(\psi)\dot{\psi} + L_I \sin(\gamma)\dot{\gamma} \cos(\psi) \\ &\quad + L_I \sin(\gamma) \cos(\psi)\dot{\psi} - L_I \cos(\gamma)\dot{\gamma} \sin(\psi)\end{aligned}\tag{C.11}$$

Collecting like terms results in:

$$\begin{aligned}\dot{e}_I &= \dot{E}_T + (\sin(\psi) \sin(\gamma) - \cos(\psi) \cos(\gamma))(L_I \dot{\gamma} + L_I \dot{\psi}) - a_I \cos(\psi)\dot{\psi} \\ \dot{n}_I &= \dot{N}_T + (\sin(\psi) \sin(\gamma) + \cos(\psi) \cos(\gamma))(L_I \dot{\gamma} + L_I \dot{\psi}) + a_I \sin(\psi)\dot{\psi}\end{aligned}\tag{C.12}$$

Substituting the following trigonometry identity

$$\begin{aligned}\cos(\psi + \gamma) &= \sin(\psi) \sin(\gamma) - \cos(\psi) \cos(\gamma) \\ \sin(\psi + \gamma) &= \sin(\psi) \sin(\gamma) + \cos(\psi) \cos(\gamma)\end{aligned}\tag{C.13}$$

into Equation (C.12) results in the position dynamics of the implement:

$$\begin{aligned}\dot{e}_I &= \dot{E}_T + (L_I \dot{\gamma} + L_I \dot{\psi})\cos(\psi + \gamma) - a_I \cos(\psi)\dot{\psi} \\ \dot{n}_I &= \dot{N}_T + (L_I \dot{\gamma} + L_I \dot{\psi})\sin(\psi + \gamma) + a_I \sin(\psi)\dot{\psi}\end{aligned}\tag{C.14}$$

## C.4 Inverse Kinematics

The estimation and control algorithms presented in Chapter 7 require the angle between the implement and the tractor. Because no direct measurement of this angle was available, the angle was derived from other available measurements. Creating a sensor that would actually measure the implement angle is not a trivial task. There are many degrees of freedom at the tow pin of an implement which makes measuring the angle between the tractor and implement a cumbersome task. By measuring the position of the implement, not only is it possible to infer the implement angle, but precise locations of the implement can be controlled as well.

The implement angle ( $\gamma$ ) can be calculated from inverse kinematics using simple geometry. The implement position ( $e_I, n_I$ ), the tractor position ( $E_T, N_T$ ), tractor heading ( $\psi$ ), as well as position of the tow pin relative to the implement and tractor positions ( $a_I, L_I, c_I$ ) must all be known as shown in Figure C.2. First the position of the tow pin is calculated by:

$$\begin{aligned} e_1 &= E_T - \alpha \sin(\psi) \\ n_1 &= N_T - \alpha \cos(\psi) \end{aligned} \quad (C.15)$$

Then the offset angle of the GPS receiver is calculated (Note: the offset angle will be zero if the GPS receiver is placed along the center line of the implement).

$$\Delta\gamma = \tan^{-1}(e_I / L_I) \quad (C.16)$$

Next the angle between the GPS receiver and tow pin is calculated.

$$\gamma_1 = \tan^{-1}\left(\frac{e_I - e_1}{n_I - n_1}\right) \quad (C.17)$$

The above angle is in Cartesian space and is the sum of the following angles.

$$\gamma_1 = \psi + 180 \text{ deg} + \gamma + \Delta\gamma \quad (C.18)$$

The implement angle can now be found by rearranging (C.18) above.

$$\gamma = \gamma_1 - (180 \text{ deg} + \psi + \Delta\gamma) \quad (C.19)$$

## Appendix D

### Steering Valve Identification

The steering actuator dynamics are an integral part of the tractor control system. As mentioned in Chapter 3, the steering valve actuator is highly nonlinear. Characteristics of a typical steering actuator, including saturation and a dead-band region, are shown in Figure D.1

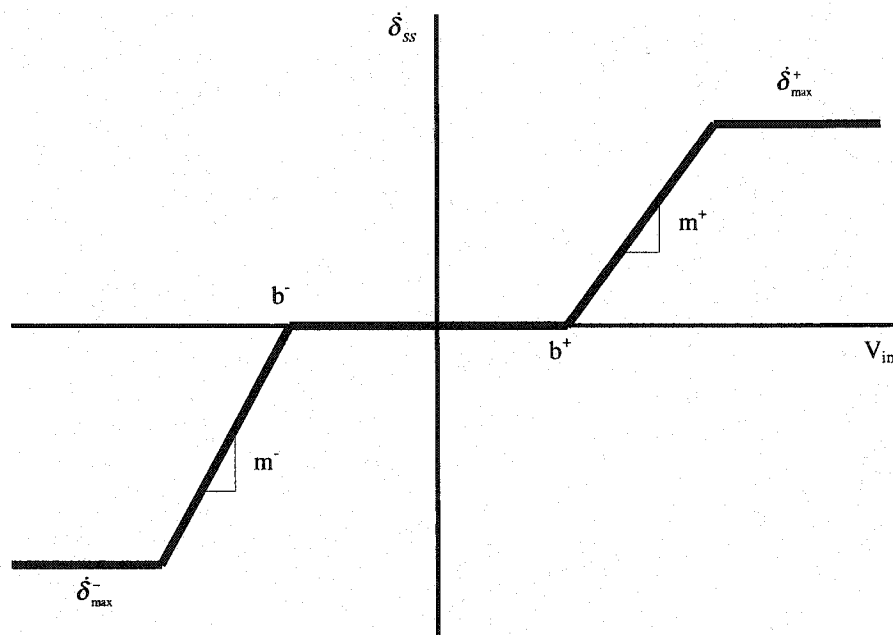


Figure D.1 Typical Valve Characteristics Including Dead-Band Region and Saturation (Steady State Slew Rate vs. Voltage Input).

Data was taken to identify the steady state characteristics of the steering valve. A Pulse Width Modulated (PWM) voltage was used to regulate the 12 volt tractor battery source. The PWM duty cycle percentage creates an effective voltage equal to the percentage of the source voltage. The current drive chips provide the capability to drive the current in a positive or negative direction through the solenoid. Figure D.2 shows the experimental steady state slew rate vs. PWM duty cycle. The figure also contains the characterized (best-fit) valve function,  $F_v(V_{in})$ . The parameters of the valve function characterizing the steering actuator in Figure D.2 are give in Table D.1. Note that there is no such thing as a negative PWM duty cycle. Negative duty cycle in this appendix refers to a PWM duty cycle with the current applied in the negative direction.

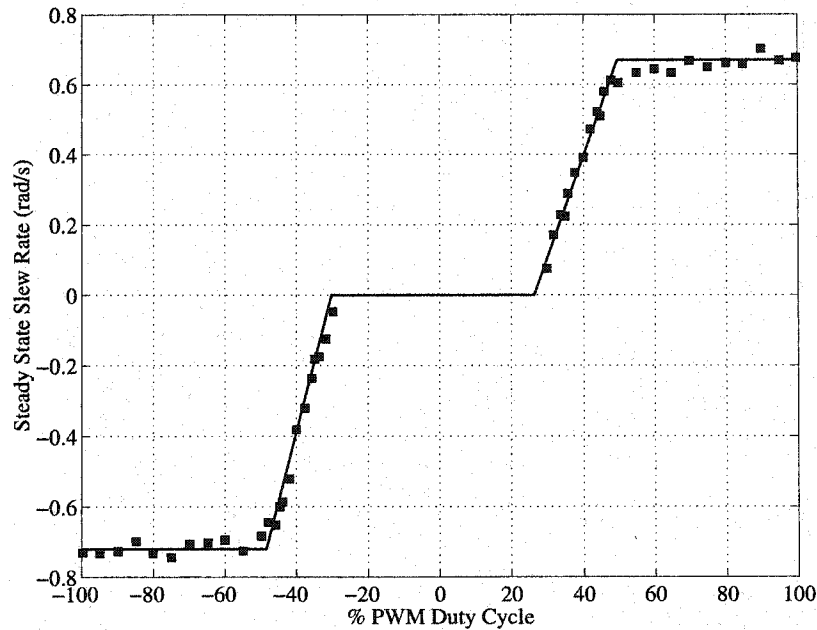


Figure D.2 Experimental and Valve Model of the Steady State Slew Rate vs. Input Voltage.

Table D.1 Parameters Describing the Steady State Characteristics of the Steering Valve.

Parameter	Units	Value
$b^+$	% PWM Duty Cycle	26.27
$b^-$	% PWM Duty Cycle	-30.20
$m^+$	(rad/s) / (% PWM Duty Cycle)	0.0289
$m^-$	(rad/s) / (% PWM Duty Cycle)	0.0395
$\dot{\delta}_{\max}^+$	rad/s	0.67
$\dot{\delta}_{\max}^-$	rad/s	-0.72

Identification of the steady state slew rate versus input voltage is used to invert the non-linear characteristics of the steering valve. Once the steady state characteristics of the steering actuator are known, system identification can be used to determine the remaining dynamics of the steering actuator. Figure D.3 shows a block diagram of the steering valve dynamics as well as the non-linear valve inversion function ( $F_v^{-1}$ ) used to generate the command PWM input ( $u_{command}$ ) from the desired control input ( $u$ ).

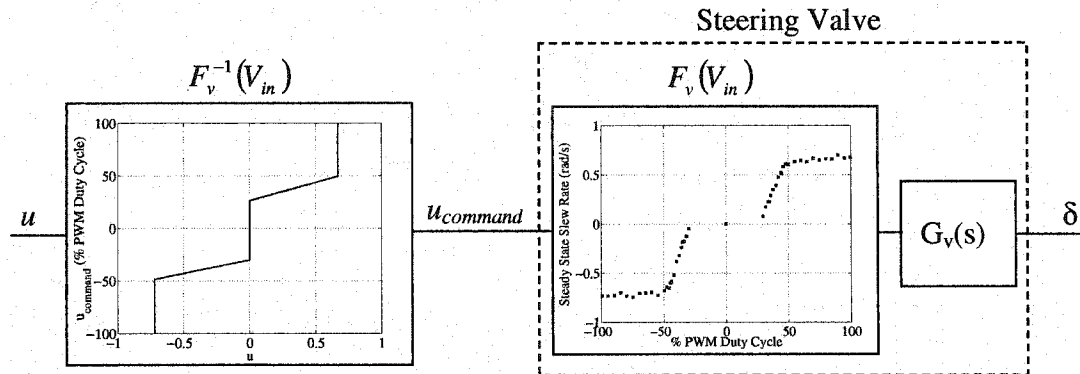


Figure D.3 Valve Inversion and Valve Dynamics Block Diagram.

Assuming that the valve non-linearity is perfectly inverted (i.e., that  $F_v \times F_v^{-1} = 1$ ), the remaining steering valve dynamics from the control input ( $u$ ) to steer angle are then described by the linear transfer function:

$$\delta(s) = \frac{K_v d_v}{I_v s^2 + d_v s} u(s) = \frac{K_v}{s(\tau_v s + 1)} u(s) \quad (D.1)$$

where:  $K_v$ =Valve DC Gain  
 $d_v$ =Valve Damping  
 $I_v$ =Valve Inertia  
 $\tau_v$ =Valve Time Constant

The above transfer function represents a first order lag between input and steering slew rate ( $\dot{\delta}$ ), plus a pure integrator from slew rate to steer angle ( $\delta$ ). The values for the steering valve model in Equation (D.1) were found using a system identification approach similar to the approach taken to model the tractor yaw dynamics in Chapter 2. If the steady state characteristics of the valve have been accurately identified (in  $F_v$ ) then the valve DC gain ( $K_v$ ) will simply be equal to one.

Figure D.4 shows the empirical transfer function (ETFE) from the input ( $u$ ) to output ( $\delta$ ) data. The figure also shows the Box-Jenkins fit of the input-output data. The valve time constant ( $\tau_v$ ) was found to be 0.1053 seconds. Finally, Figure D.5 shows the input as well as the actual and modeled steer angle ( $\delta$ ) and steering slew rate ( $\dot{\delta}$ ) outputs.

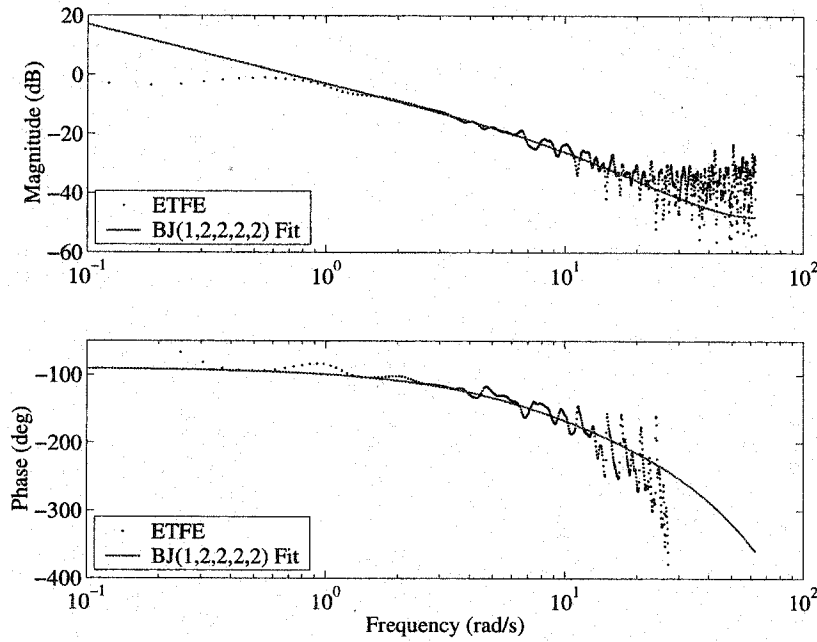


Figure D.4 Empirical Transfer Function and Box-Jenkins Model Fit of the Steering Actuator Dynamics.

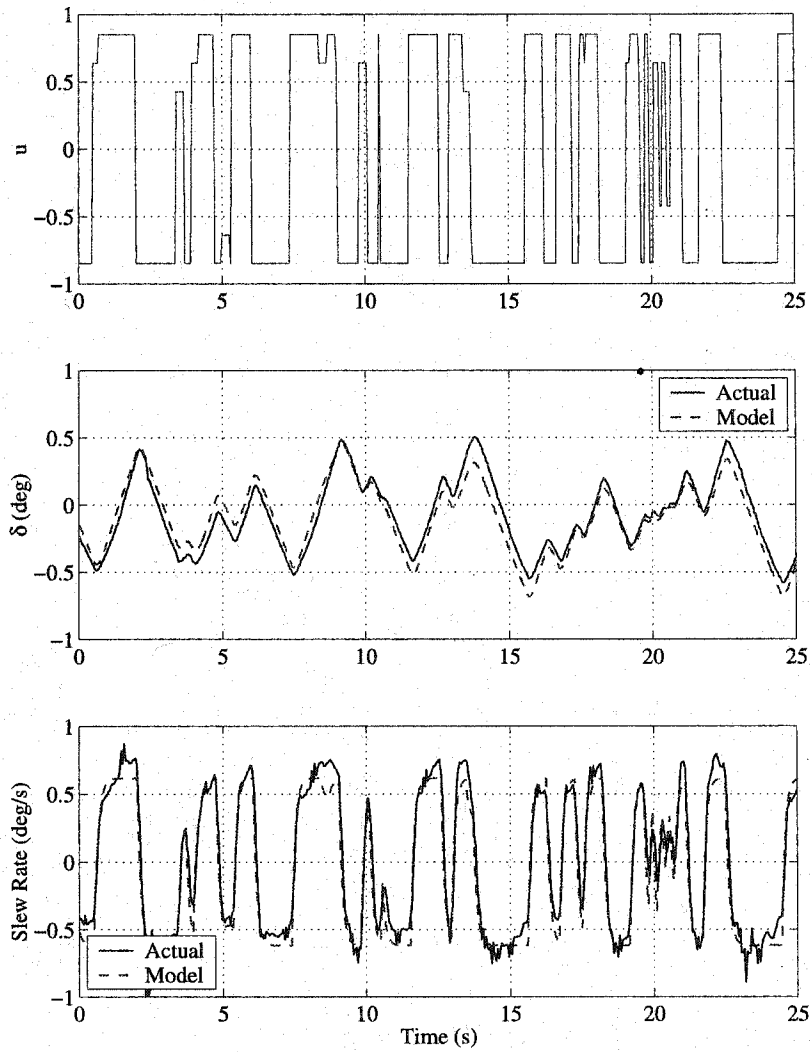


Figure D.5 Valve Input and Actual vs. Model Valve Outputs of Steer Angle ( $\delta$ ) and Slew Rate ( $\dot{\delta}$ ).





# Bibliography

- Abbot, E., Powell, D., "Land-Vehicle Navigation Using GPS," *Proceedings of the IEEE*, January 1999, Vol. 87, No. 1, pp. 145-162.
- Allen, D. E., et. al., "Low-Cost Fiber Optic Gyro for Land Navigation," *Fiber Optic and Laser Sensors XIII*, Vol. 2510, 1994, pp. 28-36.
- Alouani, A.T., et. al., "On the Optimality of Two-Stage State Estimation In the Presence of Random Bias," *IEEE Transaction on Automatic Control*, Vol. 38, No. 8, August 1993, pp. 1279-1282.
- Aono T., Fujii K., Hatsumoto S., Kamiya T., "Positioning of Vehicle on Undulating Ground Using GPS and Dead Reckoning," *Proceedings of the 1998 IEEE International Conference on Robotics & Automation*, May 1998, pp. 3443-3448.
- Bell, T., et al., "Automated Tractor Row and Contour Control on Sloped Terrain Using Carrier-Phase Differential GPS," Fourth International Conference on Precision Agriculture, St. Paul, MN, June 1998.
- Bell, T., *Precision Robotic Control of Agricultural Vehicles on Realistic Farm Trajectories, Ph.D. Dissertation*, Stanford University, December, 1999.
- Berman Z., Powell J. D., "The Role of Dead Reckoning and Inertial Sensors in Future General Aviation Navigation," *Proceedings of the 1998 IEEE Position Location and Navigation Symposium*, April 1998, pp. 510-517.
- Bevly, D.M., Personal Interview with South Texas Farmer David F. Bevly, 1998.

- Bevly, D.M., Rekow, A., Parkinson, B., "Comparison of an INS vs. Carrier Phase DGPS Attitude in the Control of Off-Road Vehicles," *Proceedings of the 1999 ION Annual Meeting*, Cambridge, MA, June 1999(a).
- Bevly, D.M., Rekow, A., Parkinson, B., "Incorporating INS with Carrier-Phase Differential GPS for Automatic Steering Control of a Farm Tractor," Presented at the 1999 SAE Intl. Off-Highway and Powerplant Congress and Exposition, Indianapolis, IN, September 1999(b), Reprinted in *Agricultural Machinery, Tires, Tracks, and Traction (SP-1472)*. Paper No. 1999-01-2851.
- Bevly, D.M., Rekow, A., Parkinson, B., "Evaluation of a Blended Dead-Reckoning and Carrier Phase Differential GPS System for control of an Off-Road Vehicle," *Proceedings of the 1999 ION-GPS Meeting*, Nashville, TN, September 1999(c).
- Bevly, D. M., et. al., "The Use of GPS Based Velocity Measurements for Improved Vehicle State Estimation," *Proceedings of the 2000 American Control Conference*, Chicago, IL, June 2000(a).
- Bevly, D.M., Parkinson, B.W., "Carrier-Phase Differential GPS for Control of a Tractor Towed Implement," *Proceedings of the 2000 ION-GPS Meeting*, Salt Lake City, Utah, September 2000(b).
- Bevly, D. M., Gerdes, J. C., Parkinson, B., "Yaw Dynamic Modeling for Improved High Speed Control of a Farm Tractor," *Proceedings of the 2000 ASME IMECE*, Orlando, FL, November 2000(c).
- Bevly, D. M., Rekow, A., Parkinson, B., "Comparison of an INS vs. Carrier Phase DGPS Attitude in the Control of Off-Road Vehicles," *Journal of Navigation*, Vol. 42, No. 4, Winter 2000 (d).
- Bevly, D. M., Sheridan, R., Gerdes, J. C., "Integrating INS Sensors with GPS Velocity Measurements for Continuous Estimation of Vehicle Side-Slip and Tire Cornering Stiffness," *Proceedings of the 2001 American Control Conference*, June 2001.
- Borenstein J., "Experimental Evaluation of a Fiber Optics Gyroscope for Improving Dead-reckoning Accuracy in Mobile Robots," *Proceedings of the 1998 IEEE International Conference on Robotics & Automation*, May 1998, pp. 3456-3461.

- Bryson, A. E., *Control of Spacecraft and Aircraft*, Princeton University Press, Princeton New Jersey, 1994.
- Brodie, K., "SiRF's Federated Filter Architecture for Automotive Dead Reckoning," *Proceedings of the 1999 ION-GPS Meeting*, September 1999.
- Caglayan, A.K., and Lancraft, R.E., "A Separated Bias Identification and State Estimation Algorithm for Nonlinear Systems," *Automatica*, Vol. 19, No. 5, September 1983, pp. 561-570.
- Chapra, S., Canale, R., *Numerical Methods for Engineers*, 2<sup>nd</sup> Edition, McGraw-Hill, Inc, 1989.
- Chen, B., Wu, C., Uang, H., "A Minimax Tracking Design for Wheeled Vehicles with Trailer Based on Adaptive Fuzzy Elimination Scheme," *IEEE Transactions on Control System Technology*, Vol. 8, No. 3, May 2000, pp. 418-434.
- Chen, C., Tomizuka, M., "Steering and Braking Control of Tractor-Semitrailer Vehicles in Automated Highway Systems," *Proceedings of the 1995 American Control Conference*, Seattle, Washington, June 1995, pp. 658-662.
- Cohen, C.E., et al., "Autolanding a 737 Using GPS Integrity Beacons," *Navigation*, Vol. 42, No. 3, Fall 1995, pp. 467-486.
- Cohen, C.E., Parkinson, B.W., McNally, B.D., "Flight Tests of Attitude Determination Using GPS Compared Against an Inertial Navigation Unit," *Navigation*, Vol. 41, No. 1, Spring 1994, pp. 83-97.
- Cordesses, et. al., "CP-DGPS Based Combine Harvester Control without Orientation Sensor," *Proceedings of the 1999 ION-GPS Meeting*, Nashville, TN, Sept. 1999.
- Crolla, D.A., "The Steering Behavior of Off-Road Vehicles," *Proceedings of the 8<sup>th</sup> IAVSD-Symposium*, Cambridge, MA, August 1983.
- Da R., Dedes G., Shubert, K., "Design and Analysis of a High-Accuracy Airborne GPS/INS System," *Proceedings of the 9<sup>th</sup> International Technical Meeting of the Satellite Division of The Institute of Navigation (ION GPS-96)*, September 1996, pp. 955-964.
- Dixon, J.C., *Tires, Suspension, and Handling*, 2<sup>nd</sup> Ed., SAE Warrendale, PA, 1996.

- Elkaim, G., et. al., "System Identification and Robust Control of Farm Vehicles Using CDGPS," *Proceedings of ION-GPS '97*, September, 1997.
- Franklin, G., Powell, D., Workman, M., *Digital Control of Dynamic Systems*, 3<sup>rd</sup> Ed., Addison-Wesley, Menlo Park, CA, 1998.
- Friedland, B., "Treatment of Bias in Recursive Filtering," *IEEE Transactions on Automatic Control*, Vol. 23, No. 4, August 1978, pp. 735-738.
- Friedland, B., "Treatment of Bias in Recursive Filtering," *IEEE Transactions on Automatic Control*, Vol. 14, No. 4, August 1969, pp. 359-367.
- Gebre-Egziabher D., *Design and Performance Analysis of a Low-Cost Aided Dead-Reckoning Navigator*, Ph.D. Dissertation, Stanford University, December, 2001(a).
- Gebre-Egziabher D., et. al., "A Gyro-Free Quaternion-Based Attitude Determination Suitable for Implementation Using Low Cost Sensors," *Proceedings of the IEEE Position, Location, and Navigation Symposium*, San Diego, CA, March, 2000, pp. 185-192.
- Gebre-Egziabher D., et. al., "A Non-Linear, Two-Step Estimation Algorithm for Calibrating Solid-State Strapdown Magnetometers," *Proceedings of the 8<sup>th</sup> International Conference on Integrated Navigation Systems*, St. Petersburg, Russia, May 2001(b), pp. 290-299.
- Gebre-Egziabher D., Hayward R. C., Powell J.D., "A Low-Cost GPS/Inertial Attitude Heading Reference System (AHRS) for General Aviation Application," *Proceedings of the 1998 IEEE Position Location and Navigation Symposium*, April 1998, pp. 518-525.
- Gillespie, T., *Fundamentals of Vehicle Dynamics*, Society of Automotive Engineers, Inc, Warrendale, PA, 1992.
- Greenwood, D.T., *Principles of Dynamics*, 2<sup>nd</sup> Edition, Prentice-Hall, New Jersey, 1988.
- Haupt, G.T., et. al., "Optimal Recursive Iterative Algorithm for Discrete Nonlinear Least-Squares Estimation," *AIAA Journal of Guidance, Control, and Dynamics*, Vol. 19., No. 3., May-June 1996, pp. 643-649.

- Haessig, D., and Friedland, B., "Separate-Bias Estimation with Reduced-Order Kalman Filters," *IEEE Transactions on Automatic Control*, Vol. 43, No. 7, July 1998, pp. 983-987.
- Hayward, R.C., et al., "Two Antenna GPS Attitude and Integer Ambiguity Resolution for Aircraft Applications," *Proceedings of the ION Technical Meeting*, San Diego, CA, Jan, 1999.
- Heydinger, G., Garrott, W., Chrstos, J., "The Importance of Tire Lag on Simulated Transient Vehicle Response," SAE Paper No. 910235, Presented at *the SAE International Congress and Exposition*, Detroit, MI, 1991.
- Ignagni, M.B., "An Alternate Derivation and Extension of Friedland's Two-Stage Kalman Filter," *IEEE Transactions on Automatic Control*, Vol. 26, No. 3, June 1981, pp. 746-750.
- Ignagni, M.B., "Separate-Bias Kalman Estimator with Bias State Noise," *IEEE Transactions on Automatic Control*, Vol. 35, No. 3, March 1990, pp. 338-341.
- Johnson, G.W., and Modugno, E.J., "Source Localization from Multiple Independent Observables," *IEEE International Conference on Acoustics, Speech, and Signal Processing*, 1989, Vol. 4, pp. 2653-2656.
- Koepele, B., Starkey, J., "Closed-loop Vehicle and Driver Models for High-Speed Trajectory Following," *Transportation Systems - 1990 ASME WAM*, Dallas, TX pp. 59-68.
- Kornfeld, R.P., Hansman, R.J., and Deyst, J.J., "Single Antenna GPS Based Aircraft Attitude Determination," *Proceedings of the ION Technical Meeting*, Long Beach, CA, Jan 1998.
- Lachapelle, G., et al., "GPS Systems Integration and Filed Approaches in Precision Farming, Navigation," Vol. 41, No. 3, Fall 1994, pp. 323-335.
- Larsen, W.E., Nielsen, G.A., Tyler, D.A., "Precision Navigation with GPS," *Computers and Electronics in Agriculture*, Vol. 11, 1995, pp. 85-95.
- Laumond, J.P., Lamiraux, F., "A Practical Approach to Feedback Control for a Mobile Robot with Trailer," *Proceedings of the 1998 IEEE International Conference on Robotics and Automation*, Belgium, May 1998, pp.3291-3296.

- Ljung, L., *System Identification: Theory For the User*, PTR Prentice-Hall, Inc., Englewood Cliffs, NJ, 1987.
- Loeb, J., Guenther, D., and Chen, H., "Lateral Stiffness, Cornering Stiffness, and Relaxation Length of the Pneumatic Tire," SAE Paper No. 900129, Presented at the *SAE International Congress and Exposition*, Detroit, MI, 1990.
- Masson A., Burtin D., Sebe M., "Kinematic DGPS and INS Hybridization for Precise Trajectory Determination," *Proceedings of the 9<sup>th</sup> International Technical Meeting of The Satellite Division of the Institute of Navigation (ION GPS-96)*. September 1996, pp. 965-973.
- Nieminen, T., Mononen, J., Sampo, M., "Unmanned Tractors for Agriculture Applications," *XII CIGR World Congress and AgEng '94 Conference on Agricultural Engineering*, Milano, Italy, September, 1994.
- O'Connor, M.L., Elkaim, G.H., Parkinson, B.W., "Carrier Phase DGPS for Closed-Loop Control of Farm and Construction Vehicles," *Navigation: Journal of the Institute of Navigation*, Vol. 43, No. 2, Summer 1996, pp.167-278.
- O'Connor, M.L., *Carrier-Phase Differential GPS for Automatic Control of Land Vehicles*, Ph.D. Dissertation, Stanford University, December, 1997.
- Owen, G.M., "A Tractor Handling Study," *Vehicle System Dynamics*, Vol. 11, 1982, pp. 215-240.
- Owen, R.H., Bernard, J.E., "Directional Dynamics of a Tractor-Loader-Backhoe," *Vehicle System Dynamics*, Vol. 11, 1982, pp. 251-265.
- Palmer, R. J., Matheson, S.K., "Impact of Navigation on Agriculture," *Proceedings of the American Society of Agricultural Engineers*, St. Joseph, Mich., 1988, paper no. 88-1602.
- Rekow, A., et. al., "System Identification and Adaptive Steering of Tractors Utilizing Differential Global Positioning System," *Journal of Guidance, Control, and Dynamics*, Vol. 22, No. 5, Sept/Oct 1999, pp. 671-674.
- Rekow, A., *System Identification, Adaptive Control, and Formation Driving of Farm Tractors*, Ph.D. Dissertation, Stanford University, March 2001.

- Rodgers, R. M., "Integrated DR/DGPS Using Low Cost Gyro and Speed Sensor," *Proceedings of the 1999 ION National Technical Meeting*, San Diego, CA, January 1999, pp. 353-360.
- Schonberg T., et al., "Positioning an autonomous off-road vehicle by using fused DGPS and inertial navigation," *International Journal of Systems Science*, 1996, Vol. 27, No. 8, pp. 745-752.
- Shreve, E.L., and Hedrick, W.R., "Separating Bias and State Estimates in a Recursive Second-Order Filter," *IEEE Transactions on Automatic Control*, Vol. 19, No. 5, October, 1974, pp. 585-586.
- Smith, L.A., Schafer, R.L., and Young, R.E., "Control Algorithms for Tractor-Implement Guidance," *Transactions of the ASAE*, Vol. 28, No. 2, March-April 1985, pp. 415-419.
- Stengel, R., *Optimal Control and Estimation*, Dover ed, Dover Publications, Meneola, New York, 1994.
- Stombaugh, T.S., Benson, E.R., and Hummel, J.W., "Automatic Guidance of Agricultural Vehicles at High Field Speeds," *Proceedings of the 1998 ASAE Annual International Meeting*, Orlando, FL, July 1998, Paper No. 983110.
- Tacker, E.C., and Lee, C.C., "Linear Filtering in the Presence of Time-Varying Bias," *IEEE Transactions on Automatic Control*, Vol. 17, No. 6, December 1972, pp. 828-829.
- Tanaka, A., "Parallel Computation in Linear Discrete Filtering," *IEEE Transactions on Automatic Control*, Vol. 20, No. 4, August 1975, pp.573-575.
- Weisenburger, S., and Wilson, C., "An Integrated Vehicle Positioning System for Safety Applicatins," *Proceedings of the 1999 ION National Technical Meeting*, San Diego, CA, January 1999, pp. 361-368.
- Zuydam, R., "Centimeter-Precision Guidance of Agriculture Implements in the Open Field by Means of Real Time Kinematic DGPS," *Proceedings of 4<sup>th</sup> International Conference on Precision Agriculture*, St. Paul, MN, July 1998, pp. 1023-1034.